UNIVERSITY OF CALIFORNIA,
IRVINE

Insights into Chemical Processes Garnered Through In Situ Transmission Electron Microscopy

DISSERTATION

submitted in partial satisfaction of the requirements
for the degree of

DOCTOR OF PHILOSOPHY

in Chemistry

by

Peter Tieu

Dissertation Committee:
Professor Xiaoqing Pan, Chair
Professor Matthew Law
Assistant Professor Joe Patterson

2023

DEDICATION

To

my parents Phuoc Tieu and Thanh Huynh

sister Ashley Tieu

friends who have been there to talk to

The most important thing I've learned is that learning isn't passing one's eyes over words.

It is when knowledge is understood for oneself that it attains its true potential.

TABLE OF CONTENTS

LIST OF FIGURES

Page

LIST OF TABLES

Page

ACKNOWLEDGEMENTS

I would like to express my deepest appreciation to my advisor, Professor Xiaoqing Pan, for his continuous guidance, support, and instruction throughout my PhD studies. He has provided the resources and opportunities for me to grow as a researcher. I would also like to thank Professor Matthew Law and Assistant Professor Joe Patterson for serving on my committee and providing feedback on my work.

I would like to thank the numerous colleagues and friends in the Pan research group. In particular, I would like to thank Dr. Wenpei Gao for the mentorship and training on the TEM instrument, analysis, and problem solving thought process. In addition, I would like to thank Dr. Mingjie Xu, Dr. Xingxu Yan, and Dr. Wenjie Zang for their assistance and advice throughout my PhD. I would also like to thank Dr. Chris Addiego, Dr. Huaixun Huyan, Dr. Chaitanya Gadre, Tom Lee, Yifeng Huang, and the other graduate students in the Pan research group with whom I've collaborated during my time at UCI. I would also like to thank the staff members at the Irvine Materials Research Institute, Dr. Toshi Aoki, Dr. Jian-guo Zheng, and Dr. Li Xing for their help and support with my electron microscopy work.

Portion of Chapter 2 of this dissertation is a reprint of the material as it appears in "Directly Probing the Local Coordination, Charge State, and Stability of Single Atom Catalysts by Advanced Electron Microscopy: A Review" [*Small* **2021**, 17, 2006482], used with permission from Wiley. The co-authors listed in this publication are Xingxu Yan, Mingjie Xu, Phillip Christopher, and Xiaoqing Pan. The co-authors provided guidance and feedback.

Portion of Chapter 2 of this dissertation is a reprint of the material as it appears in "XAFCA: a new XAFS beamline for catalysis research" [*J. Synchrotron Radiat*. **2015**, 22, 3], used with permission from the International Union of Crystallography. The authors listed in this publication are Yonghua Du, Yi Zhu, Shibo Xi, Ping Yang, Herbert Moser, Mark Breese, and Armando Borgna.

Portion of Chapter 4 of this dissertation is a reprint of the material as it appears in "How Pt influences H_2 reactions on high surface-are Pt/CeO_2 powder catalyst surfaces" [*JACS Au* **2023**, 3, 8], used with permission from American Chemical Society. The co-authors listed in the publication are Jaeha Lee, Jordan Finzel, Wenjie Zang, Xingxu Yan, George Graham, Xiaoqing Pan, and Phillip Christopher.

Portion of Chapter 5 of this dissertation is a reprint of the material as it appears in "Quasi/non-equilibrium state in nanobubble growth trajectory revealed by *in-situ* transmission electron microscopy" [Nano Today **2023**, 48, 101761], used with permission from Elsevier. The co-authors listed in the publication are Hao Hu, Fenglei Shi, Benwei Fu, Peng Tao, Chengyi Song, Wen Shang, Xiaoqing Pan, Tao Deng, and Jianbo Wu.

Portion of Chapter 5 of this dissertation is a reprint of the material as it appears in “Controllable Growth of Copper on TiO_2 Nanoparticles by Photodeposition Based on Coupled Effects of Solution Viscosity and Photoreduction Rate for Catalysis-Related Applications” [ACS Appl. Nano Mater. **2020**, 3, 5855-5861], used with permission from the American Chemical Society. The co-author listed in the publication is Djawhar Ferrah.

Other portions of this text include unpublished work performed or supervised by collaborators: Dr. Chaitanya Gadre, Dr. Wenpei Gao, Dr. Muqing Li, and Dr. Zhengtao Xu.

I would also like to acknowledge funding provided by the National Science Foundation (NSF) awards under grant No. CBET-2031494 and CHE-1955786. I would also like to acknowledge funding provided by the Department of Energy (DOE), Office of Basic Energy Sciences, Division of Materials Sciences and Engineering, under Grant DE-SC0014430 and DE-NA0004106. I would also like to acknowledge Irvine Materials Research Institute (IMRI) at the University of California, Irvine for their support with transmission electron microscopy experiments, which is supported in part by the NSF through the UC Irvine Materials Research Science and Engineering Center (DMR-2011967).

VITA

Peter Tieu

Education

University of California-Irvine	Irvine, CA
Doctor of Philosophy in Chemistry	2023
California State University, Long Beach	Long Beach, CA
Master of Science in Chemistry	2016
Massachusetts Institute of Technology	Cambridge, MA
Bachelor of Science in Chemistry	2011

Referred Publications in this Thesis

Tieu, P., Yan, X., Xu, M., Christopher, P., Pan, X. "Directly Probing the Local Coordination, Charge State, and Stability of Single Atom Catalysts by Advanced Electron Microscopy: A Review." *Small* (2021)

Lee, J., Tieu, P., Finzel, J., Zang, W., Yan, X., Graham, G., Pan, X., Christopher, P. "How Pt Influences H_2 Reactions on High Surface-Area Pt/CeO_2 Powder Catalyst Surfaces." JACS Au (2023)

Hu, H., Shi, F., Tieu, P., Fu, B., Tao, P., Song, C., Shang, W., Pan, X., Deng, T., Wu, J. "Quasi/non-equilibrium state in nanobubble growth trajectory revealed by in-situ transmission electron microscopy." *Nano Today* (2023)

Djawhar, F. and Tieu, P. "Controllable Growth of Copper on TiO_2 Nanoparticles by Photodeposition Based on Coupled Effects of Solution Viscosity and Photoreduction Rate for Catalysis-Related Applications." *ACS App. Nano Mater*. (2020)

Tieu, P., Gadre, C., Gao, W., Yan, X., Ferrah, D., Li, M., Xu, Z., Pan, X. "In situ observations of thermal post-synthesis modification of a zirconium based MOF using atomic resolution S/TEM and vibrational EELS." *Adv. Funct. Mat.* (Submitted)

Additional Publications

Lyu, Z., Yu, S., Wang, M., Tieu, P., Zhou, J., Shi, Q., Du, D., Feng, Z., Pan, X., Lin, H., Ding, S., Zhang, Q., Lin, Y. "NiFe Nanoparticle Nest Supported on Graphene as Electrocatalyst for Highly Efficient Oxygen Evolution Reaction." *Small* (2023)

Ding, S., Barr, J.A., Lyu, Z., Zhang, F., Wang, M., Tieu, P., Li, X., Engelhard, M.H., Feng, Z., Beckman, S.P., Pan, X., Li, J., Du, D., Lin, Y. "Effect of Phosphorus Modulation in Iron Single-Atom Catalysts for Peroxidase Mimicking." *Adv. Mat.* (2023)

Li, H., Fei, M., Troiano, J., Ma, L., Yan, X., Tieu, P., Yuan, Y., Zhang, Y., Liu, T., Pan, X., Brudvig, G.W., Wang, D. "Selective Methane Oxidation by Heterogenized Iridium Catalysts." *J. Am. Chem. Soc.* (2023)

Ding, S., Barr, J.A., Shi, Q., Zeng, Y., Tieu, P., Lyu, Z., Fang, L., Li, T., Pan, X., Beckman, S.P., Du, D., Lin, H., Li, J., Wu, G., Lin, Y. "Engineering Atomic Single Metal–FeN_4Cl Sites with Enhanced Oxygen-Reduction Activity for High-Performance Proton Exchange Membrane Fuel Cells." *ACS Nano* (2022)

Li, X., Ding, S., Lyu, Z., Tieu, P., Wang, M., Feng, Z., Pan, X., Zhou, Y., Niu, X., Du, D., Zhu, W., Lin, Y. "Single-Atomic Iron Doped Carbon Dots with Both Photoluminescence and Oxidase-Like Activity." *Small* (2022)

Lyu, Z., Ding, S., Tieu, P., Fang, L., Li, X., Li, T., Pan, X., Engelhard, M.H., Ruan, X., Du, D., Li, S., Lin, Y. "Single-Atomic Site Catalyst Enhanced Lateral Flow Immunoassay for Point-of-Care Detection of Herbicide." *Research* (2022)

Murphy, E., Liu, Y., Matanovic, I., Guo, S., Tieu, P., Huang, Y., Ly, A., Das, S., Zenyuk, I., Pan, X., Spoerke, E., Atanassov, P. "Highly Durable and Selective Fe- and Mo-Based Atomically Dispersed Electrocatalysts for Nitrate Reduction to Ammonia via Distinct and Synergized NO_2^- Pathways." *ACS Catal*. (2022)

Huang, Y., Chen, Y., Xu, M., Asset, T., Tieu, P., Gili, A., Kulkarni, D., Andrade, V.D., de Carlo, F., Barnard, H.S., Doran, A., Parkinson, D.Y., Pan, X., Atanassov, P., Zenyuk, I. "Catalysts by pyrolysis: Direct observation of chemical and morphological transformations leading to transition metal-nitrogen-carbon materials." *Mater. Today* (2021)

Wu, S., Li, Z., Li, M-Q., Diao, Y., Lin, F., Liu, T., Zhang, J., Tieu, P., Gao, W., Qi, F., Pan, X., Xu, Z., Zhu, Z., Jen, A.K-Y. "2D metal–organic framework for stable perovskite solar cells with minimized lead leakage." *Nat. Nanotech*. (2020)

Howitz, W.J., Thane, T.A., Frey, T.L., Wang, X.S., Gonzales, J.C., Tretbar, C.A., Seith, D.D., Saluga, S.J., Lam, S., Nguyen, M.M., Tieu, P., Link, R.D., Edwards, K.D. "Online in No Time: Design and Implementation of a Remote Learning First Quarter General Chemistry Laboratory and Second Quarter Organic Chemistry Laboratory." *J. Chem. Educ*. (2020)

Cheng, S., Tieu, P., Gao, W., Hu, J., Feng, W., He, J., Pan, X., Xu, Z. “Crystallinity after decarboxylation of a metal–carboxylate framework: indestructible porosity for catalysis.” *Dalton Trans.* (2020)

Choi, C., Kwon, S., Cheng, T., Xu, M., Tieu, P., Lee, C., Cai, J., Lee, H.M., Pan, X., Duan, X., Goddard III, W.A., Huang, Y. “Highly active and stable stepped Cu surface for enhanced electrochemical CO_2 reduction to C_2H_4.” *Nat. Catal.* (2020)

Ye, F., Xu, M., Dai, S., Tieu, P., Ren, X., Pan, X. “In Situ TEM Studies of Catalysts Using Windowed Gas Cells.” *Catalysts* (2020)

Gao, W., Tieu, P., Addiego, C., Ma, Y., Wu, J., Pan, X. “Probing the dynamics of nanoparticle formation from a precursor at atomic resolution.” *Sci. Adv.* (2019)

ABSTRACT OF THE DISSERTATION

Insights into Chemical Processes Garnered Through In Situ Transmission Electron Microscopy

by

Peter Tieu

Doctor of Philosophy in Chemistry

University of California, Irvine, 2023

Professor Xiaoqing Pan, Chair

Catalysis remains an important field of research that drives economical approaches for various energy conversion applications from natural resources. Industrial catalyzed reactions occur at the surface of heterogeneous catalysts where many different active sites exist. Any atom not at the surface is not directly used to drive chemical reactions. To improve efficiency, catalytic nanomaterials have shrunk to the nano and atomic scale, increasing the surface area/volume ratio. Traditional characterization methods for nanomaterials provide a large scale picture of overall changes but do not exhibit a high degree of spatial information. To that end, transmission electron microscopy (TEM) may be used to probe materials down to the scale of individual atoms through both imaging and spectroscopy. Specialty holders allow for replication of benchtop reactions with which to investigate changes to nanomaterials in situ. Here, in situ TEM was used to gain insights into a variety of chemical processes including bond cleavage and surface reduction of different nanomaterials.

First, we used in situ TEM to observe the contraction of the inter-metal center distances upon heating of a Zr based metal-organic framework before tracking the chemical bond changes with vibrational electron energy loss spectroscopy (EELS). The in situ results were corroborate with ex

situ samples to validate the results. Then, in situ TEM and EELS was used to spatially map the Ce^{3+} aggregation on the surface of Pt loaded ceria nanoparticles. The localization of the Ce^{3+} had remained an unanswered question prior. The surface reduction was seen to proceed in an irreversible fashion which was attributed to orientated attachment, a precursor step to sintering. Finally, in situ TEM was performed in a liquid environment analyzing the growth of nanobubbles and the dissolution of octahedral core-shell nanoparticles. Both nanomaterials exhibited stages of structural changes that correspond to size stability and atom migration, respectively. As seen with the variety of nanomaterials observed, in situ TEM gives insight to the various chemical processes that occur when replicating benchtop reactions.

Chapter 1

Introduction

1.1 Heterogeneous Catalytic Nanomaterials

Catalysis is an important field of research because it provides economical approaches to drive various energy conversion processes to produce value-added chemicals and fuels from natural resources such as oil, coal, solar energy, wind, and natural gas. The largest scale (by mass and value) catalyzed reactions occur at the surface of heterogeneous catalysts where there are many active sites. Any atom not at the catalyst surface is not directly used to drive chemical reactions but may aid in the stability and/or modulation of the surface sites. To increase the conversion yield per gram of catalyst, the use of smaller and smaller materials approaching the nanoscale with high surface/volume ratios have been developed. Further advances from nanoparticle sized catalysts to stabilized single atom catalysts (SACs) have also been achieved, pushing the field of catalysis further. These nanoparticles and SACs can exhibit characteristics distinct from bulk materials of the same composition and from each other as well. Due to the size reduction from bulk to nanoparticles and smaller, a larger fraction of surface atoms is left with dangling bonds. The reduction in size modifies the exhibited behavior through mechanisms such as quantum size effect, strong metal-support interactions, surface effects, and strain.[1–10] As a result of these influences, the behavior of nanomaterials must be examined at the nanoscale.

Characterization of catalytic nanomaterials, both in situ and ex situ, to understand the formation, intermediate stages, stability, and reactivity is important toward designing better catalysts. The catalysts surface may shift about during a reaction or the active site may become inactive.

Structural instability may lead to temporary higher turnover numbers but also to long term degradation. A recent work showed the release of Au single atoms from a nanoporous Au surface during methane pyrolysis, showing how an irreversible process may occur under reaction conditions. [11] The nature of these structural changes during synthesis, pre-treatment, and catalytic activity vary based on the reaction conditions and the starting material. Multiple characterization techniques to probe the nanomaterials directly and indirectly are commonly used. Bulk spectroscopic techniques performed on the benchtop are the most readily available. Further complex X-ray based spectroscopic techniques are performed at large instrumentation facilities. Further detailed visualization and interrogation at the nanoscale is achieved through electron microscopy, both ex situ and in situ.

1.2 Transmission Electron Microscopy

1.2.1 Sample Preparation

The acquisition of high quality data during a TEM experiment begins with the preparation of a high quality sample. For the purpose of transmission electron microscopy, a sample should be less than 100 nm in thickness, with more ideal cases being less than 50 nm, especially when dealing with heavier elements starting with the 4d transition metals. While the synthesis of nanomaterials and catalysts generally result in individual particles on the nanometer scale of appropriate size, the individual particles are synthesized at the micro or milligram scale, typically resulting in a final powder form.

The typical method of achieving a dispersion of the nanomaterial from powder form is via dropcasting. By suspending the powder in a solvent followed by sonication, the powder can be separated into small clusters and/or individual particles for imaging and analysis. The solvent choice and sonication duration will have an impact on the final dispersion. The solubility of the nanomaterial in the solvent is the most prudent factor, with water being the common aqueous solvent and a light alcohol such as ethanol or methanol being the option for a mildly polar solvent. For non-polar solvents, toluene or hexane may be used but this solvent choice is less common. To aid with the dispersion, sonication is subsequently utilized. Fifteen minutes or less is a common choice for duration. A longer duration may be selected but may damage more fragile nanomaterials. Once sonication is complete, a micropipette is used to transfer a droplet of the solution to a TEM grid without direct contact. Various TEM grids exist for different applications. The most common are a copper ring with a copper mesh. Other metals such as gold or nickel are also available when copper is a part of the nanomaterial to be examined and spectroscopy is necessary. Onto the copper mesh, an amorphous support may be deposited. The support may be continuous or have regular holes or irregular holes or other shaped voids. Often, the support is carbon but other light materials that can be made into an amorphous film (e.g. silicon nitride, silica) are3omercially available. Many kinds of specialty grids for applications such as focused ion beam (FIB) are commercially available. The solvent is allowed to evaporate and the sample preparation is complete.

On occasion, some nanomaterials may not be of sufficiently small size and cannot be properly dispersed by the solvent choice alone. This can be seen with materials that have been pyrolyzed (or nearly), exhibiting a hardened structure. To achieve a thickness that is electron transparent,

mechanical grinding with a mortar and pestle (or ball milling if there is sufficient quantity) can be used. However, this leaves particles of various sizes. A size selection of the grinded particles is required. By dispersing the grinded particles in the desired solvent to be used for dropcasting and using centrifugation, the larger particles are forced into the pellet at the centrifuge tube tip while smaller particles remain suspended in the supernatant. By using increasing centrifugal force and retaining the supernatant, smaller and smaller particles may be selected for TEM analysis.

1.2.2 Conventional Transmission Electron Microscopy

A typical electron microscope is composed of an electron gun, condenser system, objective lens, movable specimen stage, intermediate and projector lenses, image-recording system (CCD camera and various detectors), and many optional equipment including aberration corrector, EDS detector, and electron energy-loss spectrometer. In conventional TEM mode, electrons emitted from the electron gun form a parallel beam after passing through the condenser lens and illuminate the sample (Figure 1.1). Then, electrons can be diffracted by the interaction with the sample and carry this information onward. The electrons are focused by the objective lens. The intermediate lens and projector system can be configured to project either this diffraction pattern or allow the diffracted beams to interfere further to form a real space image for projection. The objective lens and projector lens also control the magnification through a wide range. Finally, the real space image or diffraction pattern formed by the electron beam is recorded by an image-recording device such as a digital camera.

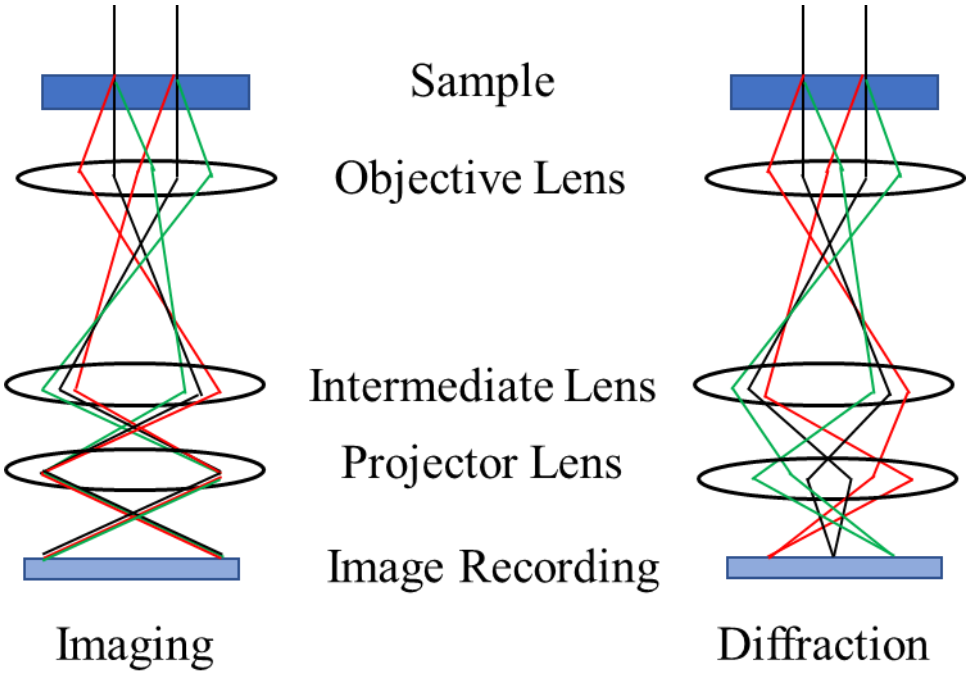

Figure 1.1. Ray diagrams
Schematic of a conventional TEM in imaging and diffraction mode.

In high resolution TEM (HRTEM), a high spatial resolution (~0.05 nm) image can be acquired with aberration-corrected microscopes by using a large objective aperture that includes both the transmitted and diffracted beams. For very thin samples (less than 5 nm), the phase-object approximation may be applied to understand the phase-contrast of the image. However, under most circumstances, the phase-object approximation cannot be used. The phase change due to interaction of the electron beam and the sample cannot be considered linearly proportional to the electrostatic potential of the sample. The contrast in the recorded image depends on multiple factors including the exit wave function of electrons passing through the sample, sample thickness, misalignment to a zone axis, defocus, and various aberrations of the optical lenses and thus the contrast of the final image should not be interpreted as representative of atomic structures.

Computer simulation is used in conjunction with HRTEM to come to a final conclusion of the atomic structure.

1.2.3 Scanning Transmission Electron Microscopy

In scanning transmission electron microscopy (STEM), the electron beam is converged to form a small probe (Figure 1.2a). With the invention of aberration correctors, modern electron microscopes achieve an electron probe with a sub-Ångstrom size to acquire atomic resolution images. Scanning coils raster-scan the probe across a region of the sample with magnification controlling the step size. The electrons can be elastically and inelastically scattered by the atoms in the sample. The scattered electrons are picked up by electron detectors and integrated together to form an image. The electrons that are scattered to a high angle are collected by a ring-shaped high angle annular dark field (HAADF) detector to form a HAADF image (Figure 1.2b). Unlike the above-mentioned HRTEM images, HAADF images are formed by incoherent scattered electrons.[12–14] The scattering probability is approximately proportional to $Z^{1.7\text{-}2}$, where Z is the atomic number and the exponent changes based on the collection angle.[15] Thus, HAADF images are also called Z-contrast images. Z-contrast images are less sensitive to sample thickness and alignment to a zone axis, allowing for direct interpretation of the atomic structure from the intensity of the HAADF image. On the other hand, an annular bright-field (ABF) detector with the ring-shaped inner circumference of the transmitted electron disk collects low-angle scattered electrons. Thus, ABF images can be effective to visualize the atomic column of light elements such as H, Li, and O.[13,15,16] If the electrons in the transmitted central disk is collected by a circular retractable bright-field (BF) detector, a bright-field (BF) image is generated (Figure 1.2c). BF STEM images

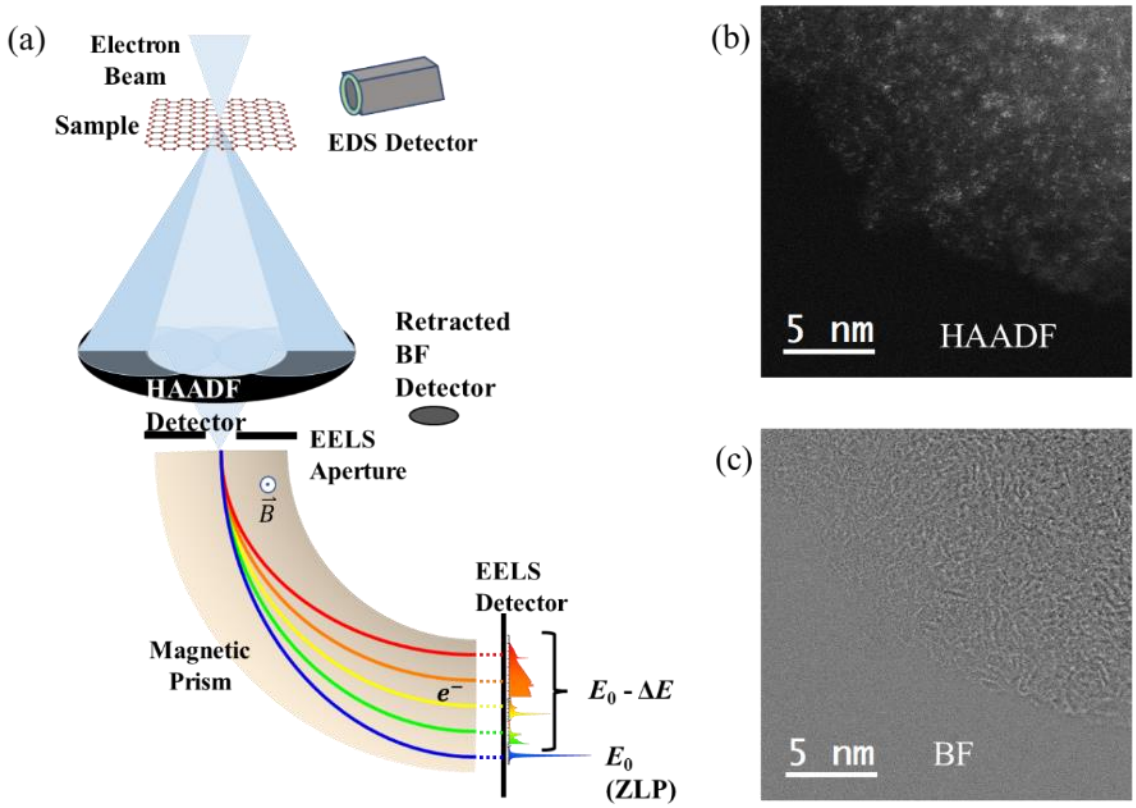

Figure 1.2. STEM configuration
(a) STEM configuration schematic depicting HAADF, BF, EDS, and EELS detectors. Identical region of Fe and Mo single atoms dispersed on N-doped graphene as imaged by the (b) HAADF and (c) BF detectors on GrandARM. The Fe and Mo show up readily in the HAADF image with light elements showing a faint intensity. The BF image shows the clear presence of the lighter elements but is harder to distinguish atomic locations.

primarily contain the coherently scattered electrons, and thus do not exhibit Z-contrast characteristic and are more analogous to HRTEM images which also contain coherently scattered electrons. In STEM, HAADF and ABF/BF images may be acquired simultaneously when solely imaging.

For the work mentioned here on the GrandARM microscope at UCI, the following table is considered the standard STEM imaging condition unless otherwise mentioned.

Table 1.1 Standard STEM imaging conditions on GrandARM

Instrument Component	Specification
Acceleration voltage	300 kV
Condenser lens aperture	30 µm
STEM probe size	0.06 nm
Convergence semi-angle	32 mrad
EELS energy resolution	0.34 eV
EDS energy resolution	121.5 eV
HAADF detector	Inner angle: 53 mrad Outer angle: 180 mrad
BF detector	Outer angle: 31 mrad
Spot size	7C
Camera length	12 cm

1.3 In situ Transmission Electron Microscopy

In situ TEM imaging under reaction conditions allow for observations to garner an understanding of key points during the synthesis, activation, and degradation of the nanomaterials, particularly for catalysts, which may be missed ex situ.[17] For synthesis, in situ imaging gives information about the mechanism through which the nanomaterial forms as well as at what point undesirable changes occur. The temporal resolution of equipment used within electron microscopes has been improving, enabling the capture of fast processes due to the availability of direct electron detector for TEM mode and faster scanning for STEM mode. Gatan, Inc. has improved their cameras through the years, going from 25 to 6000 frames per second depending on the type of camera and the detector binning. The temporal resolution afforded by hardware improvements have aided analysis of faster processes. In situ TEM experiments can be carried out either within environmental TEM (ETEM) or using specialty holders. The work discussed here use micro-electromechanical systems (MEMS) based E-chips with specialty holders to provide

stimulus such as heat, gas, liquid, light, or strain (or a combination) at the microscale. A general schematic for a heating E-chip and a gas cell E-chip can be seen in Figure 1.3. For these holders, the miniaturization of devices must be accomplished. Because the reaction environment can be kept separate from the microscope's vacuum environment, large adjustments to the microscope operating conditions are not needed. To acquire images and spectroscopy, the microscope is set up in the same conditions as those for ex situ experiments and then the holder is inserted to commence the experiment. The environment of the E-chip is controlled separately from the microscope software control as well. In situ TEM using MEMS based holders allow for the replication of benchtop reactions in the microscope to acquire information about the reaction process with little to no change from standard microscope operation.

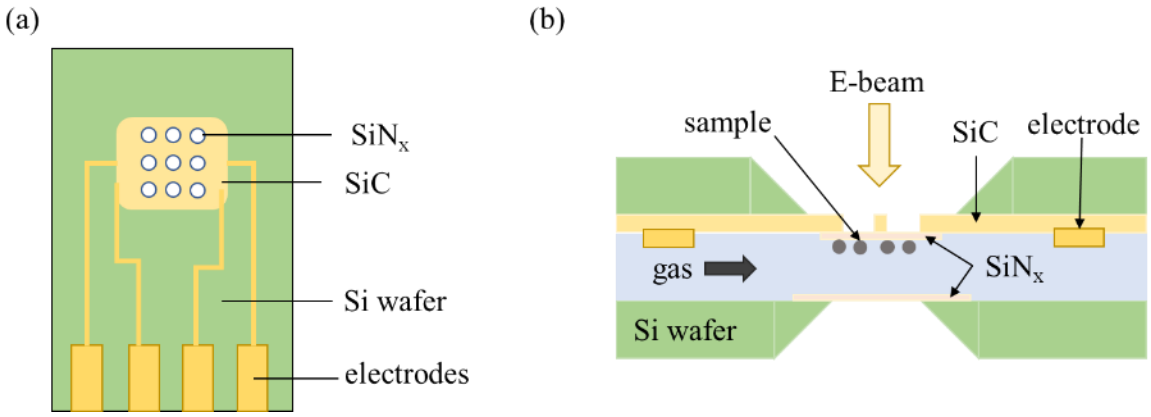

Figure 1.3 E-chip schematics
(a) Schematic of a Protochips Fusion heating E-chip viewed from the top. The electron transparent SiN_x membrane covers the central region of the SiC heating unit. (b) Schematic of a Protochips Atmosphere gas cell E-chip viewed from the side. The slanted cut of the Si wafer allows for higher signal detection of X-rays with the EDS detector.

Chapter 2

Comparison of TEM and Macroscopic Spectroscopy Techniques

2.1 Energy Dispersive X-ray Spectroscopy

Energy dispersive x-ray spectroscopy (EDS) is a spectroscopic technique used in electron microscopes for elemental identification, especially at low magnification to provide conclusive evidence of the elemental distribution and/or homogeneity of a material. The ease of performing EDS also allows the operator to quickly acquire the spectrum data to complement the HAADF images without changing many microscope parameters. The wide energy detection window allows for broad scanning of multiple elements, especially heavier elements (>4p elements). To generate an EDS spectrum, the incident electron beam can eject an electron from the inner shell of an atom in the sample, forming an electron hole. Another electron from an outer shell then fills this hole and the resultant energy difference may be released in the form of an X-ray, as shown in Figure 2.1. Different elements have distinct characteristic X-ray energies, which, when combined with the raster-scanning nature of STEM mode in the electron microscope, allow for spatially resolved elemental mapping which may not be readily determined from HAADF imaging alone (Figure 2.2). In combination with low and high magnification HAADF images, EDS provides a clear assessment of the distribution of elements across nanomaterials. For well-defined structures with atomic columns aligned to a low order zone axis such as perovskite thin films, atomic resolution EDS elemental maps may also be achieved.

However, the energy resolution for EDS (121.5 eV for GrandARM) may not allow for the

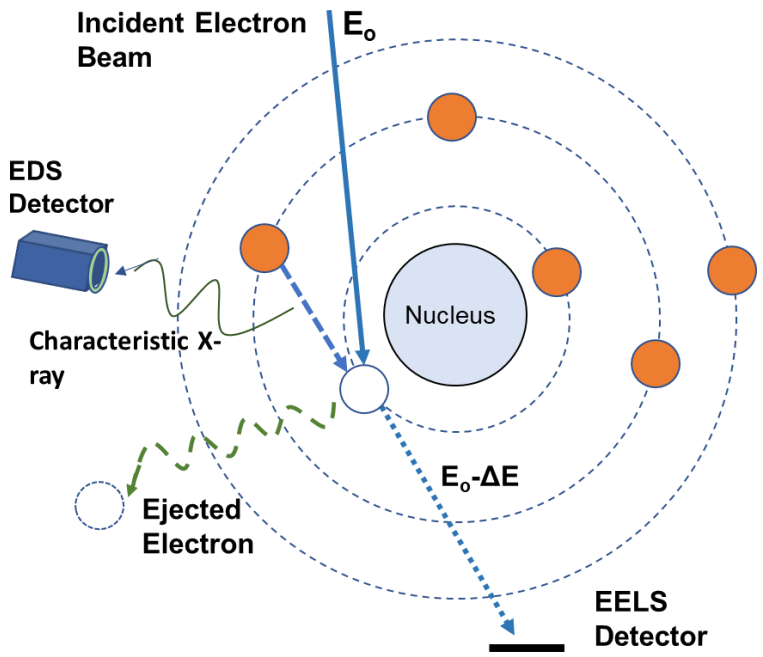

Figure 2.1. EDS and EELS sample interaction
Schematic of the interaction of the electron beam with an atom to generate EDS and EELS signals.

distinction of overlapping characteristic peaks, e.g. the Mo Lα (2.29 keV) and S Kα (2.31 keV) peaks of MoS_2. In addition, quantitative EDS measurements are only a rough estimate without the use of standards to calibrate the signal within a specific microscope. The amount of generated X-rays is also impacted by the extent of electron channeling through a material which is impacted by the tilt relative to a zone axis.[18] There have been some works which spatially mapped single atoms through EDS with careful quantitative evaluation of the EDS counts to confirm the signal came from a single atom and not from a cluster of atoms.[19–21] At the same time, the authors recognize the lower collection efficiency of EDS compared to electron energy loss spectroscopy (EELS) which provides such a challenge for high quality quantitative EDS. As mentioned earlier, the wide energy scan range allows EDS to be a powerful tool for the detection of heavier elements. This is of particular relevance to single atoms of heavy elements which have characteristic peaks

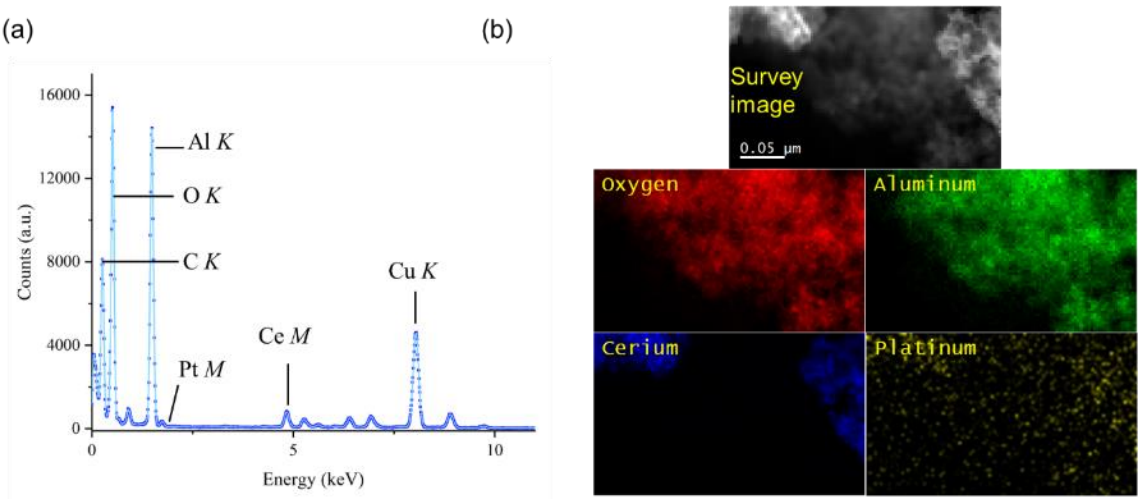

Figure 2.2. Example EDS data
(a) EDS spectrum of 2% Pt/CeO_2:γ-Al_2O_3 at a 1:4 mass ratio on a TEM grid. Carbon and copper signals arise from the TEM grid. (b) Survey image region from the EDS scan and the elemental maps.

at very high loss that is not as readily picked up with an EELS detector. Additionally, some elements are more prone to background contributions such as Fe which can be found in EDS detectors or Ti which standard TEM holders utilize in the construction. Hence, other spectroscopic techniques in conjunction with EDS should be considered.

2.2 Electron Energy Loss Spectroscopy

HAADF images are mainly formed by integrating incoherent elastically scattered electrons which only change the propagating direction without losing energy.[12] At the same time, some electrons can be inelastically scattered due to various interactions with the sample including: inner-shell ionizations (Fig. 2.1), inter- and intra-band transitions, and plasmon, exciton, and phonon excitations. Consequently, the transmitted electrons lose energy equivalent to the energy of the corresponding interaction, which provides local coordination and chemical information as well as

the electronic and vibrational structure of the materials. The energy loss of these inelastically scattered electrons can be measured using a magnetic-prism spectrometer. After the projector lenses and HAADF detector, the electron beam passes through an EELS aperture into the spectrometer. In the magnetic prism, the electrons are deflected to different trajectories according to their energy. The outgoing electrons, with different energy loss, are refocused onto an EELS detector to form an electron energy-loss spectrum. An EEL spectrum can be divided into regimes with different energy spans. In the low-loss regime (0–50 eV), the spectrum contains the zero-loss peak (ZLP), plasmon peaks, and signals, such as phonons, reflecting the electronic and vibrational structure of the material. The ZLP, composed of elastically scattered electrons, is a sharp peak centered at 0 eV with the full width at half maximum of the ZLP defining the energy resolution of EELS. A high energy resolution is critical to visualize the fine structure of ionization edges. The typical energy resolution is about 0.3–0.6 eV for a field emission gun (0.34 eV for GrandARM at 300 kV) and has been improved to sub-8 meV with the help of a monochromator.[22,23] The plasmon peak is commonly utilized to estimate the sample thickness, information which can be

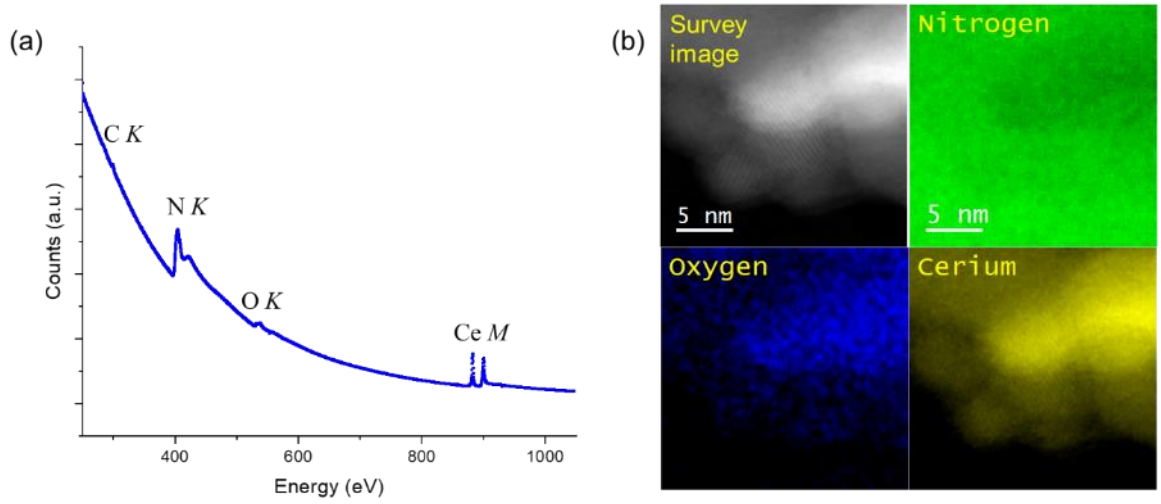

Figure 2.3 Example EELS data
(a) Coreloss EELS spectrum of CeO_2 nanoparticles on a SiN_x membrane using 0.50 eV/ch dispersion. Si *K* and *L* edges are not in this energy window. (b) Survey image region from the EELS scan and the elemental maps.

used for simulating and interpreting various imaging conditions such as HRTEM. In the core-loss EELS regime (>50 eV), there are characteristic peaks for different elements (similar to EDS) which allow for elemental mapping (Figure 2.3). The improved energy resolution allows for distinction of fine structure and visualization of the lower energy regime near the zero-loss peak. By combining a small probe size with adjustable energy resolution, EELS elemental mapping may be performed with more details related to the electronic structure, in comparison to EDS elemental mapping. While HAADF-STEM imaging is excellent for visualizing nanomaterials, there are limitations to the interpretation through Z contrast. For instant, the lighter elements on an organic support, such as C, N and O, are not easily detected, and intensity profiles may not distinguish between elements of similar atomic weight. As such, EELS mapping is commonly used to identify elements in conjunction with HAADF images. Because of the better energy resolution compared to EDS, EELS provides more detailed information in the fine structure of the ionization edges.[24,25] By analyzing these features, the local coordination and oxidation state of nanomaterials down to the single atom can be ascertained.

Both spectroscopic TEM techniques are used as complementary tools with the spatial resolution limited by the size of the probe formed from the electron beam. Acquisition of both EDS and EELS data must be balanced between sufficient signal-to-noise ratio and minimizing beam-induced damage as noted by Egerton and Watanabe.[26] The combination of STEM and EELS is capable of probing atomic resolution compositional and chemical information, making this combination a powerful technique in the study of nanomaterials.[27]

2.3 Vibrational Electron Energy Loss Spectroscopy

As the invention and improvement of the monochromator and new-type spectrometers pushed the energy resolution to the meV range, the field of vibrational EELS was pioneered in 2014 and has been expanding since.[28] Besides the inelastic scattering due to the excitations of inner-shell and outer-shell electrons of atoms, the electron can also interact with the nucleus and experience the lattice vibration of the material, and subsequently lose energy equivalent to the eigenenergy of excited vibration modes. The correlation of vibrational modes seen in the EEL spectrum usually have direct analogues to the peaks measured by FTIR and Raman spectroscopy which allow for probing of bond changes during a chemical reaction.[29] Even the difference between ^{12}C and ^{13}C can be spatially resolved with vibrational EELS.[30] The applications of vibrational EELS are constantly being explored.[31–35] While probing the vibrational modes of heavy metals may not be possible at the moment due to the limited energy resolution and poor signal-to-noise ratio of the EELS detector, the influence of the metal catalysts on the local support environment or on a reactant during a chemical reaction can be investigated. Changes to vibrational modes are likely to accompany adsorption/desorption of a reactant which can be tracked through vibrational EELS with high spatial resolution. The strength of vibrational EELS lies in probing light elements' interaction spatially.

2.4 Probe Molecule FTIR

Probe molecule FTIR is a common technique employed with metal nanoparticles and single atom catalysts to characterize active surface site structures due to the inactivity of metal-metal and metal oxide bonds to IR.[6,36–38] CO is commonly used as the probe molecule due to the strong binding of CO to many metal centers and the site-specific vibrational fingerprint typically observed from

1800–2200 cm^{-1} as a function of the metal oxidation state and local coordination. The strength of the CO backbonding, and thus the stretching frequency, is directly influenced by the electron density of the bound metal and the orientation of the CO relative to the metal. The different binding mechanisms (e.g. linear, bridged, geminal) of CO induce changes in the vibrational frequency, providing structural information about the adsorption site. CO bound to metals have a large IR extinction coefficient, making the signal-to-noise ratio of even a small amount of bound CO adaquate.[39] Further development of FTIR as a rapid analytical screening tool was accomplished by combining HAADF-STEM imaging with CO FTIR to provide complementary information about single atom catalyst synthesis and structure.[40] The FTIR measurements provide a sample averaged probe of the synthesized metal catalyst while the HAADF images give atomic visualization of the corresponding structures. By imaging at different metal loadings, the nanoparticle to single atom ratio can be confirmed, setting up a calibration curve of sorts to rapidly screen future synthesis using the same metal, thereby increasing the rate of screening of synthesis methods.

Along with ex situ samples, FTIR can be useful for examining in situ structural changes of catalysts, inferred from changes in the nature of bound species. For example, Rh/TiO_2 catalysts exposed to elevated temperatures and high CO_2 to H_2 feed ratios showed dynamic product selectivity in the CO_2 reduction reaction. In situ FTIR was used to study the strong metal support interaction (SMSI) between the Rh and TiO_2 support by Matsubu et al.[41] A redshift of the CO stretch on Rh by 50 cm^{-1} as well as a weakening of the intensity of the stretch was observed during reactive treatments. To identify the cause of the redshift, TEM imaging was employed. A buildup of carbonate and formate like species (HCO_x) was observed to cover the support. The buildup of the HCO_x species on the TiO_2 induced oxygen vacancies in the TiO_2 substrate. The oxide vacancy

caused the metal oxide to become more mobile, migrating onto the Rh nanoparticles and reducing the concentration of CO bound to the surface. The presence of SMSI was hinted at via FTIR but needed confirmation by in situ microscopy techniques that look directly at the nanomaterial.

2.5 Raman Spectroscopy

Raman spectroscopy is a non-destructive spectroscopic technique that provides information about chemical structure and bonding. Using a monochromatic laser light, a sample is illuminated and some light is scattered with a change in the energy due to interactions with the molecular vibrations. This Raman scattering is specific to the composition and structure of the bond and molecule, allowing Raman spectroscopy to be used as a chemical fingerprint technique. In a spectrometer, monochromatic light, typically in the visible or near IR range range, excites the sample to a virtual energy state (Figure 2.4). The sample relaxes back to a different vibrational state, releasing a photon with different energy than the incident light. A loss of energy is called a Stokes shift while a gain of energy is termed anti-Stokes. Samples for Raman spectroscopy do not require special preparation and can even be performed through transparent or opaque containers.

Raman spectroscopy can be considered as a complimentary spectroscopic technique to IR. Whereas IR requires a change in the dipole moment in a vibration, Raman spectroscopy requires a change in the polarization (i.e. the shape of the electron cloud). Materials and bonds that are IR active have weak Raman signals and vice versa. Polar chemical bonds where electrons are tightly held toward one atom do not exhibit high polarization and have weak Raman signals. On the other hand, homonuclear bonds exhibit a high degree of polarizability. Similarly, metal-ligand bonds have a high tendency to be Raman active due to the large amount of mobile electrons from the

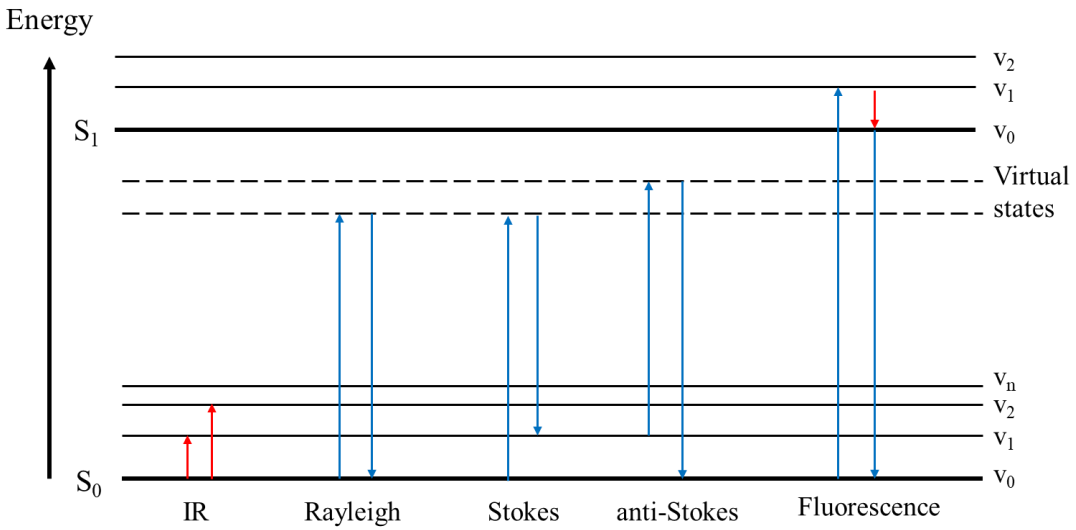

Figure 2.4. Jablonski diagram of FTIR and Raman transitions
Jablonski diagram depicting the energy transitions for IR absorption. In Raman spectroscopy, after excitation to a virtual state, the majority of the scattering is elastic (Rayleigh) with some inelastic scattering (Stokes and anti-Stokes). Due to the high energy wavelength used for excitation in Raman, fluorescence is another possible result.

metal. Therefore, Raman is used to probe materials that do not show up in IR spectra or to avoid strong IR peaks. For example, O-H bonds have weak signals in the 200-2000 cm^{-1} range in Raman, allowing for investigation of samples dispersed in water. The energy resolution in most commercial spectrometers is 2-4 cm^{-1} which is sufficient to resolve small changes to the chemical bond and structure, such as differentiating between ortho-, meta-, and para- positions.[42]

Similar to IR, Raman has limitations when applied to nanomaterials. The Raman active chemical bonds which are present in organic materials may not be present in ionic salts or purely metallic compounds. In addition, highly fluorescent materials may wash out the already relatively weak Raman signal. While there are ways to mitigate the impact of fluorescence with a longer excitation wavelength (1064 nm) and/or spatially offset Raman spectroscopy, these options may not always be available. Finally, as a bulk spectroscopic technique, the spectra are averages of the ensemble. The differentiation of behavior at heterogeneous sites via Raman should be coupled with other

methods to provide structural evidence.

2.6 X-ray Absorption Spectroscopy

X-ray absorption spectroscopy (XAS) utilizes X-rays to probe the electronic state and coordination of a material. The highly penetrating nature of X-rays allow the sample to be crystalline, amorphous, in liquid, gaseous, etc. The high energy of X-rays enable the analysis of energy regions which are not as accessible with other techniques, of particular relevance to heavy metal and metal-metal energetics. Additionally, development of operando spectroscopy have enabled investigations into the evolution of materials under catalytic conditions.[43] X-ray absorption spectroscopy measures the absorption coefficient of a material as a function of energy, with a sharp rise at the energy corresponding to the binding energy of a core electron. For transmission XAS, the absorption coefficient may be expressed as $\mu(E) = \ln(I_o/I)$ where I_o is the intensity of the X-ray before the sample and I is the measured intensity after the sample. The resulting spectrum has distinct regions corresponding to X-ray absorption near edge structure (XANES) and extended X-ray absorption fine structure (EXAFS) which show features to determine the electronic and geometric structure (Figure 2.5a). The XANES region arises from excitation of core electrons to the conduction and valence bands and is used to determine the electronic state. The EXAFS region arises from scattering interactions of photoelectrons with neighboring atoms and thusly is used to determine the local geometry and coordination environment.

XANES analysis looks at the sharp absorption peaks that are dramatically changed by the localized electronic state. The position of the edge and the shift can be used to determine the valence state, similarly to coreloss EELS. A linear combination of known spectra can be used to acquire

compositional ratios of mixed valence materials. In contrast to XANES, the analysis of EXAFS data is not as straightforward but can be fully interpreted. After pre- and post-edge background subtraction, the spectrum is converted from energy space to k space. A weighting is applied (typically k^2 or k^3) to counteract the rapid decay of the spectrum in k space. A Fourier transform is applied to bring the spectrum from k space to R space. This transformation is usually shown as the absolute value, $|\chi(R)|$, with peaks that correspond to coordination shells. Each coordination shell is modeled individually and then compared to the raw data to ensure a good fit. This fitting generates the average coordination around the atom. Together, XANES and EXAFS give the electronic and geometric information about each type of atom in a sample.

While EXAFS modeling has improved in both quality and accessibility, there remain limitations due to the process which is used for the analysis.[44] The key assumptions lie during the modeling process which assumes a uniform structure (or an average structure) around each atom type. This is due to the fact that the data is a summation from a micrometer sized sample so with no spatial information. Therefore, simple periodic structures fit well but polydispersity is not effectively modeled. Additionally, highly disordered compositions exhibit suppression of the second-shell peak.[45,46] As such, XAS data is useful for understanding well-defined materials but additional methods such as EELS to provide site-specific information should be considered in conjunction with XAS.

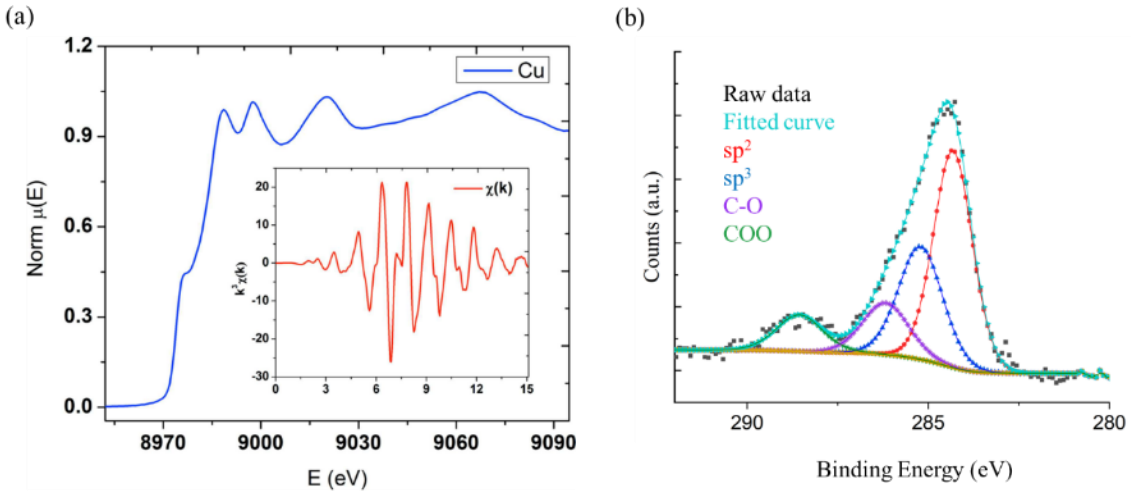

Figure 2.5. Example XAS and XPS data
(a) Copper foil XANES data of the Cu K-edge. Inset, k^3-weighted EXAFS data. Reproduced with permission of the International Union of Crystallography. (b) C1s scan of a Zr based metal-organic framework with deconvolution to separate carbon species.

2.7 X-ray Photoelectron Spectroscopy

X-ray photoelectron spectroscopy (XPS) is a surface-sensitive technique that provides information about the oxidation state and local binding of species near the sample surface. Irradiation of a sample with X-rays of a particular wavelength results in ejection of electrons whose energies are measured. Only electrons that actually escape the sample are measured in XPS. However, photo-emitted electrons can undergo further inelastic collisions, recombination, and other trappings which result in a decrease of photoelectrons which successfully escape. This attenuation has a higher degree of effect the deeper into the sample the X-rays penetrate, resulting in a surface-weighted signal. The inelastic mean free path of an electron within a sample may be calculated, often resulting in single digit nanometer depth penetration.[47] Thus, the information garnered from XPS comes near exclusively from the upper surface of a sample (with an average depth of 5 nm).

The detectors within a XPS instrument are able to measure the energy of the emitted electrons. The difference between known energy of the incident X-rays (Al K_α = 1486.7 eV) and the measured energy of the emitted electrons combined with a small work-function allows for calculation of the binding energy of the sample (Figure 2.5b). When combined with a monochromator and Al K_α X-rays, laboratory XPS instruments can achieve a working energy resolution between 0.4 and 0.6 eV. The binding energy of various elements are effected by the local coordination and oxidation state, resulting in chemical shifts to higher binding energy at higher oxidation states. Because these binding energies are reproducible, a catalogue of typical values for the identification of elements in a spectrum is available, similar to coreloss EELS. At the same time, the ability to scan various energy windows without much recalibration allow for the analysis of a wider variety of elements compared to EELS. The relative quantification of elements to yield an empirical formula for solid state samples is one of the common uses of XPS. Another capability of XPS is through depth profiling whereby destructive removal of the uppermost layers of a material allow for XPS measurements at various depths. Because the information in XPS comes primarily from the outermost surface, different depths can have different spectra to provide compositional information in a manner that the above techniques cannot. This kind of information is of particular relevance to core-shell nanoparticles and other materials that exhibit some kind of encasement.

However, the spectra are a summation of the scanned region which is in the micrometer scale. As such, while there is a vertical distinction in XPS, there is no spatial information in the x,y plane of the sample. Therefore, XPS is an effective tool for understanding to totality of surface behavior but lacks stronge capability for determining the horizontal locality of specific atomic behavior.

Chapter 3

Combining In Situ and Ex Situ Techniques to Investigate Post-synthesis Modification of a MOF

3.1 Background

Metal-organic frameworks (MOFs) have a porous and crystalline structure afforded by varying the composition of the building blocks, leading to applications such as gas storage and separation, catalysis, and proton-conducting membranes.[48–55] The MOF structure is constructed by joining metal centers (secondary building units) with organic linkers (typically aromatic chains caped with polar groups such as a carboxylate) to generate an open crystalline framework with a well-defined pore size. The many various metal centers and organic linkers have resulted in thousands of generated compounds whose chemistry are based on the structure.

Further adjustments to the chemistry of a MOF can be achieved through post-synthesis modification (PSM). For example, by incorporating organic guests, metal-organic complexes, and/or nanoparticles into the framework, the reactivity of the MOF is adjusted and additional catalytic sites can be added to the MOF. [56,57] The incorporation of nanoparticles as a catalytic site in the MOF structure is particularly useful by adding a new component into the framework which adds a new type of active site.[58–60] Other types of PSM that remove parts of the framework are done through thermal activation. The thermal activation can remove the occupying gas and free up acid sites inside the framework. However, the crystallinity is readily affected when

excess thermal energy is applied. Additionally, this adjustment to the framework through removal is not as well studied.

Typically, characterization techniques such as powder X-ray diffraction, infrared spectroscopy, thermogravimetric analysis, and electron microscopy are used to understand the structure and composition of a MOF. In situ characterization techniques are relevant for providing detailed information about the transformations that occur during a PSM. In situ FTIR in particular is used to easily track the formation and/or cleavage of bonds during a chemical process thanks to the distinct fingerprint region that shows a clear change in the peak intensity and shape as the reaction proceeds. FTIR focuses on light elements that can exhibit a change in the bond polarity but not heavier elements when incorporating nanoparticles into the framework. However, regular spectroscopic techniques only provide information about the chemical bonds and environment that are present without direct information about the overall structure which is crucial for MOFs. To that end, in situ TEM was used to examine the structure and chemical composition of a Zr based MOF during a heating PSM through imaging and spectroscopy. The in situ results were further validated with ex situ samples.

3.2 Methods

3.2.1. TEM Sample Preparation

Solid MOF powder dispersed in ethanol was dropcast onto a carbon TEM grid and onto a Protochips Fusion heating E-chip and allowed to air dry. In situ heating was performed on the Fusion E-chip inside the microscope with temperature ranges between 25 and 800 °C with a ramp rate of 1 °C/s at 10^{-6} Pa vacuum condition. Ex situ heating was performed in a vacuum oven with

a ramp rate of ~1 °C/s and an oxygen partial pressure <1/1000th atmospheric value. Ex situ samples were held at various temperatures for 200 minutes and then allowed to cool overnight (~12 hours) under vacuum.

3.2.2. TEM Characterizations

For TEM imaging, GrandARM at 80 kV for in situ work and on a JEOL 2100F at 200 kV for ex situ work was used. The in situ TEM imaging was acquired on a Gatan OneView camera. The MOF was imaged on GrandARM in STEM conditions described in chapter 1.2.3. For in situ vibrational EELS combined with STEM imaging during the same session, a Nion UltraSTEM 200 with High Energy Resolution Monochromated EELS Spectrometer (HERMES) at 60 kV was used. For the Nion microscope, a 38 mrad convergence semi-angle was used and the HAADF detector collected signal between 95 and 210 mrad for imaging conditions. Vibrational EELS was performed using a 33 mrad convergence semi-angle with a 0.5 meV/channel dispersion. Use of the monochromator reduces the probe current to 10 pA. The 30x30 pixel map was collected using Nion's inbuilt Swift software.

3.2.3 Ex Situ Characterizations

Raman spectra were taken on a Renishaw inVia Raman microscope using an Nd:YAG laser at 1064 nm for excitation. FTIR data was acquired with a Jasco 4700 with 4 cm^{-1} energy resolution and 100 total scans. XPS was performed on a Kratos AXIS Supra spectrometer with a monochromatic Al Kα (1486.6 eV) X-ray radiation source. A Shirley background was applied and

all components were fitted with a Voigt peak. A pass energy of 20 eV was used for all high resolved XPS spectra, resulting in a 0.45 eV energy resolution.

3.3 Initial Structure Characterization

The MOF archetype has a range of sensitivity to an electron beam depending on the composition and structure.[61–65] Therefore, initial imaging was performed with conventional TEM to discern the sensitivity of this Zr based MOF. The .cif structure file was provided by collaborators at City University of Hong Kong to compare with initial structure characterization results. The atomic model showed a hexagonal pattern between the zirconium oxide metal centers with the terphenyl-4,4-dicarboxylic acid linkers in between (Figure 3.1a). Initial imaging showed unexpected stability under the electron beam even under 500k magnification. The low magnification imaging indicated the flake-like nature of the MOF, forming a two dimensional sheet with weak interactions in between sheets. TEM imaging confirmed the presence of a hexagonal pattern which is attributed to the metal centers (Figure 3.1c, d). While individual atoms and the exact atomic location may not be determined solely from the TEM images, the comparison with the atomic model allows for a high degree of certainty that the dark regions in the TEM images correspond to the zirconium oxide metal centers. Electron diffraction was performed, indicating a hexagonal nature whose distance in reciprocal space corresponds to the inter-metal center distance in real space (Figure 3.1b). Therefore, the diffraction pattern for this crystalline material contains information about the heavier metal centers.

Due to the exhibited stability, the MOF was imaged under standard STEM conditions on GrandARM. Due to Z contrast, the metal centers show up more clearly here, exhibiting the

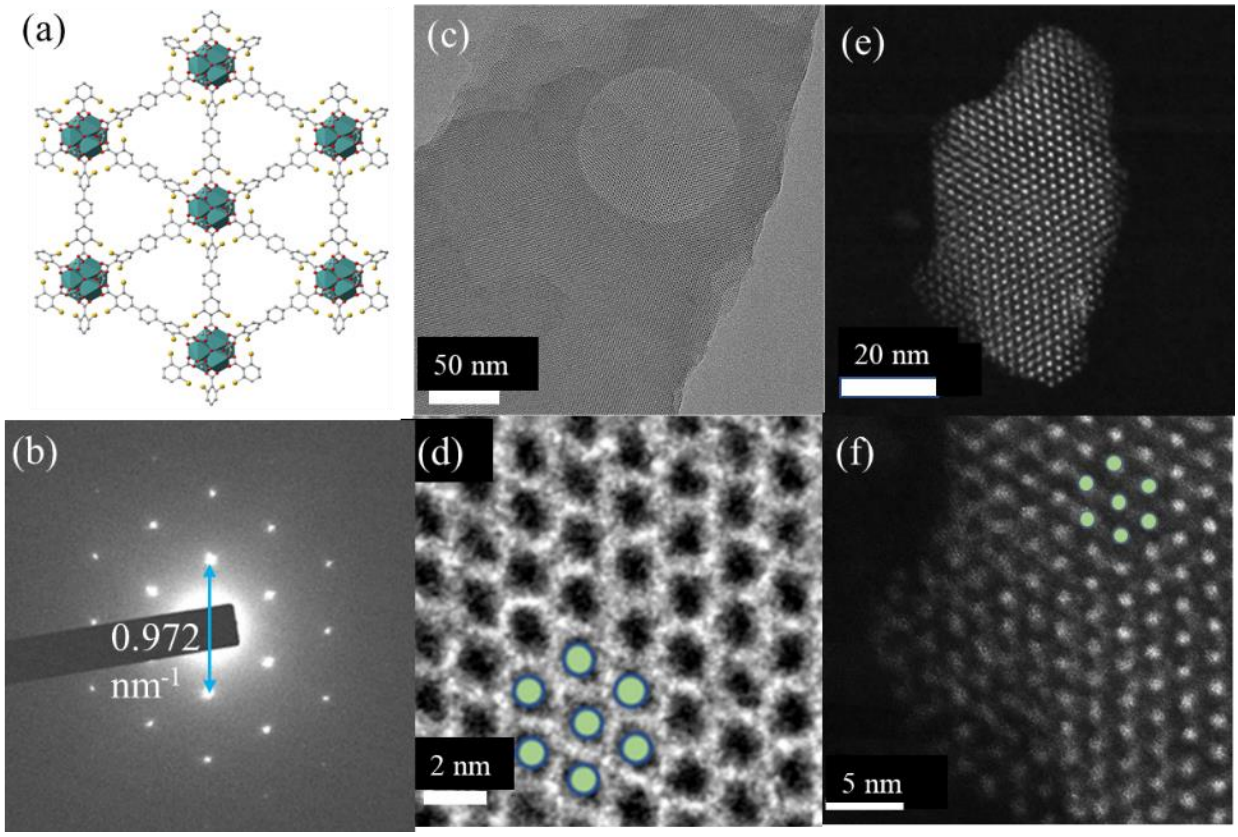

Figure 3.2. Structural characterization of a Zr based MOF
(a) Atomic model from powder XRD refinement. (b) Electron diffraction of the pristine MOF. (c) Low and (d) high magnification TEM image and (e) low and (f) high magnification HAADF image of a Zr based MOF. Zr=green, O=red, S=yellow, C=grey, H omitted for clarity. A hexagonal schematic representing the metal centers overlaid on (d) and (f).

hexagonal pattern that was observed under TEM conditions (Figure 3.1e, f). The direct interpretation of the signal intensity further confirms that the hexagonal pattern in TEM is correctly attributed to the metal centers. At higher magnification, the distance between metal centers was measured (2.1 nm) and faint hints of the organic linkers were observed in between the metal centers. However, prolonged exposure to the electron beam in STEM at higher than four million magnification resulted in destruction of the organic component and the metal centers visibly aggregating. Having ascertained the initial structure and the stability under TEM conditions, in situ experiments were designed to investigate a PSM utilizing thermal stimulus.

3.4 In Situ Characterization

In situ TEM imaging was performed on GrandARM at 80 kV from 25 to 800 °C with the beam off for ca. 15 minutes between temperature intervals before imaging. The hexagonal pattern remained up to 650 °C before the structure undergoes destruction above 700 °C (Figure 3.2a). Fast Fourier transformations (FFT) of the direct images were analyzed to understand the overall change to the framework based on the metal centers. The FFT of the observable lattice matched the distances measured in the electron diffraction, indicating that the FFTs could be used to track changes to the inter-metal center distances. The MOF showed a marked increase in the reciprocal lattice spacing between 250 and 300 °C and again between 500 and 600 °C (denoted by vertical dashed lines in Figure 3.2b). An increase in the spacing in the FFT corresponds to a decrease of the inter-metal center distance in real space, contrary to expectations of thermal expansion for most materials. A low magnification image series was also acquired to confirm the contraction of the MOF is not a

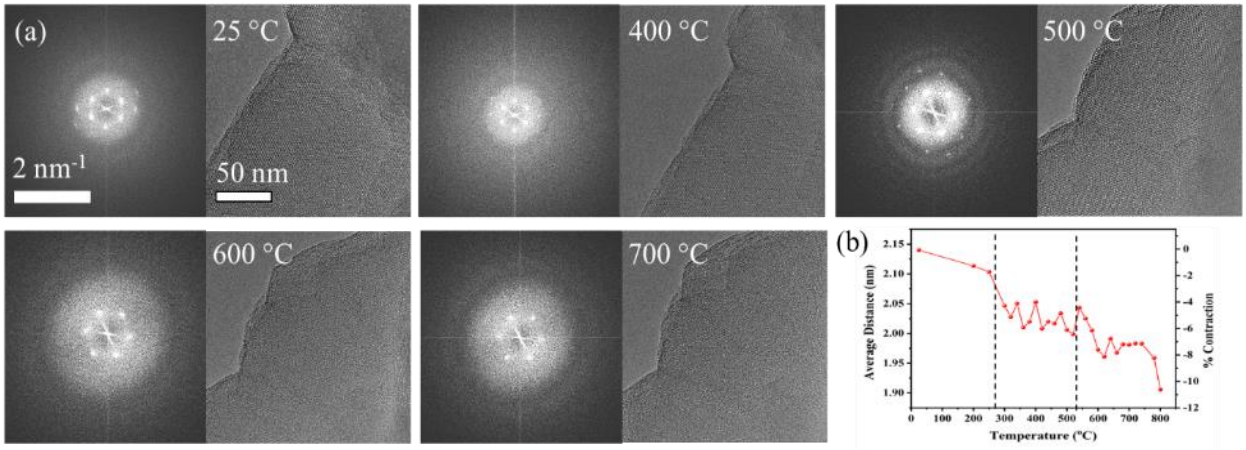

Figure 3.2 In situ heating TEM results
a) FFT and TEM images of the MOF structure at various temperatures. b) Plot of average measured (001) inter-metal center distances in the FFT, converted to real space, between 25 and 800 °C with the % contraction compared to 25 °C. Major stages of changes indicated with dashed vertical lines.

local phenomenon observed due to the electron beam (Figure 3.3). The electron beam was turned off except during the brief seconds necessary to acquire an image at each temperature. The low magnification STEM images acquired in situ confirm that the contraction phenomenon observed is due to the thermal stimulus and not induced by the electron beam. As such, an explanation about how contraction of a MOF framework led to the conclusion that chemical bond changes were involved during this PSM.

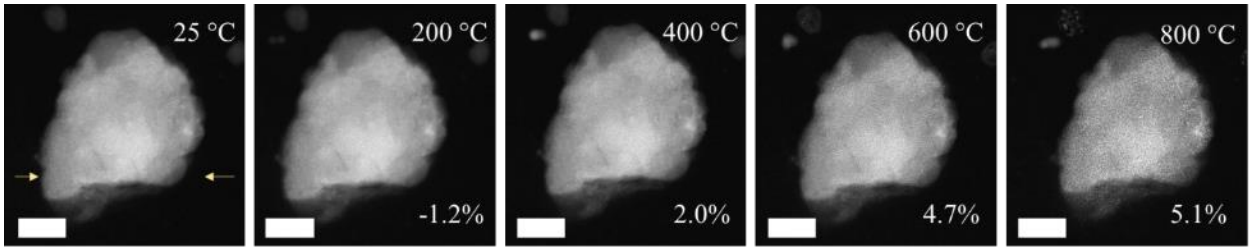

Figure 3.3. Low magnification in situ STEM results
Low magnification HAADF-STEM images acquired during in situ heating at various temperatures. The length of the MOF flake was measured between the yellow arrows and the percent contraction compared to 25 °C is shown in the bottom right. The beam was turned off during the experiment except when imaging at these temperatures. Scalebar, 100 nm.

To investigate the chemical bonding changes, in situ vibrational EELS was performed on a Nion UltraSTEM. The energy resolution achieved for the vibrational EELS measurements was 8 meV as measured by the full width half maximum of the zero-loss peak. The ability of vibrational EELS in electron microscopy to resolve different bonds is a powerful tool that was first reported in 2014 with the aid of the monochromator.[28] Following the same heating profile as the in situ imaging work, vibrational EELS spectra were acquired at various temperatures, normalized to the ZLP, as shown in Figure 3.4. Two major peaks located between 60-110 meV and 115-225 meV were observed. Correlative measurements from Raman and FTIR of the pristine MOF structure were used to assist the interpretation of the vibrational EELS results (3.5a). In the vibrational EELS spectrum, the large peak between 115-225 meV is attributed to the aromatic C-C bond and the

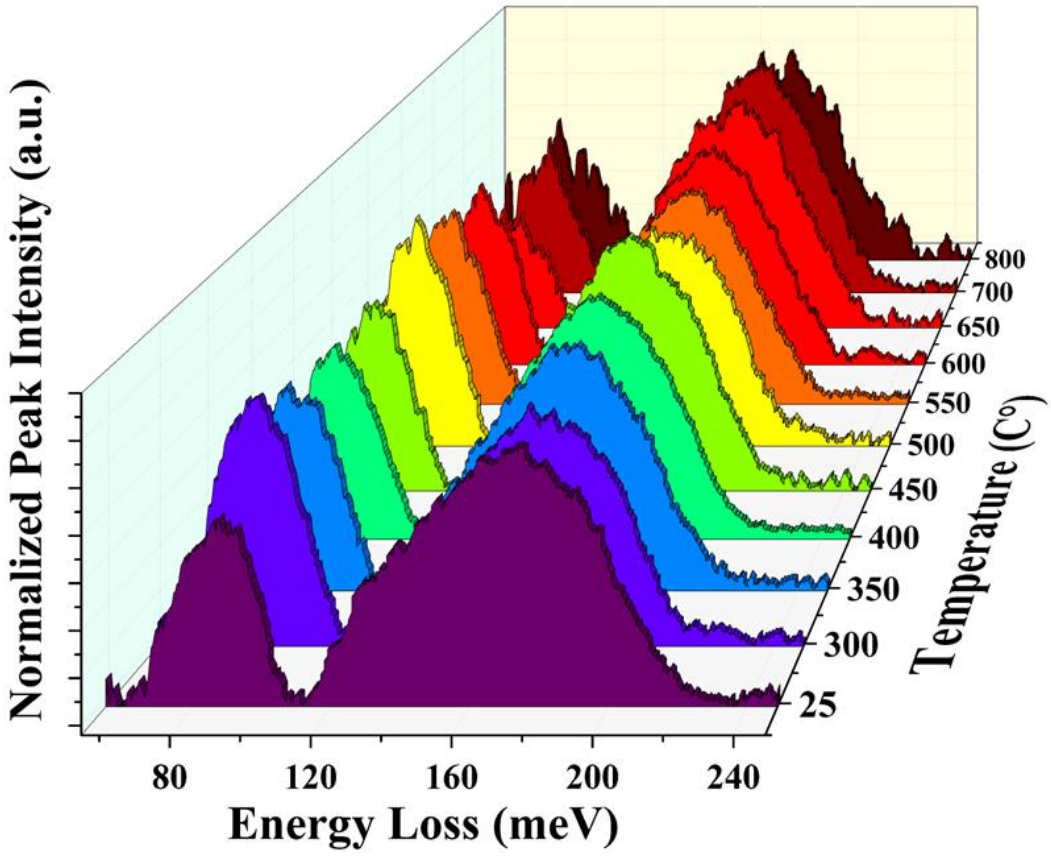

Figure 3.4. In situ vibrational EELS results
In situ vibrational EELS spectra at different temperatures observing chemical bond changes. The peak from 60-110 meV is attributed to the C-S and S-S bonds. The peak from 115-225 meV is attributed to C-C and carboxyl groups.

resonance stabilized carboxyl group. Chemical bonds with heavier elements exhibit a peak at a lower energy and thus the smaller peak at 60-110 meV is a mixture of the C-S and S-S bonds.

By looking at the large peak centered at 170 meV before and after heating, the MOF structure indicates the presence and relative quantity of C-C and carboxyl bonds are mostly unchanged (Figure 3.6a). However, the peak associated with C-S and S-S bonds shows a drastic reduction. The better stability of the aromatic bonds (124 kJ/mol) was expected compared to sulfide bonds. A small decrease in the peak centered at 170 meV in Figure 3.6a was attributed to a decarboxylation process. Due to the relative abundance of the C-C bonds compared to the

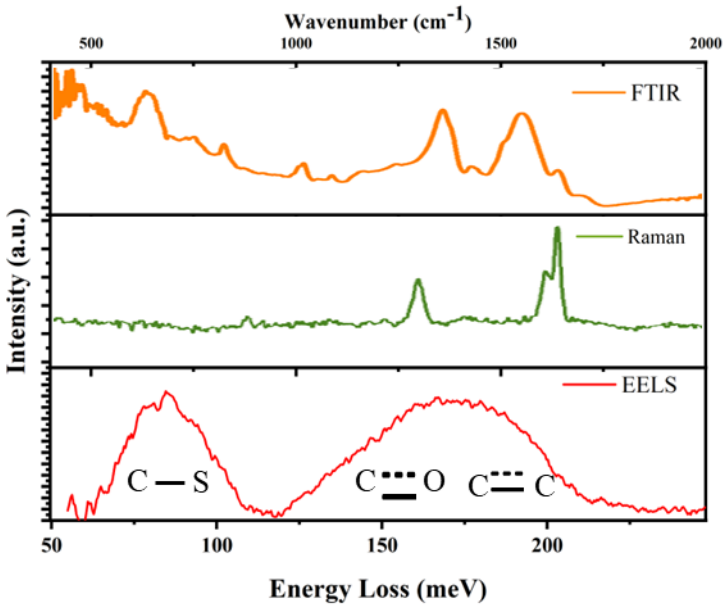

Figure 3.5. Comparative spectroscopic energies
Comparison of peak energies in FTIR, Raman, and vibrational EELS of the pristine MOF structure with important bonds indicated.

carboxylic group, the measured decrease in peak area is small and can be considered nearly constant. With the peak at 170 meV being nearly constant, the ratio of the two peaks in the vibrational EELS spectra reflects upon the amount of C-S and S-S bonds present in the framework at each temperature as seen in Figure 3.6b. Due to the relatively weaker bonds C-S and S-S bonds, high temperatures can result in a loss of the sulfur species from the framework. To check on whether sulfur remained even at higher temperatures, in situ coreloss EELS was performed on GrandARM with the same temperature range. Figure 3.7 shows that there is a decrease in the presence of the S $L_{2,3}$ edge, matching the loss indicated in the vibrational EELS spectra, sulfur remains in the MOF framework to the end. Thus, this indicates that there is a loss in the number of C-S and S-S bonds in the framework but the contraction to the structure must include sulfur in the final result. By combining the in situ results, we conclude that there is a two stage lattice contraction caused first by the formation of disulfide bonds at ~300 °C and a decarboxylation at ~500 °C which decreases the inter-metal center distance. The formation and cleavage of bonds,

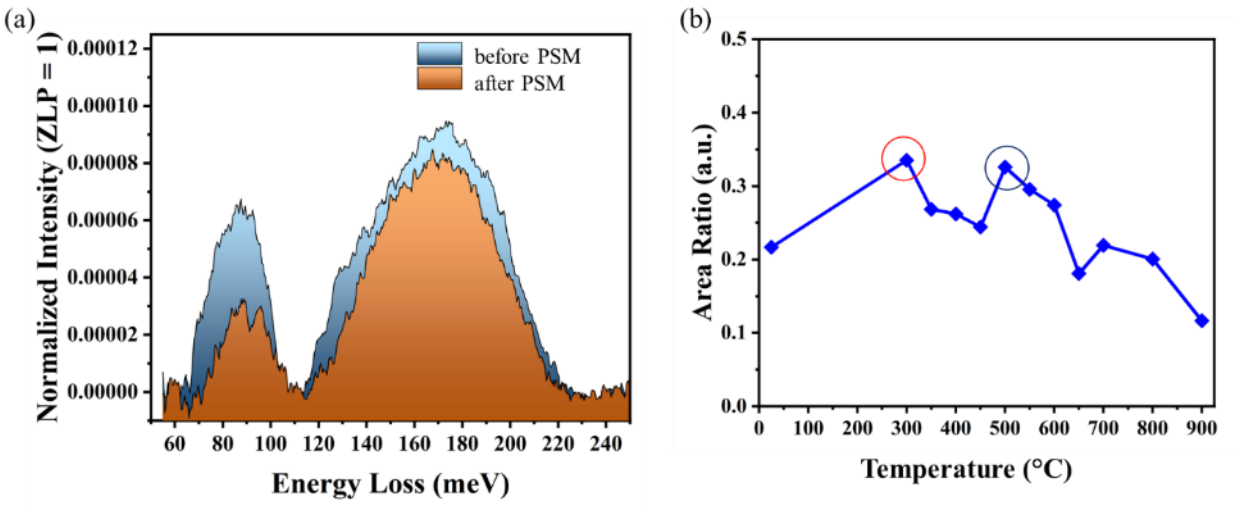

Figure 3.6 Vibrational EELS peak analysis
(a) A comparison of the two peaks detected in the vibrational EELS spectra before and after heat treatment, normalized to the ZLP. The peak associated with the C-S and S-S bonds is noticeable decreased. (b) Ratio of the two peak areas throughout the heating process with sudden increases (emphasized with the circles) that match with the temperatures where lattice contractions were observed.

observed directly with in situ microscopy during the PSM, changes the spacing of this MOF as seen by the TEM images.

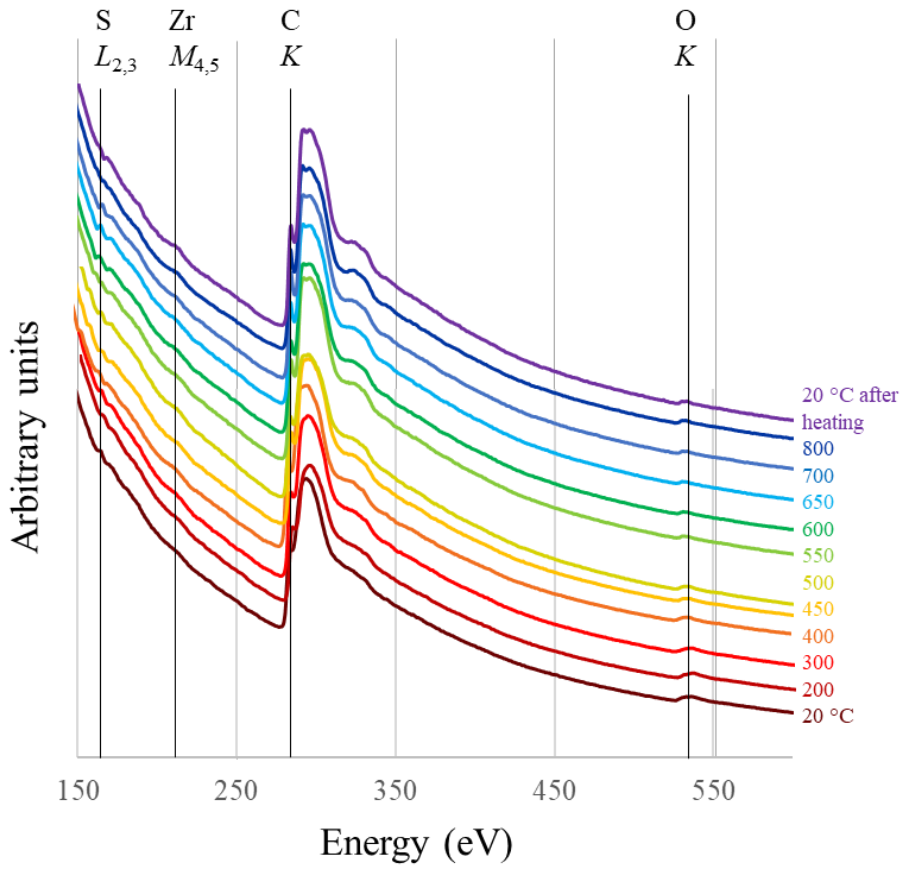

Figure 3.7 In situ coreloss EELS of the MOF
Coreloss EELS spectra throughout the heating process. The S $L_{2,3}$ edge (165 eV), Zr $M_{4,5}$ edge (180 eV, delayed maximum at 211.5 eV), C *K* edge (284 eV), and O *K* edge (532 eV) are visible throughout the heating process. Normalized to the ZLP. Vertical offset for clarity.

3.5 Complementary Ex Situ Characterization

To confirm the in situ measurements, ex situ samples were heated to various temperatures in a vacuum oven for comparison with the in situ results through imaging, IR, and XPS. The physical appearance of the MOFs were clearly changed after heating, converting from a pale yellow shade to a more golden hue before transitioning to brown and grey (Figure 3.8). The grey powder after 600 °C is typical of pyrolysis which yields a greyish white product. An examination of the ex situ samples with HAADF-STEM imaging showed the maintenance of the hexagonal pattern up to 500 °C before undergoing a loss of distinct structure (Figure 3.9) in a similar manner to the in situ

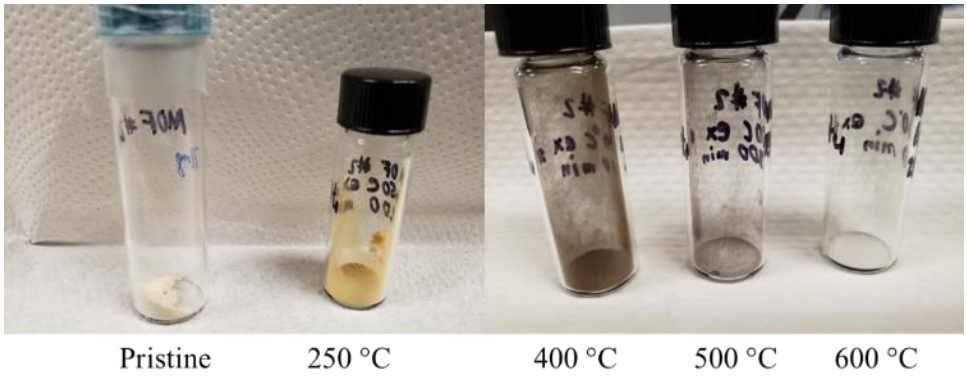

Figure 3.8. Appearance of ex situ samples
The physical appearance of the MOF sample after ex situ thermal treatment compared to the pristine MOF.

observations. The structural degradation at a lower temperature compared to the in situ results is attributed to the heating duration, which was for a longer period of time compared to the in situ work, due to the configuration of the vacuum oven.

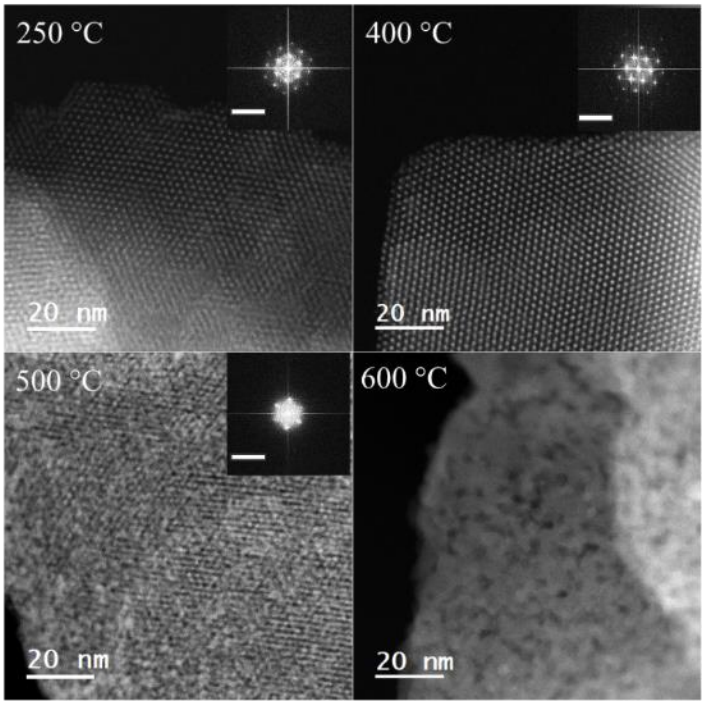

Figure 3.9 HAADF images of ex situ MOF samples
HAADF images of ex situ samples heated to various temperatures showing the maintenance of the hexagonal pattern from the metal centers up to 500 °C before undergoing pyrolysis as observed in the bulk sample. Inset, the corresponding FFT of the images. Inset scalebar, 2 nm^{-1}.

IR analysis of the different ex situ samples provide additional information about organic functional groups within the framework, namely the aromatic and carboxyl groups (Figure 3.10). The aromatic C-C peak slowly decreases in intensity as a loss of some weakly bound carbon occurs before a loss of aromaticity upon pyrolysis. Meanwhile, a small blueshift is observed on the peak initially observed at 1365 cm^{-1} while also broadening. The blueshift is indicative of a strengthening of the average C-O bond strength in the framework. The decarboxylation would reduce the resonance stabilization of the carboxyl group, leading the average C-O bond to trend closer to a double bond of a carbonyl group. The IR results show the bulk changes to the bonds within the MOF structure of the ex situ samples.

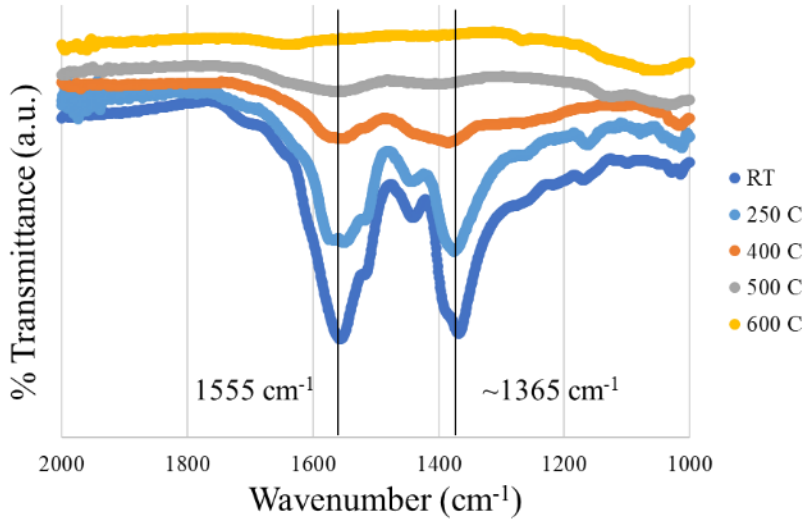

Figure 3.10 FTIR of ex situ MOF samples
FTIR of ex situ samples at different temperatures to track the prevalence of the aromatic stretch (1555 cm^{-1}) and the resonance stabilized carboxyl group (~1365 cm^{-1}). The destabilization of the carboxyl group during the decarboxylation process leads toward more double bond character in the C-O bond, resulting in a small blueshift. Slight vertical offset of clarity.

In addition to IR to inspect the bond vibrations, XPS was used to identify the nature of the chemical bonding present within the MOF. Considering the thickness of a single layer of this MOF is 7.3 nm as determined from the structure model, XPS is a suitable tool for probing the change in the overall electronic state of the various elements of the MOF. The penetration depth is estimated to be 6 nm for the C1s core level. [47] Using the same ex situ samples and the pristine MOF dispersed on a Cu foil, XPS spectra of C1s and S2p core levels were collected (Figure 3.11). In the pristine MOF, the C1s spectrum was deconvoluted into four components located at 284.4 eV, 284.8 eV, 286.2 eV, and 288.5 eV, attributed to sp2 C-C, sp3 C-C, C-O and C-S bonds, and O-C=O bonds, respectively (Figure 3.11a).[66–69] The C1s core level of the sample heated to 250 °C shows a decrease in the relative intensity of the C-C components compared to the pristine sample which is associated with the removal of carbon contamination. Annealing to 400 °C shows a decrease in functional groups involving oxygen. Further annealing to 500 °C completes the decarboxylation process, leaving the sp2 and sp3 carbons to be the dominant carbon species.

The S2p core level from the pristine MOF (Figure 3.11b) indicate a single spin-orbit pair ($S2p_{3/2}$ and $S2p_{1/2}$) with the expected splitting of 1.18 eV and area ratio of 2:1, located at 163.4 for the peak associated with $S2p_{3/2}$, a typical thiophenol binding energy. The following discussion of binding energy of the S2p peaks refer to $S2p_{3/2}$. The homogeneity of the sulfur bonds in the pristine structure is evident in the XPS result. In contrast, the S2p spectra of the thermally treated MOF samples show additional spin-orbit pairs with a higher binding energy. The presence of the peaks at a higher binding energy is indicative of a new chemical environment where sulfur has less electron density, be it through a change of oxidation state or through bonds with more electronegative elements. Here, fitted spin-orbit pairs at 164.2 eV and 167.6 eV for the sample heated to 250 °C are attributed to diphenyl disulfide and/or dibenzothiophene and diphenyl

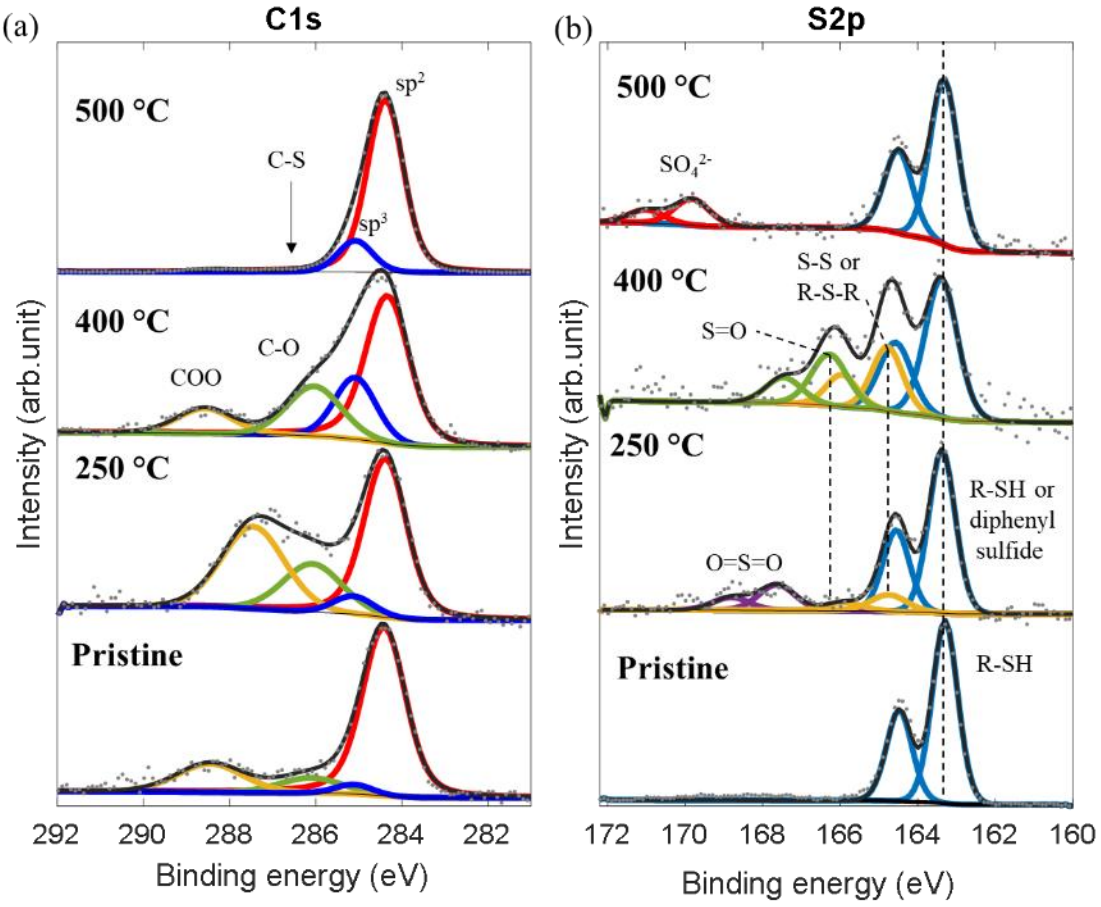

Figure 3.11 XPS of the ex situ MOF samples
(a) Carbon 1s and (b) sulfur 2p XPS components of ex situ MOF samples at various temperatures indicating the changing carbon and sulfur species. Samples were taken on copper foil. Binding energy was calibrated to adventitious carbon (284.4 eV).

sulfone, respectively. The unambiguous identification of diphenyl sulfide formation at higher temperatures cannot be made here due to overlap with thiophenol components (binding energy of 163.4 eV). The formation of the sulfone is likely a result of the oxidation of diphenyl sulfide, hinting at the presence of such a species. At 400 °C, the S2p spectrum was resolved into multiple spin-orbit pairs with the peak at 166.2 eV fitting with values for sulfoxide groups.[70] Further heating to 500 °C show that over 80% of the chemical environment of observed sulfur comes from one (or two highly overlapping) components centered at 163.4 eV with an additional sulfate peak at 169.9 eV comprising the remainder of the sulfur. Through this series of ex situ samples, the

sulfur chemical environment was observed to undergo an evolution, yet the overall hexagonal pattern was retained prior to pyrolysis.

3.6 Discussion and Conclusion

Combining the in situ and ex situ results, the transformation of the organic linker in the MOF becomes evident. Starting with from a pristine structure (Figure 3.12, structure **1**) as observed through TEM and STEM imaging, the FFTs of the in situ TEM images indicate a contraction of the lattice spacing in real space, contrary to expected thermal expansion. The contraction can be attributed to a change in the bonding of the organic linker while maintaining the hexagonal lattice pattern of the pristine MOF. During the initial heating, the S-H bond, the most reactive bond in the framework, breaks and reforms as a disulfide. In the case of alkane thiols, H_2S loss can occur, forming an alkene which further reacts to form a thioether.[71] In the case of this MOF, the formation of an alkene is suppressed by the aromatic rings. Instead, the proximity of the sulfur atoms favors the formation of a disulfide bond (Figure 3.12, structure **2**) as evidenced by

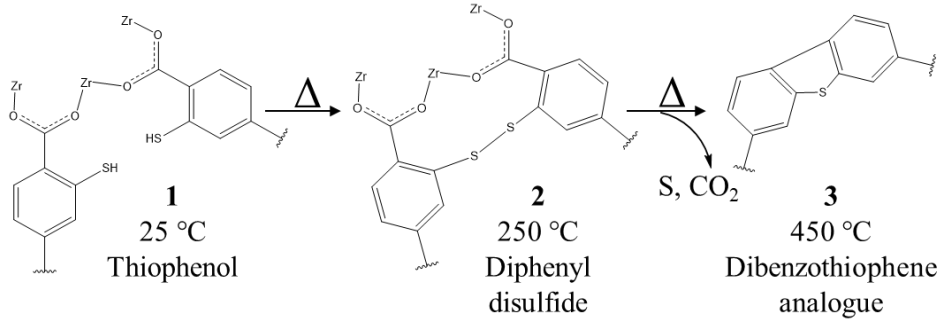

Figure 3.12 Schematic of the MOF transformation
The pristine structure, 1, forms a cross linker through disulfide bonds, 2, at an elevated temperature. Further heating causes cleavage of the disulfide bond and decarboxylation, leading to formation of a strained dibenzothiophene analogue, 3.

vibrational EELS and XPS. Additional side products that can form include diphenyl sulfide analogues. Further thermal treatment at higher temperatures leads to the cleavage of the disulfide bond and a decarboxylation process as evidenced by IR and XPS. As a result, the organic linkers come together to cyclize into a dibenzothiophene analogue, an aromatic product (Figure 3.12, structure **3**). The thiophene formation has a high degree of stability due to aromaticity and retains sulfur in the framework to the end of the in situ heating process, matching the in situ coreloss EELS results. The covalent merging of the adjacent organic linkers also serves to further contract the lattice spacing while maintaining the hexagonal lattice pattern as seen in the in situ and ex situ images. The linear shape of the terphenyl-4,4-dicarboxylic acid structure of the linker, as compared to more rigid linkers such as a tetrapod, enable a degree of flexibility in the plane of the MOF sheet whilst undergoing bond break and formation. Extensive thermal treatment does lead to a gradual degradation of the framework, indicating that proper control of the PSM is a necessity. The cleavage and formation of bonds during the in situ thermal treatment, as revealed through direct imaging and vibrational EELS, matches with the structural changes observed at the bulk.

Tracking the cleavage and formation of a chemical bond during in situ heating that results in structural changes provides insight into the transformation. Unlike traditional spectroscopic techniques such as IR and Raman, the strength of in situ imaging and vibrational EELS lies in the ability to track structural changes along with the corresponding bond changes rather than taking snapshots of a quenched reaction which may miss important intermediate stages. Additionally, some reactions may not be possible to quench, only allowing for snapshots of the beginning and end when performed ex situ. This is of particular relevance to MOFs where the crystalline structure has a strong determining factor to the characteristics, be they desirable or undesirable. Here, we observe a sequential lattice contraction which was explained by a combination of in situ imaging

and vibrational EELS. The initial observations allow for a continuous view of the entire transformation to further examine in detail. By understanding the stages in a PSM, finer control of the resulting structure can be achieved. The periodicity of a MOF means that small changes with the organic linker can repeat throughout the framework which are observed directly with in situ electron microscopy.

Dr. Muqing Li and Prof. Zhengtao Xu provided the synthesized MOF, .cif file, FTIR data, and Raman data. Dr. Chaitanya Gadre performed the vibrational EELS acquisition and vibrational EELS processing and jointly acquired FTIR and Raman data of the ex situ samples. Dr. Wenpei Gao helped design and supervised the in situ TEM imaging. Dr. Xingxu Yan helped with discussion about the vibrational EELS results. Dr. Djawhar Ferrah acquired the XPS data and assisted with the deconvolution in CasaXPS.

Chapter 4

Monitoring How Pt Influences H_2 Surface Reactions on Pt/CeO_2 Powder Catalysts

4.1 Background

Ceria (CeO_2) has been extensively studied and utilized as a heterogeneous catalyst and as a support for noble metals.[72] Dissociated hydrogen on the ceria surface can participate in selective hydrogenation or dehydrogenation reactions.[73–75] Additionally, dissociated hydrogen induces the reduction of Ce^{4+} to Ce^{3+} and the formation of oxygen vacancies (V_o) at the surface which then facilitate the adsorption and activation of other reactants.[76–79] The pretreatment of doped ceria has been known to improve catalytic activity.[80–83] Therefore, a fundamental understanding of the H_2 activation mechanism on ceria and the resulting surface chemistry lends to further improvements to surface activation without undesired aggregation.

Surface science studies into ceria have shown that platinum-group metals (PGMs) promote the interactions between H_2 and the ceria surface by dissociating H_2 and spilling over H to the ceria surface.[84–88] However, the mechanistic picture of powders with a high surface area may not be exactly the same as the surface science studies due to various features such as variations in the surface and the existence of ceria-ceria particle boundaries. Most reports assert that V_o (and the associated Ce^{3+}) localize around the PGM doped on the ceria surface.[77,89–93] However, the influence of Pt on the elementary steps involved in V_o formation on the ceria surface remains

lacking. Furthermore, direct measurements of Ce^{3+} spatial distribution in a non-ideal PGM/ceria case have not been shown. While it is appreciated that PGM induced hydrogen spillover has been used to influence the ceria surface, there remains more to be discovered about the process for powder catalysts. Information about the PGM/ceria surface reduction mechanism and the distribution of the Ce^{3+} would go toward filling this void.

4.2 Methods

4.2.1 Synthesis of Pt(x)/CeO_2

High surface area ceria and γ-alumina (Al_2O_3) was purchased from US Research Nanomaterials and used as the support in this work. A series of high surface area powdered Pt(x)/CeO_2 samples were prepared, where x denotes the mass percent of Pt to CeO_2. Pt weight loadings between 0.0005-2 wt% were used to form single atoms or nanoparticles on the ceria surface (Figure 4.1). Strong electrostatic absorption was used following previously reported synthesis methods to deposit Pt on the ceria surface. The dried Pt/CeO_2 was then calcined at 450 °C in dry flowing air for 4 hr. The Pt-free ceria was also oxidized at 500 °C in dry flowing air for 2 hr. Pt/CeO_2 was also physically mixed with ceria after calcination (1:19, 1:49, 1:99 ratio) using a vibratory mixer to achieve a low Pt weight loading with Pt nanoparticle species.

4.2.2 Gas Cell Preparation and Parameters

Samples were dropcast onto a Protochips Atmosphere E-chip configured for STEM. Pre- and post-in situ imaging were preformed using a Protochips Inspection holder. In situ experiments were

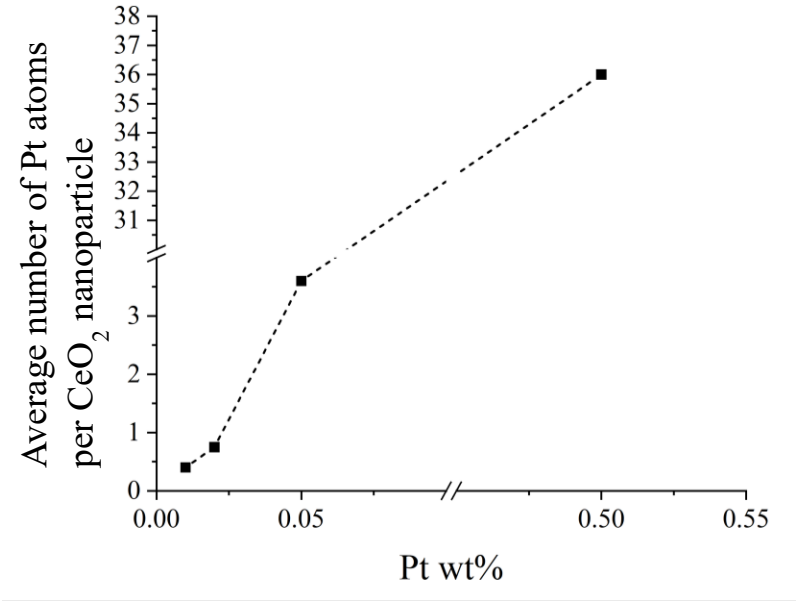

Figure 4.1. Pt weight loadings on CeO_2
Average number of Pt atoms per CeO_2 nanoparticle based on initial weight percent, loaded via strong electrostatic adsorption

performed using a Protochips Atmosphere 210 gas cell system with 0.1 cm^3/s flow rate at 200 Torr. Pure Ar, 5 vol% H_2/Ar, and 20 vol% O_2/Ar from Airgas (research grade) were used for the in situ work. After assembly, prior to imaging, the environment within the gas cell was pump purged five times at 200 °C to remove residual atmospheric oxygen and carbon. For the sequential reduction-oxidation-reduction experiment, the gas cell was exposed to H_2 for 1 hr before pump purging the gas cell five times with Ar and swapping the gas flow to O_2 for 1 hr and finally swapping back to H_2 with a pump purge process. While pump purging, the electron beam was turned off.

4.2.3 In Situ EELS Acquisition and Post-acquisition Processing

EEL spectra were collected using a Gatan K2 direct electron detector with an energy dispersion of 0.250 eV/channel on GrandARM. Spectra were calibrated to the N *K* edge of the SiN_x membrane on the E-chip. 50x50 pixel maps with 0.1 s dwell time were used to generate the EELS mapping

images. 10x10 pixel maps with 0.05 s dwell time were used to measure the Ce oxidation state at the particle boundary in the sequential reduction-oxidation-reduction experiment. Principal component analysis (PCA) was used to improve the signal-to-noise ratio and then a power law background subtraction was applied to the spectra. A double arctan background was then applied and the Ce M_5 and M_4 peaks were fitted using a Voigt peak. From there, the Ce M_5 and M_4 peak heights were measured and the M_5/M_4 ratio at each pixel was calculated. To generate the EELS maps, the M_5/M_4 was plotted, and a Gaussian blur was applied with sigma = [5,5]. Due to inclusion of vacuum regions in the scanned region, a cutoff threshold for total counts was applied to each pixel to match with the corresponding HAADF image whereupon a pixel below the threshold had the M_5/M_4 set to zero. Custom Python code was used for the PCA, double arctan background subtraction, Voigt peak fitting, M_5/M_4 ratio measurements, threshold application, and Ce oxidation state mapping.

To quantify the Ce^{3+} concentration of a Ce oxidation state map, a background value was acquired on CeO_2 at 200 °C under Ar or H_2. At 200 °C, pure CeO_2 is not observed to consume H_2 according to H_2-temperature programmed reduction (TPR). The average M_5/M_4 ratio from these maps at 200 °C were consistently higher than the expected Ce^{4+} value of 0.91. This phenomenon of increased M_5/M_4 ratio was seen repeatedly in multiple samples for both gaseous environments. As such, the difference between the measured values (0.925±0.023 for H_2, 0.915±0.004 for Ar) and the expected value of 0.91, due to instrumentation, was used as a correction factor for all EEL spectra and maps as applied to the relevant gaseous environment.

4.3 Ex Situ TEM Investigation

Low and high magnification HAADF images were acquired of the commercial ceria, Pt(0.01)/CeO_2, and Pt(2)/CeO_2, representing samples with no Pt, Pt single atoms, and Pt nanoparticles (Figure 4.2). The low magnification images show regions of a uniform intensity, hinting at a single layer of ceria nanoparticles. EELS thickness maps confirm the uniformity of these regions (Figure 4.3). Given that commercial ceria as purchased from US Research Nanomaterials is 10-15 nm in diameter, these regions consist of a single layer of the ceria nanoparticles. These single layer regions were selected for in situ observations due to the uniformity as well as being the minimum thickness possible.

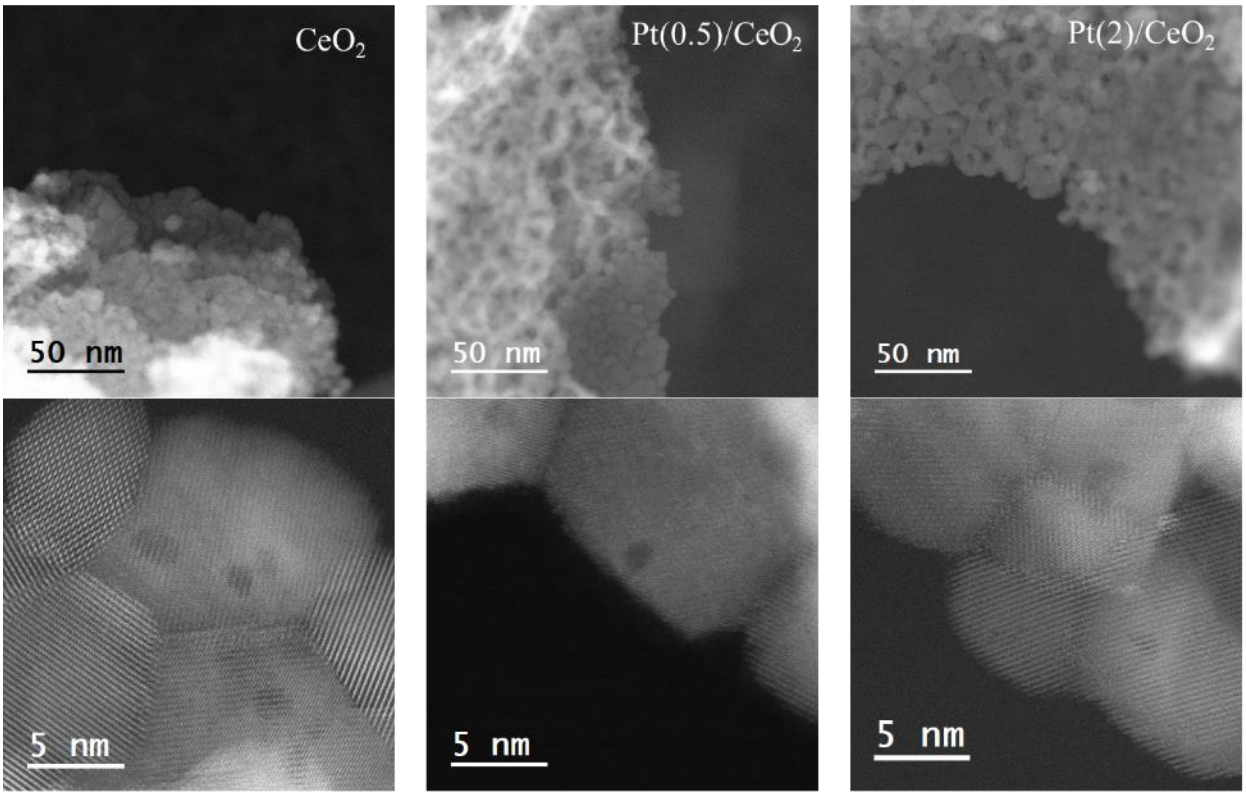

Figure 4.2. HAADF images of CeO_2 and Pt(x)/CeO_2
Low and high magnification HAADF images of CeO_2, Pt(0.5)/CeO_2, and Pt(2)/CeO_2 after calcination in dry flowing air. These samples represent Pt-free, Pt single atoms, and Pt nanoparticles on the ceria surface.

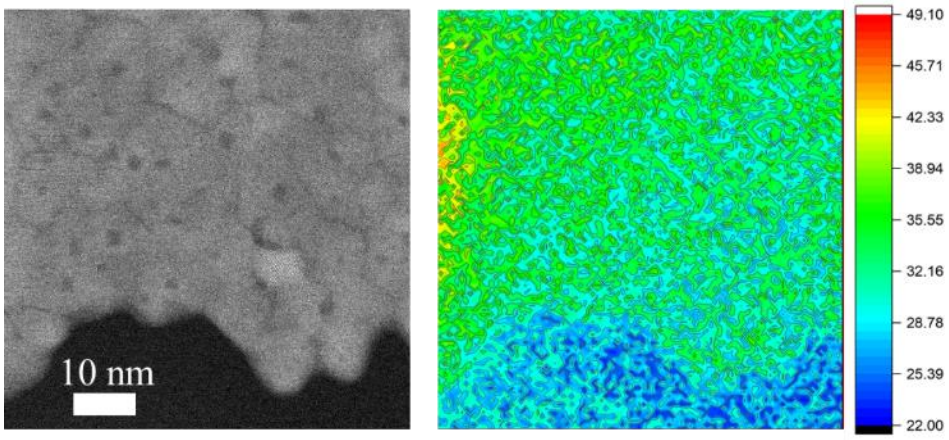

Figure 4.3 EELS thickness map of CeO_2
HAADF image (left) and corresponding EELS 100x100 pixel contour plot (right) of material thickness in nm. The silicon nitride membrane thickness is also included (blue region in contour plot) in the measurement.

4.4 In Situ Imaging and EELS

To acquire spatial information about the changes to the cerium oxidation state and the locality of the cerium surface reduction, coreloss EELS was utilized. Due to the nature of raster-scans in STEM, each pixel contains an individual EEL spectrum, providing information about the electronic state of materials at each pixel. Oftentimes, the spatial resolution in EELS is limited by the probe size. With in situ experiments using MEMS based E-chips, the electrons must also pass through two SiN_x membranes, adding ca. 80 nm of thickness, albeit with a light material. To preserve the spatial resolution, a direct electron detector was used which has 10 to 100 times higher sensitivity compared to a charge-coupled device (CCD) system for EELS measurements. Because the M_5/M_4 is highly sensitive to small variations that can show up at the peak center, sufficient signal-to-noise is a necessity. To that end, PCA was used to improve the signal-to-noise before peak fitting was applied. While an additional potential method to improve EELS data quality is by increasing electron dose, such a method may result in beam damage and was not elected to be used in this work. Figure 4.4 shows a comparison of the signal-to-noise of EEL spectra for an individual

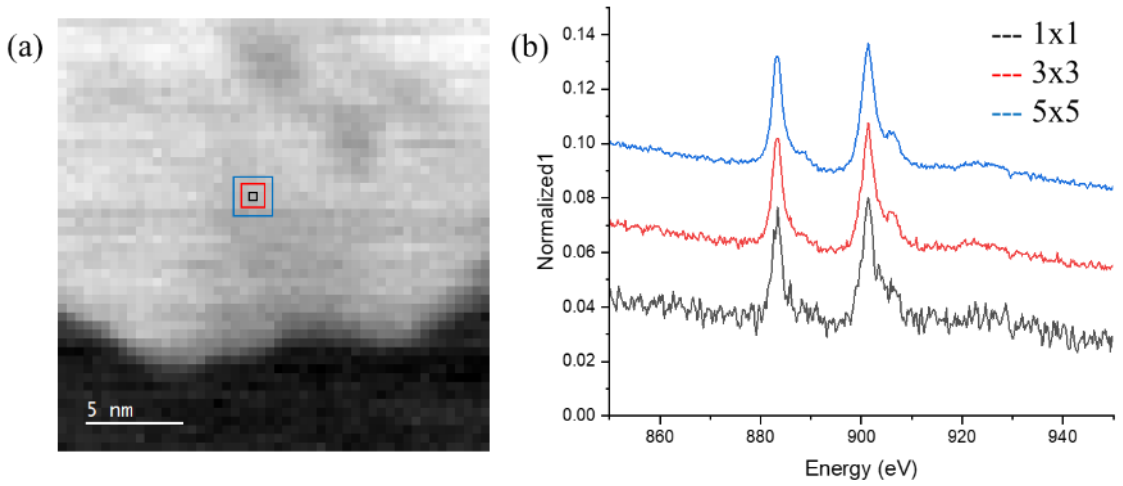

Figure 4.4. EELS pixel map and data quality comparison
(a) 50x50 pixel EEL spectrum image of Pt(2)/CeO_2. (b) Normalized EEL spectra from 1x1, 3x3, and 5x5 pixel boxes in (a) showing the signal-to-noise quality of the EELS data. Vertical offset for clarity. The variation of the peak height in the 1x1 box is evident. One pixel length is 0.44 nm.

pixel versus summation of a few pixels. The single pixel has a very noisy M_5 peak center. Thus, a denoise and peak fitting was a necessity for calculation of the Ce oxidation state and corresponding Ce^{3+} percentage maps.

In situ HAADF images and EELS spectra were acquired and post-acquisition process was applied. Ce^{3+} has an M_5/M_4 ratio of 1.31 while Ce^{4+} was a ratio of 0.91.[90,94–96] Because TEM shows a projection of materials, the summation of cerium atoms at each pixel results in a linear relationship of the oxidation state as expressed by the following equation:

$$0.91 * (1 - x) + 1.31 * x = y \tag{4.1}$$

where x is the percentage of Ce^{3+} at a pixel and y is the measured M_5/M_4 ratio at the pixel. A representation of the difference in measured ratio can be seen in Figure 4.5a where both a difference in peak height and a shift to a lower energy was observed for the pixels with more reduced cerium.

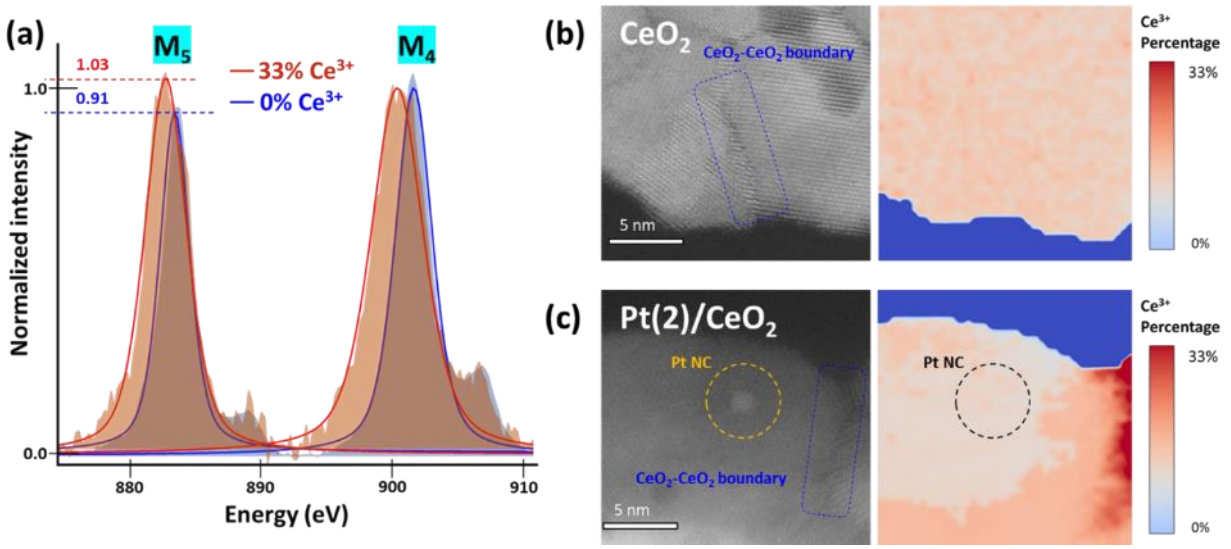

Figure 4.5. Difference in Ce^{3+} concentration observed in situ
(a) Representative EEL spectra with different Ce^{3+} concentrations after PCA, power law and double arctan background subtraction, normalized to the Ce M_4 peak height. Processed data are represented by the shaded area and fitted Voigt peaks are represented by the solid lines. HAADF images and corresponding EELS maps of (b) pure CeO_2 after in situ reduction at 450 °C for 1 hr and (c) Pt(2)/CeO_2 with Pt nanoparticles after in situ reduction at 400 °C for 1 hr. 10 Torr of H_2 partial pressure was used. In the EELS maps, a gradual change from light blue to red indicates an increase in Ce^{3+} concentration. Darker blue represents vacuum regions with only silicon nitride membrane.

A high magnification HAADF image and the corresponding Ce^{3+} percentage map can be seen in Figure 4.5b and c for comparison between ceria with and without Pt. As seen with the Pt-free ceria, the ceria surface became somewhat evenly reduced with no distinction of Ce^{3+} accumulation. In contrast, ceria with Pt loaded on the surface exhibited distinct differences. As seen with the Ce^{3+} percentage map, there was an accumulation of Ce^{3+} at the CeO_2-CeO_2 boundary but no accumulation adjacent to the Pt nanoparticle. Another region of Pt(2)/CeO_2 was observed during the same experimental session at low magnification and the change in the surface Ce oxidation state can be seen, with heavy concentrations at the boundaries between ceria nanoparticles but not at every projection of a thin curvature (Figure 4.6).

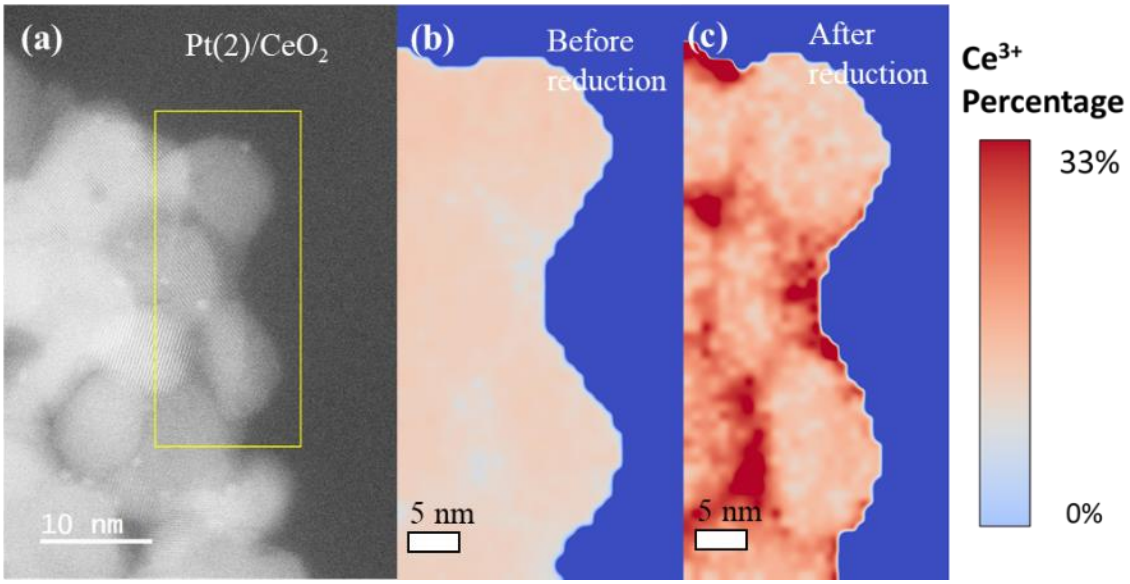

Figure 4.6. Pt(2)/CeO_2 before and after in situ reduction
(a) HAADF image of Pt(2)/CeO_2 with visible Pt nanoparticles. The EELS maps (b) before and (c) after in situ reduction with H_2 at 400 °C for 1 hr. 10 Torr of H_2 was used for the reduction. The region selected for the EELS acquisition is marked with a yellow box in (a).

As observed with Pt nanoparticles on a ceria surface, the Ce^{3+} accumulated at the boundaries between particles. A similar result was also observed when Pt single atoms dispersed on the ceria was used to study the surface reduction mechanism. Namely, single atoms of Pt on Pt(0.01)/CeO_2 were located prior to in situ reduction (Figure 4.7a). EELS oxidation state mapping were generated before and after 5% H_2 reduction whereupon the aggregation of Ce^{3+} was found to be at locations where there was overlap between ceria nanoparticles (Figure 4.7b, c), as seen by the brighter intensity in the HAADF image.

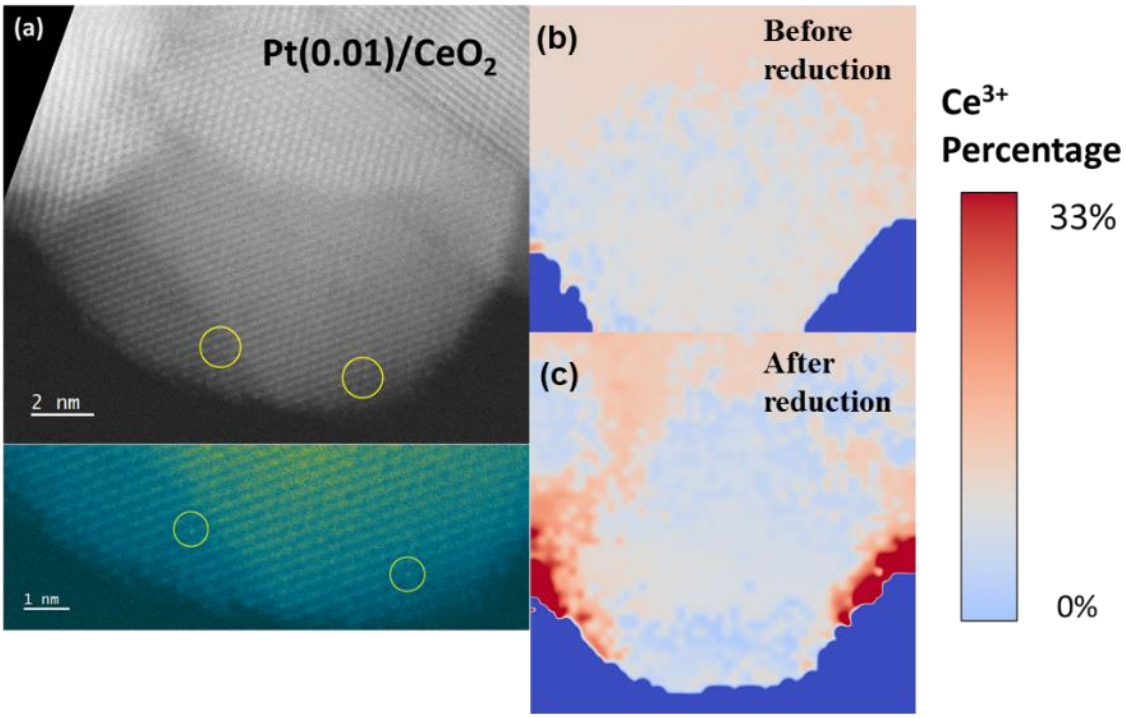

Figure 4.7. Pt(0.01)/CeO_2 before and after in situ reduction
(a) HAADF image of Pt(0.01)/CeO_2 with Pt single atoms (yellow circles). Bottom, high magnification false color image to emphasize the presence of the Pt single atoms. The EELS maps (b) before and (c) after in situ reduction with H_2 at 400 °C for 1 hr. 10 Torr of H_2 was used for the reduction.

4.5 Discussion and Conclusion

The Ce oxidation state maps clearly indicated a spatial separation between where Ce^{3+} aggregated and where the Pt species were located. Further analysis was done using the EELS mapping. The spatially averaged Ce^{3+} concentrations were quantified for pure CeO_2, Pt(0.01)/CeO_2, and Pt(2)/CeO_2 samples and agree with estimates from H_2-TPR and H_2-FTIR (Table 4.1). The bulk Ce^{3+} concentration of 8.1% and 16.3% for pure CeO_2 and Pt(0.01)/CeO_2 in Table 4.1 represent a Ce^{3+} surface coverage of 0.53 and 1.07 monolayers, respectively. The amount of Ce^{3+} surface coverage suggests that surface Ce^{4+} remote from the Pt species (recall that Pt surface coverage is low) was reduced due to the hydrogen spillover. However, the high mobility of Ce^{3+} at 400 and

450 °C means formation of Ce^{3+} at the interface between Pt and CeO_2 followed by diffusion to the CeO_2-CeO_2 nanoparticle interface cannot be fully ruled out as a contributing factor. In addition, the EELS data cannot distinguish whether the Ce^{3+} that is visualized is associated with oxygen

Table 4.1 Comparison of Ce^{3+} concentrations from EELS vs. H_2-TPR and FTIR

Sample		Ce^{3+} concentration	
		from EELS (%)	from TPR and FTIR (%)
CeO_2	Before reduction	0.3	0[(a)]
	After reduction	5.9	8.1
Pt(0.01)/CeO_2	Before reduction	2.3 ± 0.5	0[(a)]
	After reduction	11.4 ± 3.0	16.3
Pt(2)/CeO_2	Before reduction	2.4 ± 0.2	0[(a)]
	After reduction	10.8 ± 2.9	18.7

[(a)] The Ce^{3+} concentration was determined to be 0 because the single beam intensity from Ce^{3+} in the FTIR spectra was 0 before reduction with H_2.

vacancies (V_o) or adsorbed hydroxide (OH^-_{ads}). However, because the catalyst was reduced in H_2, the OH^-_{ads} is likely to react and form H_2O and V_o, as indicated by FTIR. Together, the EELS maps with FTIR results suggest a large fraction of the Ce^{3+} aggregate at and around the boundaries between CeO_2 nanoparticles when Pt is present on the ceria surface, a conclusion quite distinct from the previous assumptions of Ce^{3+} localization around the Pt species as well as the behavior seen on pure CeO_2.

As seen with the EELS maps, the interaction between neighboring ceria nanoparticles was able to produce high concentrations of Ce^{3+} at the CeO_2 surface following H_2 reduction. As such, further investigation into this interplay was performed. A sequential reduction-oxidation-reduction experiment was done in situ and ex situ to acquire bulk measurements and spatially targeted

measurements. As seen in Figure 4.8a, there was no change between the first reduction and second reduction measured by H_2-TPR for CeO_2 (black and blue curves, respectively). In contrast, the

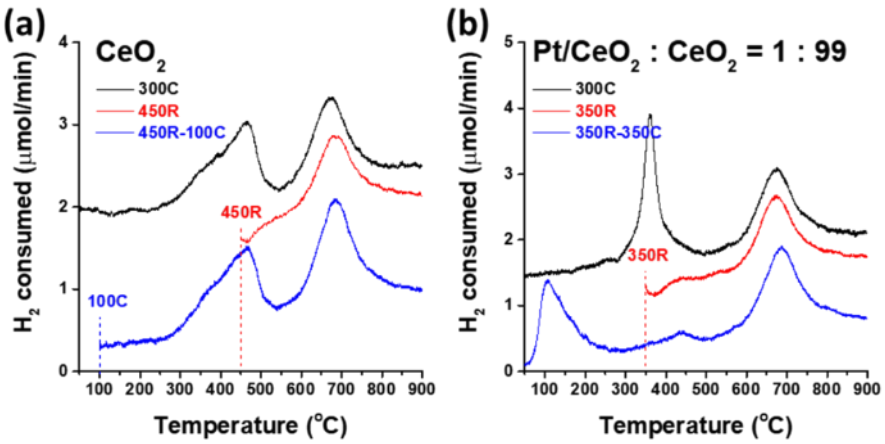

Figure 4.8. H_2-TPR of CeO_2 and Pt/CeO_2
H_2-TPR curves of (a) pure CeO_2 and (b) Pt/CeO_2, diluted with CeO_2 at a 1:99 mass ratio. Curves represent the measured reduction process after samples were oxidized at 300 °C (black), reduced (red), and sequentially reduced and oxidized (blue).

first reduction peak of Pt(1)/CeO_2, diluted with CeO_2 at a 1:99 ratio, for the first and second reduction exhibited a temperature decrease (Figure 4.8b, black and blue curves, respectively). Red curves in Figure 4.8a and b show that the surface reduction was complete after 450 and 350 °C, respectively. Similar temperature reductions for the peak associated with ceria surface reduction following sequential TPR cycles was observed with samples incorporating larger nanoparticles or single atoms, indicating that this change to the surface reduction process is not caused by an increased reducibility of the Pt species on the surface.

EELS and FTIR measurements were also taken of sequentially reduced-oxidized-reduced samples, showing an agreement with TPR results. EELS data, taken from the boundary between two nanoparticles, showed a faster rate of formation during the second H_2 exposure (Figure 4.9a). The FTIR results indicated that the entirety of the Pt(1)/CeO_2 powder exhibited faster formation rates

of OH^-_{ads} and Ce^{3+} during the second H_2 reduction (Figure 4.9b). Together, these results indicate that the hydrogen spillover from Pt species and the resulting Ce^{3+} localization near the boundaries between ceria nanoparticles are correlated and cause an irreversible change to the H_2 consumption kinetics of the material.

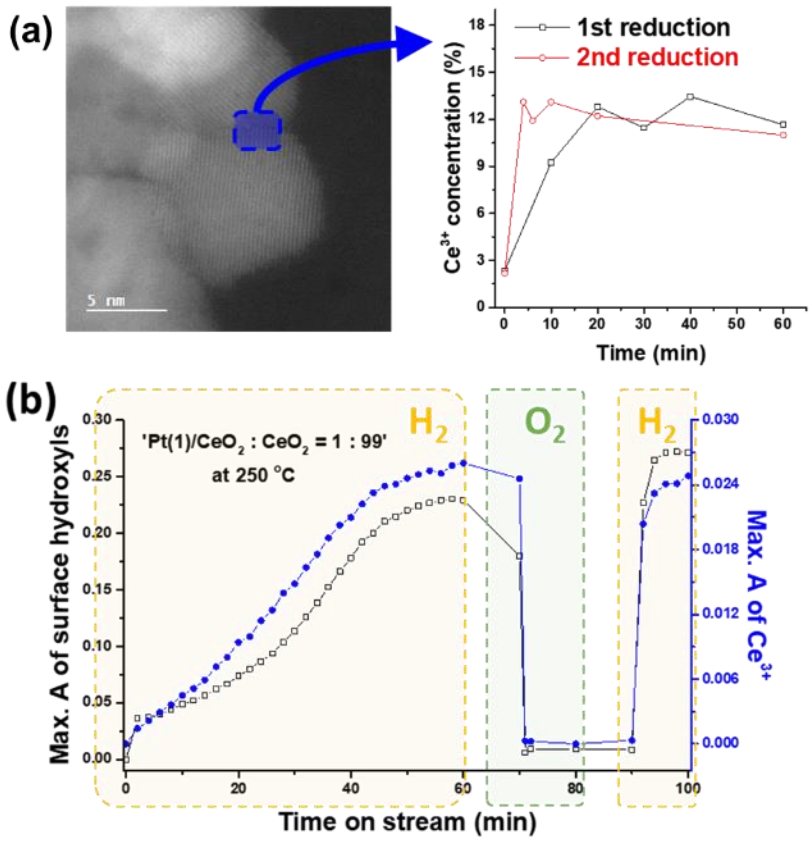

Figure 4.9. EELS and FTIR measurements of sequential reduction-oxidation-reduction (a) HAADF image of the region where the rate of Ce^{3+} formation was measured during the first and second reduction by using EELS. Sample was reduced at 400 °C with H_2 and then re-oxidized at 400 °C with 20% O_2 and then reduced again. (b) FTIR measurements of the absorbance peaks associated with surface hydroxyls (OH^-_{ads}) and Ce^{3+} during a sequential reduction, oxidation, and reduction process. As seen with both methods, the formation of Ce^{3+} occurs much more rapidly during the second reduction step.

To interrogate any potential structural changes, XRD, surface area measurements, and STEM imaging were utilized. XRD results showed no evidence of ceria aggregation, nor did surface area measurements indicate any change to the amount of exposed surface area before and after reduction. In contrast, analysis of the HAADF images via FFT indicated changes to the orientation of the nanoparticles. Using a medium magnification setting that includes many nanoparticles at random orientations, the resulting diffraction pattern will have ring-like features which are families of lattice planes through various rotations in space. This is analogous to amorphous material which have no directionality in real space and thus should exhibit circularity in reciprocal space. The FFTs of pure CeO_2 nanoparticles exhibit a large degree of circularity before and after in situ reduction with H_2 at 450 °C (Figure 4.10). Prior to exposure to H_2, Pt/CeO_2 exhibited the same circularity as pure CeO_2. However, after H_2 reduction, the circularity has been clearly diminished. Together, these results suggest a reorientation of the nanoparticles to produce aligned grains which can reduce the overall energy of a system. Of note is that lattice alignment between ceria

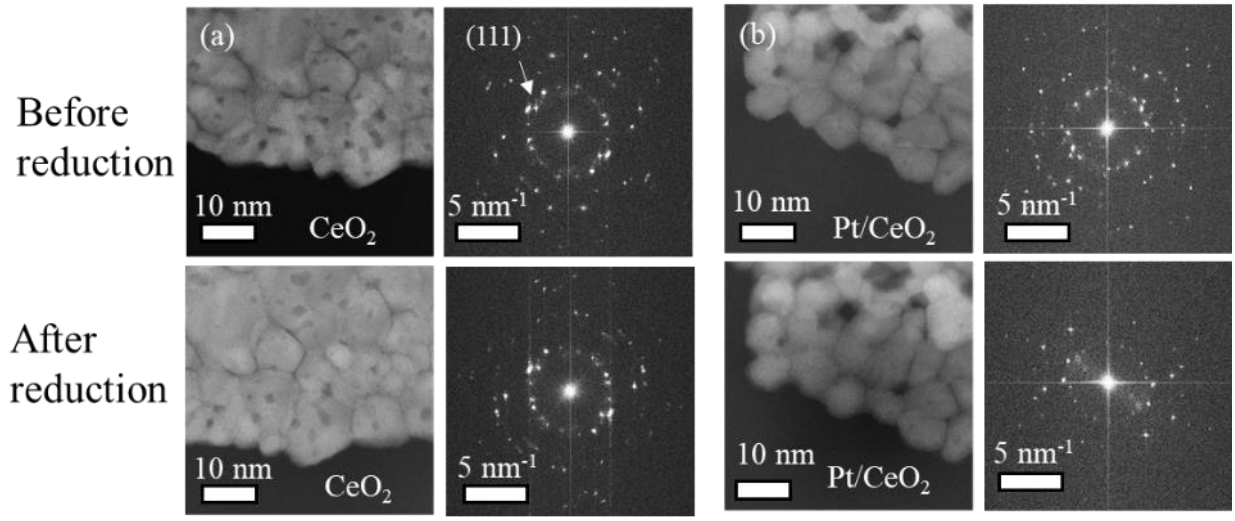

Figure 4.10. HAADF images and FFTs before and after in situ reduction
HAADF images and corresponding FFT of (a) pure CeO_2 and (b) Pt/CeO_2 before and after in situ reduction. The ring representing CeO_2 (111) at 0.31 nm^{-1} marked.

nanoparticles (often termed oriented attachment and having a relatively small activation barrier) and the removal of some surface oxygen are prerequisites for ceria sintering.[97–101] The activation barrier for the orientated attachment of ceria nanoparticles is reported to be 54 kJ/mol for ca. 2 nm CeO_2 and 95 kJ/mol for ca. 60 nm CeO_2, indicating that 8 nm CeO_2 have accessible barriers at the temperatures used in this study.[98–100] The underlying thermodynamic principle of nanoparticle sintering is to lower surface energy. Thus, it is likely that the nanoparticle orientation in Pt/CeO_2 samples undergo this phenomenon during H_2 reduction to lower the surface energy for these high surface area powders and the high hydrogen spillover facilitate the process. The interaction between ceria nanoparticles with aligned interfaces facilitate faster kinetics of H_2 consumption and lead to the increased total H_2 consumption seen with Pt(x)/CeO_2 samples.

It should be noted that while the EELS maps suggest that Ce^{3+} and V_o accumulate at the CeO_2-CeO_2 boundaries after H_2 reduction, a question remains as to where the H_2O formation occurs on the ceria surface. H_2O formation and Vo formation could occur directly at the boundaries, but they could also occur at the Pt-CeO_2 interface followed by migration of V_o to the CeO_2-CeO_2 boundaries. More research would be required to elucidate which mechanism is predominant, perhaps as the technology of EELS detectors improve to capture faster events. Another possible route to probe this question could be through the use of reducing agents that are less mobile than hydrogen (e.g., CO or hydrocarbons) to better understand how CeO_2-CeO_2 and Pt-CeO_2 boundaries participate in the V_o formation step.

Dr. Jaeha Lee synthesized the Pt(x)/CeO_2, performed the H_2-TPR and H_2-FTIR, performed XRD and surface area measurements, and provided discussions on the mechanism of ceria surface reduction. Dr. Chaitanya Gadre provided the Python code for PCA, EELS analysis, and ceria

M_5/M_4 ratio mapping. Dr. Wenjie Zang, Dr. Xingxu Yan, Dr. George Graham, Dr. Phillip Christopher, and Dr. Xiaoqing Pan provided guidance to the experiments and data analysis.

Chapter 5

Nanoscale Investigations in Solution with TEM

5.1 Liquid Cell Inside the Microscope

Similar to the gas cell seen in Figure 1.3, the liquid cell can be used inside the microscope to investigate liquid phase processes. Dissolution, electrochemical reactions, and catalyst synthesis are major processes that can be replicated from the benchtop to give insight into the nano- and possibly atomic scale.[102,103] However, there are additional considerations beyond what is encountered with a gas cell. The density of the fluid is higher in the liquid phase, causing a higher degree of interaction between the electron beam and the contents of the cell, resulting in some beam broadening and loss of spatial resolution. The size of some materials of interest also force the gap between the top and bottom chip to be larger than what is used in the gas cell, i.e. 200 or 500 nm spacers, to enable liquid flow. To combat the loss of spatial resolution, the membrane can be made thinner and made of a material that is more electron transparent compared to silicon nitride. To that end, graphene liquid cells are also employed but still have issues with broad robustness compared to silicon nitride.[104–108]

Besides the decrease in spatial resolution due to interaction with the intervening liquid, further limitations are present in the liquid cell that must be considered. The use of liquid places an inherent upper limit on temperature as evaporation of the chosen liquid leads to expansion and

likely rupture of the cell. Even approaching the upper limit can be dangerous. Highly viscous long carbon chain liquids such as octylamine may not effectively flow through the small tubing system of the liquid cell or into the viewing window, inhibiting replication of benchtop conditions.

Finally, the high degree of interaction between the liquid and the electron beam can result in radiolysis products that change the environment of the liquid, especially when there is an insufficient flow rate. Water in particular is susceptible to breakdown by the electron beam, yielding nanobubbles, hydrated electrons and protons, hydroxyl radicals, hydrogen radicals, and hydrogen peroxide.[109–112] These then interact with the sample in undesirable ways to yield side products in the viewing window (or in the case of sewage treatment, desirable ways).[113] Because electron microscopy tends to have a small field of view, especially when attempting atom resolution work, the observed phenomenon in the liquid cell may be a local result. Thus, a comparison with regions that were not irradiated by the electron beam, possibly post-reaction, should be recommended.

5.2 Cu Nanostructure Synthesis Controlled by Solution Viscosity

5.2.1 Background

Nanoparticle synthesis and growth is of interest due to the properties that arise at the nanoscale to be used as catalysts and coatings. [114–117] In particular, controlled size and shape wet synthesis provide economic benefits such as lower temperature processing, scalability, and a lower cost barrier toward manufacturing compared to high vacuum synthesis methods.[118,119] There are many studies into the solution chemistry reporting on the effect of reducing agent and surfactant choice on the size, morphology, and uniformity of the resulting nanoparticles. [120–123] Further

control of the nanoparticle formation can be achieved through real-time monitoring of the reaction at the solid-liquid interface of in situ techniques. The role of reducing agent on conventional synthesis and dissolution was investigated by in situ TEM where the electron beam formed hydrated electrons and hydrogen atoms to act as strong reducing agents in solution. [124] However, the impact of solution viscosity on the growth mechanism was not yet established. To that end, electron microscopy can assist with such an investigation.

5.2.2 Characterization of Nanoparticle Growth

In this work, the impact of solution viscosity onto photocatalytic reduction and deposition of copper onto TiO_2 nanoparticles was investigated. 10-15 nm TiO_2 nanoparticles were synthesized on graphite via physical vapor deposition. [125,126] $CuCl_2$ (3 mM) was dissolved in water, methanol, or a 50/50 mixture of water and methanol. The pH of the solutions was adjusted to either 7 or 3 by hydrochloric acid. The TiO_2/graphite was immersed in the aqueous $CuCl_2$ solution for 6 hours while illuminated with a mercury lamp (2.1 mW/cm^2 or 2.8 mW/cm^2) in the 400 nm wavelength region. The viscosities of water, methanol, and the 50/50 mixture are 0.89 mPa*s, 0.59 mPa*s, and 1.33 mPa*s, respectively.[127] TEM imaging was acquired at 200 kV on JEOL 2100F and STEM imaging was acquired at 300 kV on GrandARM. XPS (Kratos Axis Supra, Al K_α 1486.6 eV photon energy) with 0.5 eV energy resolution was used to quantify the relative amount of copper deposited on the TiO_2.

Various sizes of copper species were deposited onto the TiO_2 at the two illumination intensities for the different solutions, summarized in Table 5.1. After illumination with 2.1 mW/cm^2 in water, XPS was used to measure the amount of copper deposited, normalized to Ti 2p. The ratio of copper

to TiO_2 was compared for the four different synthesis conditions. As expected, an increase in illumination resulted in an increase of 1.5 orders of magnitude in total copper deposition, N_1 vs. N_2. Similarly, an increase of 2 orders of magnitude was observed when using a solution with lower viscosity, N^M_1 vs. N_1. Methanol is known to act as a sacrificial agent for hole scavenging which allows an increase in photocatalyzed reactions and thus an increase in copper deposition.[128] Unexpectedly, a comparison of N^M_1 and N^M_2 showed a decrease of total copper deposition despite an increased illumination. These values indicate a more complex growth mechanism beyond classical growth theory.

Table 5.1. Summary of Cu photodeposition

	Water		Methanol	
Illumination (mW/cm^2)	2.1	2.8	2.1	2.8
Label	N_1	N_2	N^M_1	N^M_2
Cu quantification (normalized to N_1)	1	50	100	1
Copper morphology	Nanoparticle	Nanoparticle	Nanoparticle	Flake
Copper size (nm)	1-2	2-3	1-2	20-25

TEM and STEM imaging revealed the morphology of the copper that was deposited on the TiO_2. Small nanoparticles were observed for the aqueous solution as well as low illumination intensity (N_1, N_2, and N^M_1). In contrast, photoreduction at a high rate in a low viscosity solution (N^M_2) resulted in flakes of copper oxide 20-25 nm in length separated by tens of nanometers from adjacent flakes (Figure 5.1) Low magnification EDS confirm the presence of the TiO_2 and Cu

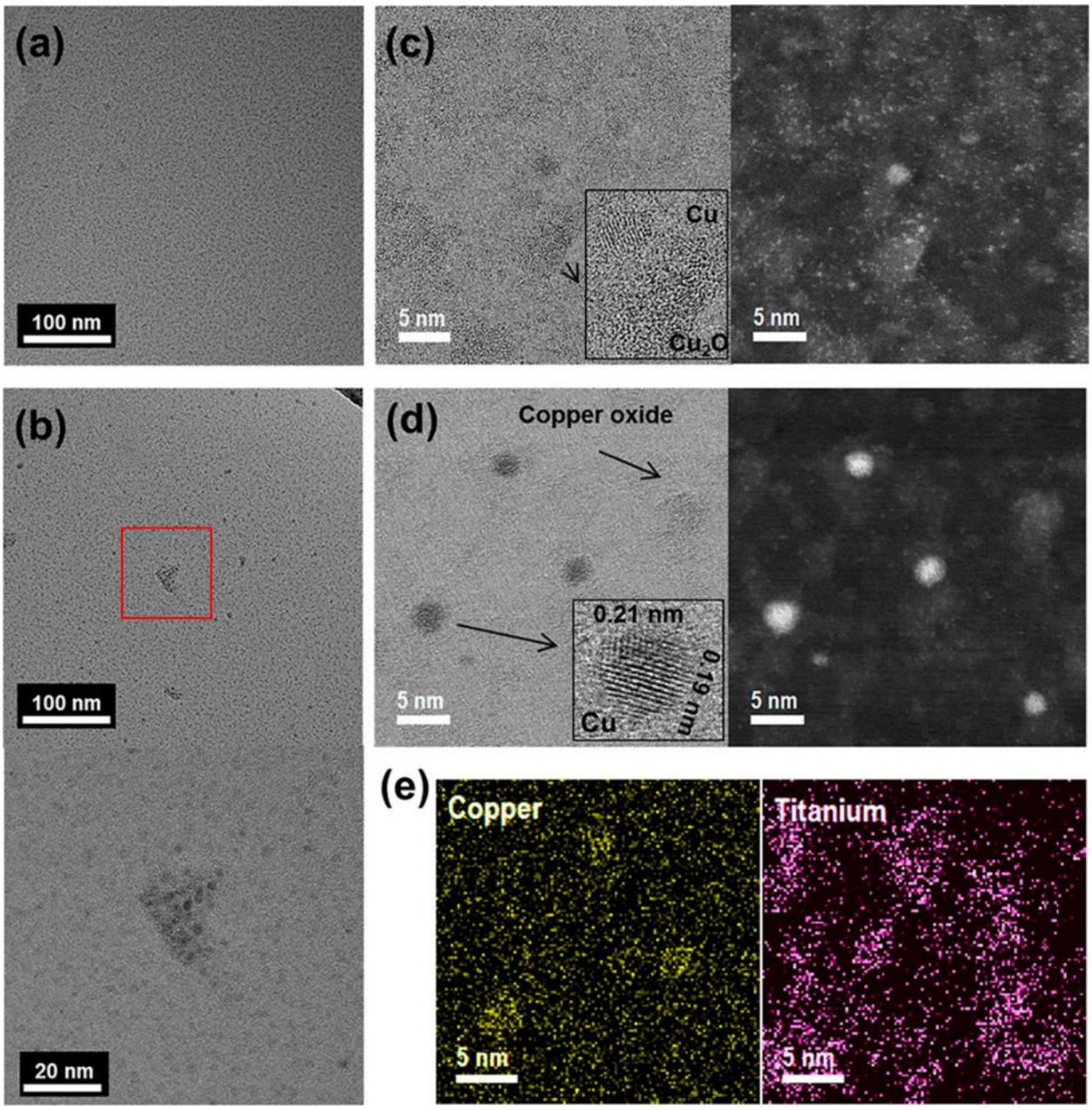

Figure 5.1. Cu photoreduced in water and methanol
Copper nanostructures synthesized at a high photoreduction rate. Low magnification TEM images of the nanostructures synthesized in (a) water (N_2)and (b) methanol (N^M_2). The bottom image in (b) corresponds to a higher magnification of the red box. Bright field STEM and HAADF images of the nanostructures prepared in (c) water and (d) methanol. Insets, magnification of the visible copper species. (e) EDS elemental map of (d). Reproduced with permission. Copyright American Chemical Society 2020.

nanoparticles (Figure 5.2) Attempts to image the flakes in STEM resulted in visible beam induced reduction of the flakes to nanoparticles over the course of a minute (Figure 5.3). The TEM images and EDS results confirm the presence of copper and the difference between copper species observed via XPS.

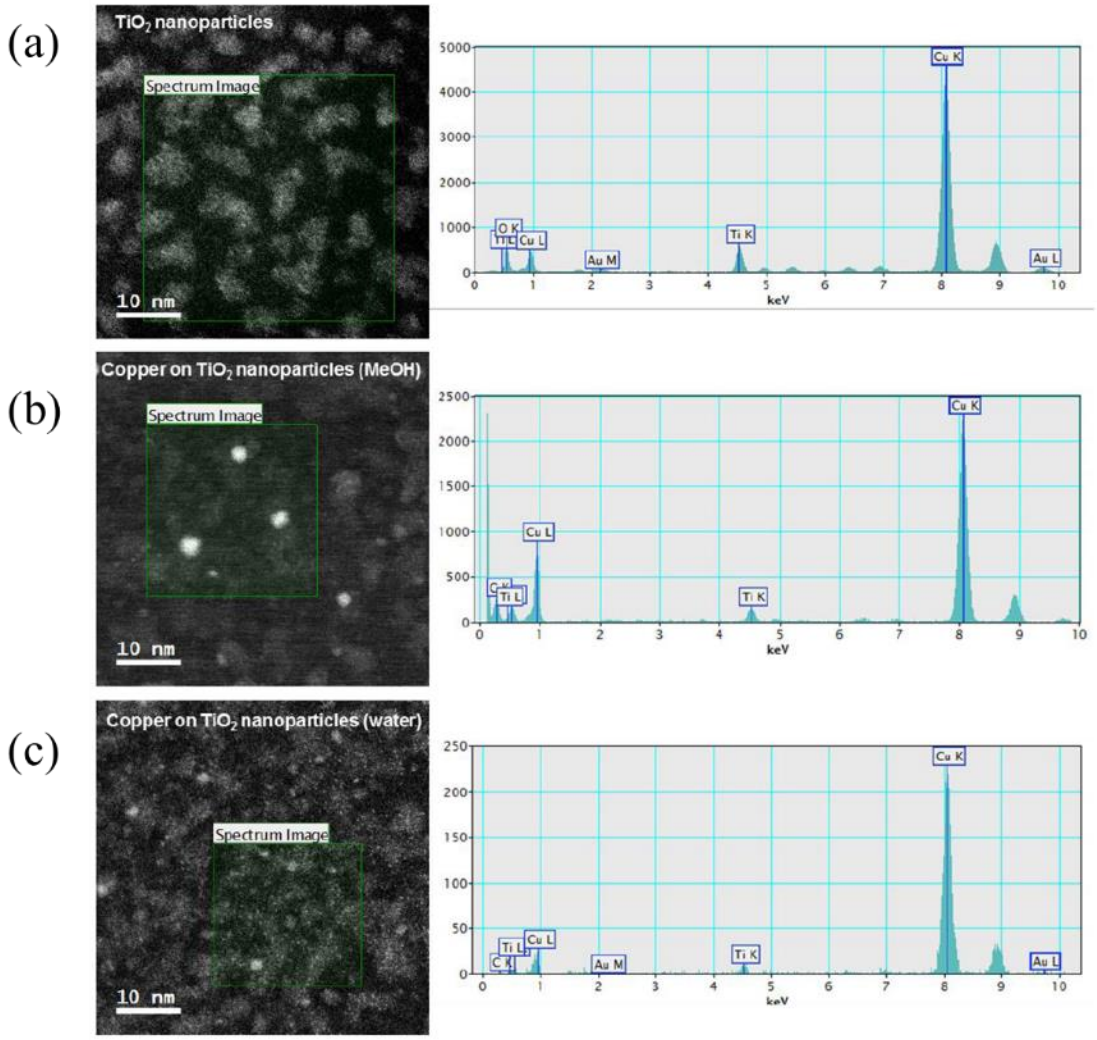

Figure 5.2 Low magnification STEM images and EDS of photoreduced Cu on TiO_2
HAADF and corresponding EDS spectra of the (a) pristine TiO_2/graphite before photoreduction of Cu and after photoreduction in (b) methanol and (c) water at a high photoreduction rate. Additional Cu and Au signal from the holder. Reproduced with permission. Copyright American Chemical Society 2020.

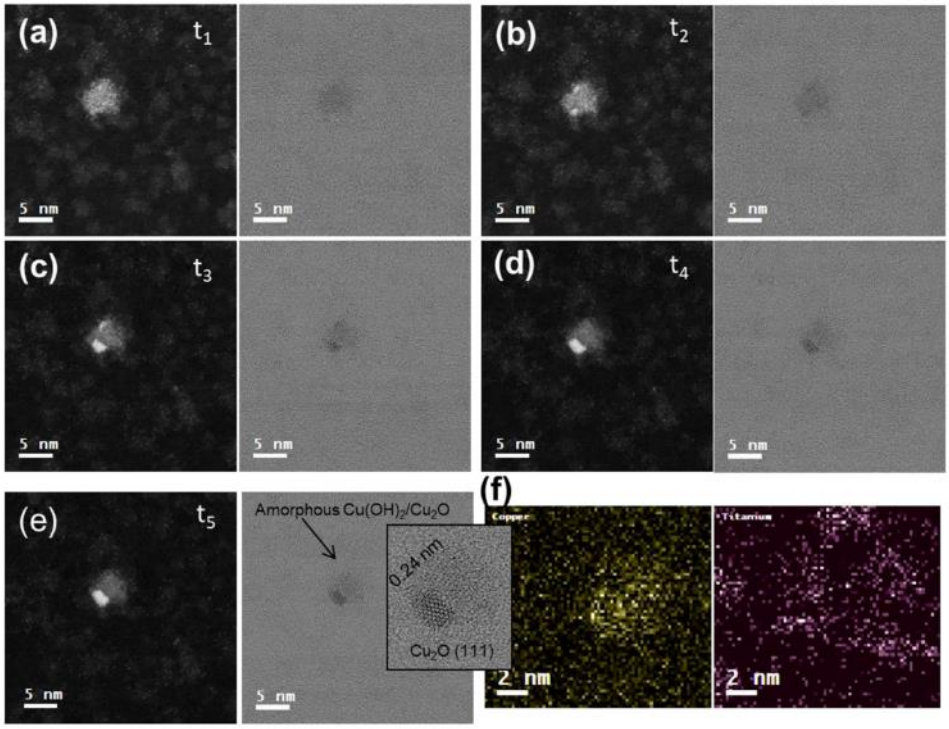

Figure 5.3 Time series of beam induced copper flake reduction
(a-e) Sequential high magnification HAADF (left) and BF (right) images of a copper oxide flake recorded ca. 20 s apart showing the reduction of the flake under prolonged exposure to the electron beam and the instability of the copper oxide species found in the flake. Inset, high magnification of the reduced copper species matching Cu_2O (111) lattice spacing. (f) EDS elemental mapping of the inset in (e). Reproduced with permission. Copyright American Chemical Society 2020.

5.2.3 Discussion and Conclusion

From the gathered XPS and TEM data, we conclude that photoreduction rate and viscosity play a role in the growth mechanism of the copper nanoparticles on TiO_2/graphite as summarized in Figure 5.4. At a low photoreduction rate (N_1 and N^M_1), the growth mechanism follows the classical growth theory irrespective of solution viscosity. The lesser amount of copper deposited on the surface travel as adatoms along the surface, limited by diffusion control. Conversely, at a high photoreduction rate (N_2 and N^M_2), classical growth theory does not explain the observed difference between the two solutions. Nonclassical growth theory that included particle-mediated and

diffusion-limited growth can be used to explain unusual morphologies at solid-liquid interfaces. The theory states that the growth of nanostructures proceeds by attachment of particles. An example would be the oriented attachment emphasized by Alivisatos and supported more recently. [129–131] The influence of viscosity toward nanoparticle growth has been discussed in terms of Brownian motion.[132] In the case of high photoreduction, the initial stage is similar to that of low photoreduction wherein clusters form. As further copper was deposited, the rate of cluster attachment must compete with desorption of copper species from the surface. In a high viscosity solution such as water, the attachment of individual atoms dominates while in a low viscosity solution such as methanol, in-plane diffusion of clusters leading to in-plane attachment dominates. Similar results have been seen with in situ TEM where the electron beam acts as the reduction source. [124,133]

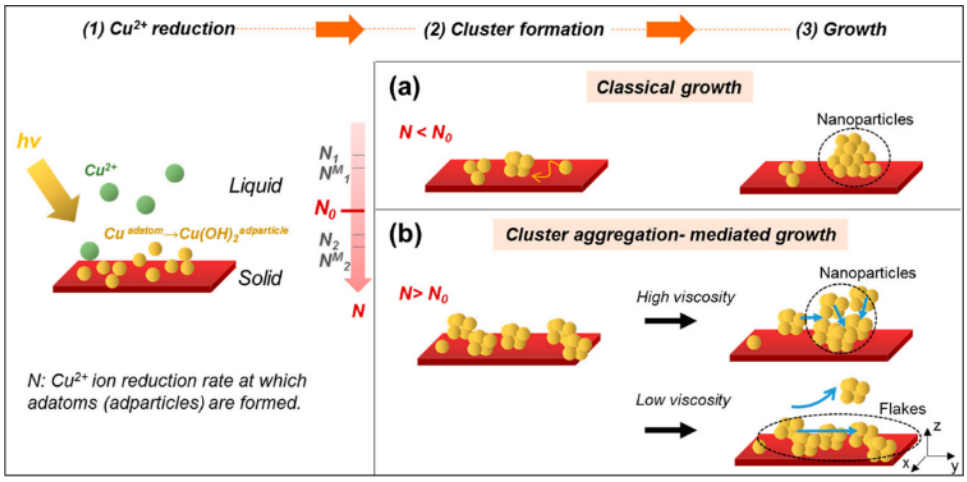

Figure 5.4. Schematic of Cu growth at solid-liquid interface
A schematic of the mechanism for the growth of the Cu nanostructures after photoreduction. (a) When the photoreduction rate, N, is below a threshold, N_o, the nanostructures follow classical growth. (b) When $N>N_o$, non-classical growth theory comes into play and viscosity influences the final structure. Reproduced with permission. Copyright American Chemical Society 2020.

Understanding the dynamics of nanostructure formation at the solid-liquid interface remains important for the growth of unique nanomaterials. The investigation into the impact of solution

viscosity may be applicable to other photoreduction synthesis of copper onto a solid support surface. As observed, nanomaterial growth may not follow expected classical pathways and further investigations into the cause will enable control of growth conditions. While this work did not observe the growth in situ due to time constraints, the benchtop conditions may be replicated inside the microscope by substituting the photo-illumination with the electron beam.

5.3 Bulk and Interfacial Nanobubble Formation

5.3.1 Background

The formation of nanobubbles are related to various physical and chemical phenomena such as decompression sickness, electrochemical generation of bubbles, and solar steam nanobubbles.[134–136] The adherence of nanobubbles on an electrode surface may hinder the diffusion, convection, and migration of interfacial ions, reducing electrocatalytic efficiency.[137] Due to properties such as long-time stability and high surface-to-volume ratio, nanobubbles have been applied to technologies in the biological, medical, and nanotechnological fields.[138–145] Generally, nanobubbles can be divided into two types, interfacial nanobubbles (INBs) and bulk nanobubbles (BNBs). INBs are adsorbed on a solid-liquid interface while BNBs are located within the bulk of the solution. Due to their location, INBs are immobile and exhibit a high curvature while BNBs are mobile.[146] Due to their different characteristics, these nanobubbles are used in different applications.[147–151] Engineering stable nanobubbles is a requirement for the various applications; the conversion between INBs and BNBs are also a topic of consideration. An improved understanding of the nucleation and growth kinetics for nanobubbles lend to finer engineering control. While some studies have been done on nanobubble kinetics, the small size of

nanobubbles has been a challenge to the kinetic studies.[152–154] As noted, a byproduct of the radiolysis of water is the generation of nanobubbles from H_2 molecules.[155] Therefore, in situ liquid cell TEM has garnered interest as a means to study nanobubbles in solution. So far, there has been research on the critical size stability, collapse, and interactions between nanobubbles.[154,156,157] However, these studies lack research into the growth kinetics which is critical to design nanobubbles of appropriate sizes for different applications.

5.3.2 In Situ TEM Nanobubble Formation

The Protochips Poseidon liquid cell was assembled with 500 nm spacers to facilitate liquid flow (Figure 5.5a). The images were acquired on a JEOL 2800 at 200 kV with the observation focused on the bottom chip with a constant dose of ca. 400 $e^-/Å^2$. Throughout, the brightness of the TEM images dropped over time which has been mentioned in other works.[158] Initially, the space between the silicon nitride windows was filled with deionized water, but as nanobubbles formed, the silicon nitride windows bulged outward, increasing the thickness of the viewing region and decreasing the spatial resolution over the course of the observation. For regions where there was water, the contrast decreased over time. For regions with bubbles, the contrast increased over time as the liquid in the path of the electron beam was replaced by gas. The Fresnel fringe method can be used to distinguish the relative vertical position of nanobubbles away from the focus (Figure 5.5b).[159]

To aid discussion of results, the observations were separated into two timeframes, stage one and two. In the initial stage, only nanobubbles on the solid-liquid interface of the bottom E-chip formed. Nanobubble A nucleated on the E-chip surface and grew up to 300 s without the

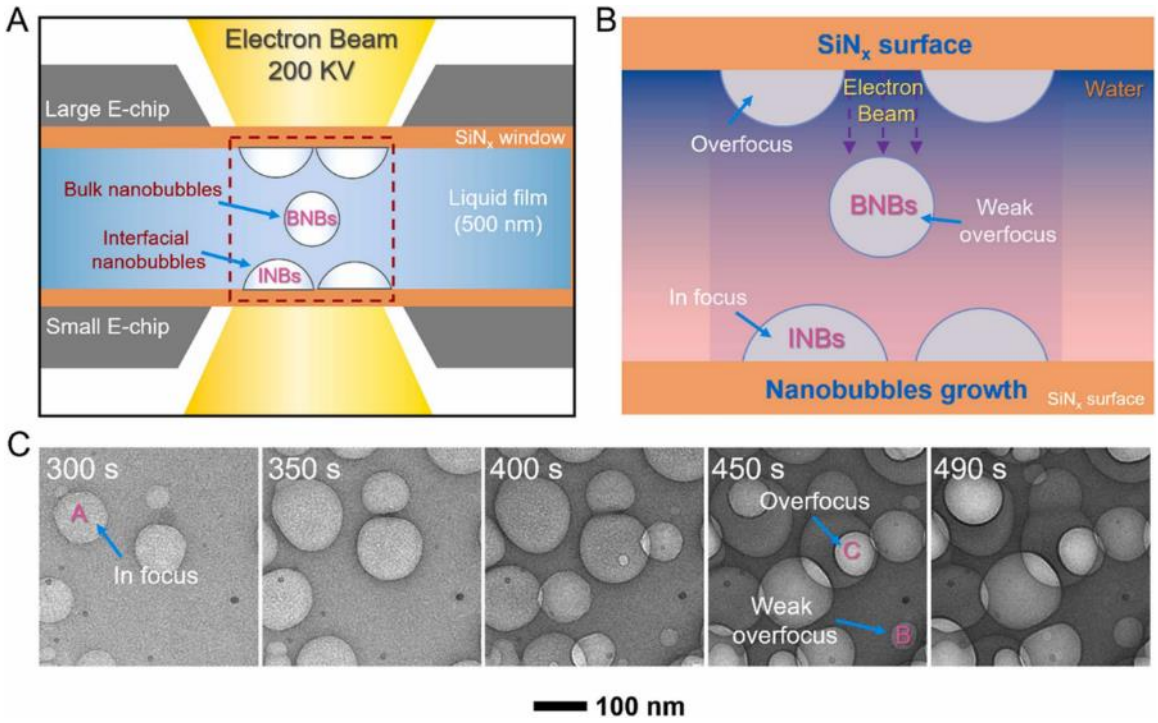

Figure 5.5. TEM setup and observations of nanobubble formation
(a) Schematic of the Poseidon liquid cell with the two types of nanobubbles. (b) Schematic of the relative locations of the nanobubbles by use of Fresnel fringes. (c) Select frames of the in situ TEM observations with specific nanobubbles labelled for analysis. Reproduced with permission. Copyright Elsevier 2023.

appearance of Fresnel fringes (Figure 5.5c). Heterogeneous nucleation occurred more frequently than homogeneous nucleation at the solid-liquid interface. Between 400-490 s, nanobubble B grew and exhibited a dark fringe, indicating a weak overfocus. Other nanobubbles, including nanobubble C grew with a dark fringe and a larger line width, indicating a difference in vertical positioning away from the E-chip surface.

5.3.3 Discussion and Conclusion

An analysis of the growth kinetics was performed on the nanobubbles. Figure 5.6 shows a time series of the growth trajectory of several nanobubbles. While the nanobubbles nucleated during

both periods with different stable sizes, the growth trajectories were similar. Initially, nanobubbles grow at an increasing growth rate before reaching a maximum and reversing course. The change of the slope of the growth rate from a positive to negative value indicated a change in the driving force behind the growth. The driving force of nanobubble growth comes from two attributes: the pressure difference from inside and outside the nanobubble, resulting in a fast growth rate; the diffusion of solvated gas molecules from water into the nanobubble, resulting in a slow growth rate. In the first stage, the pressure difference dominates as the main driving force. Once a specific size was reached, the diffusion of gas molecules dominated and the growth rate fell.

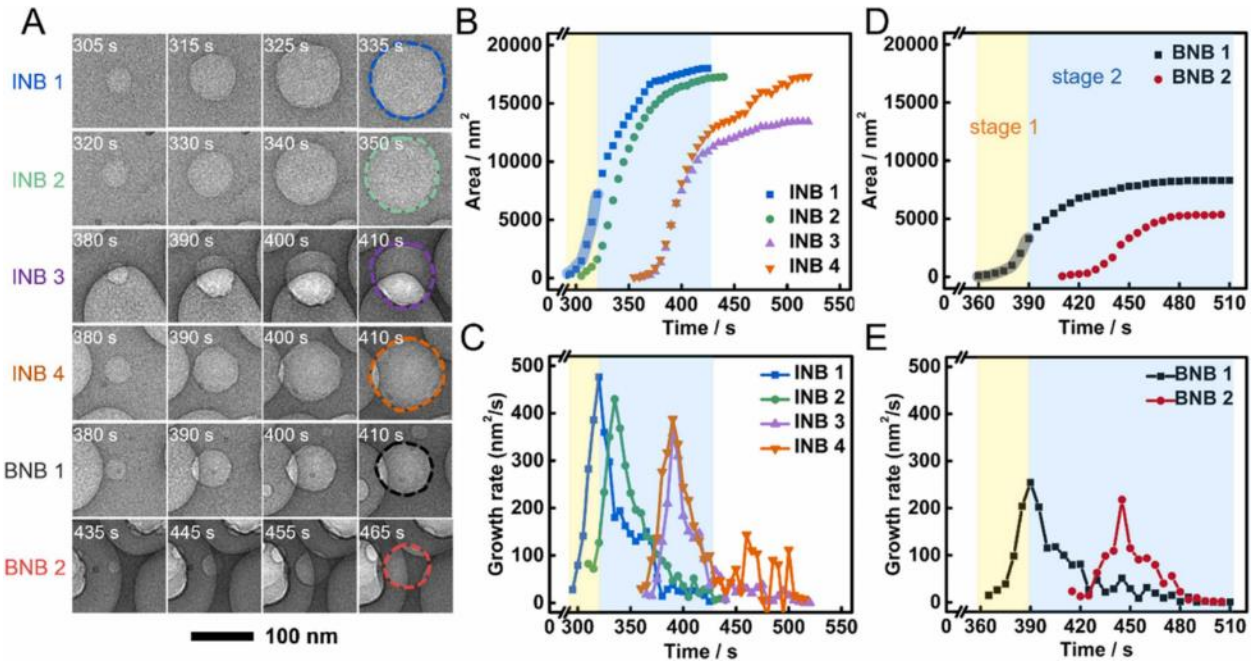

Figure 5.6 Analysis of nanobubble growth trajectories
(a) Time series of showing the growth of both types of nanobubbles. Plot of measured projected area of (b) interfacial and (d) bulk nanobubbles over time with the stages indicated. Corresponding growth rates of (c) interfacial and (e) bulk nanobubble areas. Reproduced with permission. Copyright Elsevier 2023.

In addition to observations of the growth kinetics of INBs and BNBs, the conversion of a BNB to a INB was observed in situ. Nanobubble P grew with a dark fringe, indicating that the nanobubble was located above the bottom E-chip and did not form at the solid-liquid interface (Figure 5.7). Nanobubble P grew constantly before 457 s. At 458 s, the brightness of nanobubble P changed suddenly and then stabilized. A plot of the area versus time showed a sudden change in growth rate at the same timeframe. The corresponding plot of growth rate versus time matches the observation where there was a sudden shift. Nanobubbles A and B did not have a similar change to the brightness upon changing from stage one to two, indicating that the change in growth rate was caused by a different behavior. Similarly, nanobubble C did not show a change in brightness either. Instead, nanobubble P showed a high growth rate as the time approached 458 s that was not seen with BNBs. We conclude that this was due to the compression of the bubble shape caused by interactions with the upper E-chip surface, leading to the nanobubble spreading in the horizontal direction in the moments before touching the solid surface. Then the nanobubble proceeded as an INB in stage two growth.

Nanobubble formation and growth, induced by an electron beam, were imaged in situ using a liquid cell. The quasi-equilibrium growth trajectories of the nanobubbles showed two stages with different driving forces. INBs and BNBs were distinguished using the Fresnel fringe method aided with analysis of the growth kinetics. Observations of the nanobubbles captured the conversion from BNB to INB, confirmed by a sudden change to the image contrast along with unexpected non-equilibrium growth rates. The insights of growth kinetics of nanobubbles shown here at the nanoscale improve tailored engineering of nanobubbles for suitable growth toward different applications.

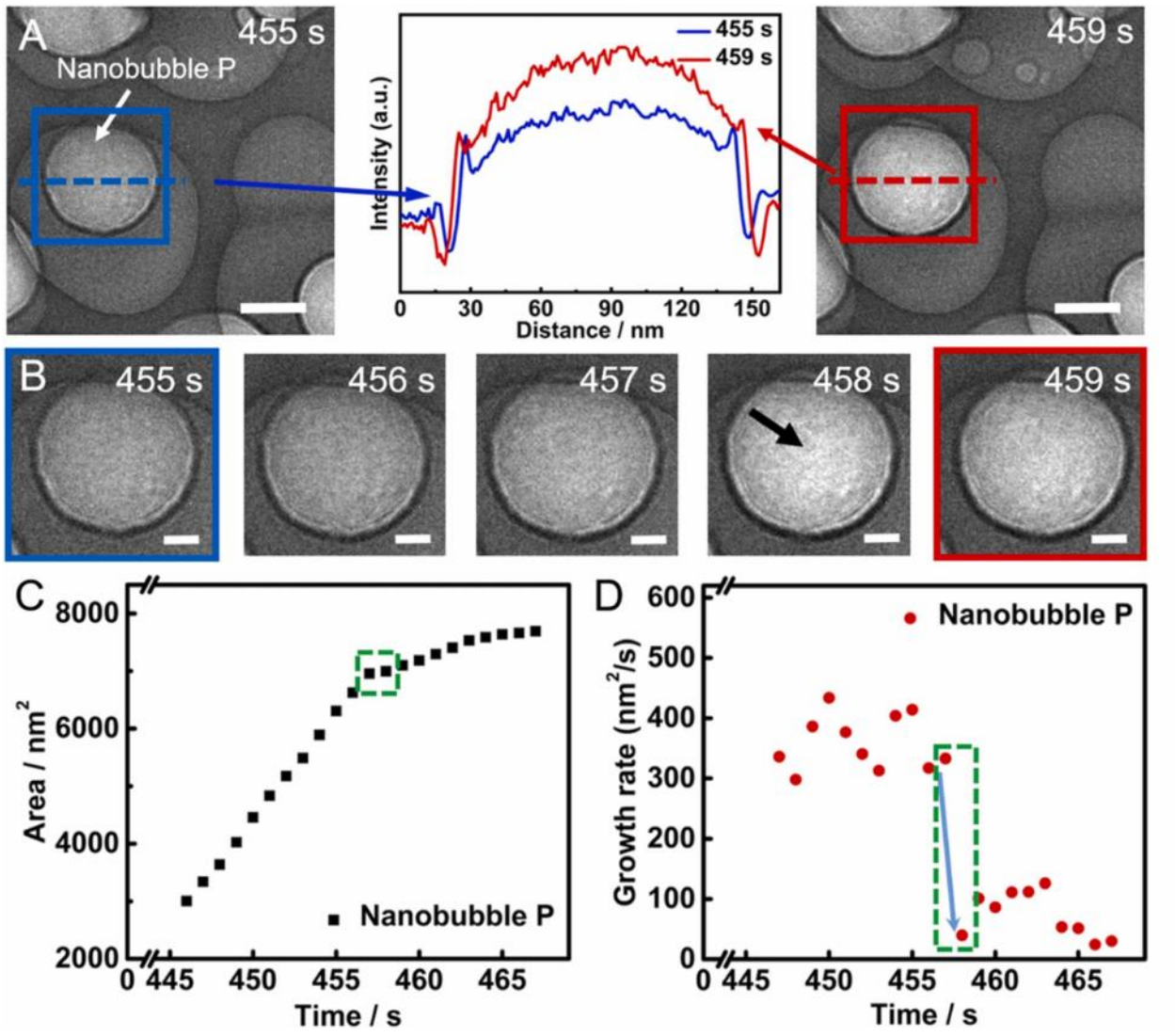

Figure 5.7 Analysis of conversion from bulk to interfacial nanobubble
(a) TEM images of nanobubble P at two different times and the corresponding brightness profile. Scalebar, 50 nm. (b) Time series of nanobubble P showing the change in brightness of the central region (black arrow). Scalebar, 20 nm. (c) Projected area versus time of nanobubble P. (d) Corresponding growth rate of nanobubble P. The green rectangle is the point when the nanobubble touches the surface of the top E-chip. Reproduced with permission. Copyright Elsevier 2023.

5.4 Pt@Pd Octahedral Nanoparticle Dissolution upon Biasing

5.4.1 Background

Corrosion of electrocatalysts during electrocatalytic processes results in degradation of activity and loss of stability. Nowadays, nanoparticles are widely used as electrocatalysts, either by themselves or embedded onto an electrode surface. Recently, M-Pt (M=Pd, Au, Co, etc.) core-shell nanoparticles have proven a promising system that yields high activity, improved stability, and efficient utilization of platinum compared to pure platinum nanoparticles.[160–169] Still, the degradation of these nanoparticles arising from loss of shape and elemental distribution remains an obstacle for widespread commercialization, especially for platinum-based nanoparticles. The structure changes during operation lead to deterioration of performance due to acidic corrosion. Density functional theory calculations have suggested that dissolution potentials decrease with increasing strain as well, another factor leading to loss of electrocatalytic activity.[10,170] To that end, in situ liquid cell experiments are well positioned to provide mechanistic insights into the dissolution and degradation processes that nanoparticles encounter. Application of a potential within the microscope with a three electrode setup mimics the benchtop setup well, allowing researchers to observe processes unfold.

5.4.2 Characterization of the Pt@Pd Octahedron

Pristine Pt@Pd octahedral nanoparticles (20 nm) were imaged on GrandARM, showing the core-shell nature of the nanoparticle along with the elemental distribution (Figure 5.8) Pt@Pd octahedral nanoparticles were imaged after various cycles of accelerated durability testing (ADT, 0.6-1.0 V vs. a rotating disk electrode, 100 mV/s) which showed an eventual loss of the Pd core, leaving a Pt cage (Figure 5.9). The (111) facet of the pristine nanoparticle was formed from two layers of Pt while after 30,000 cycles, a change in the thickness of the Pt was seen. By 50,000

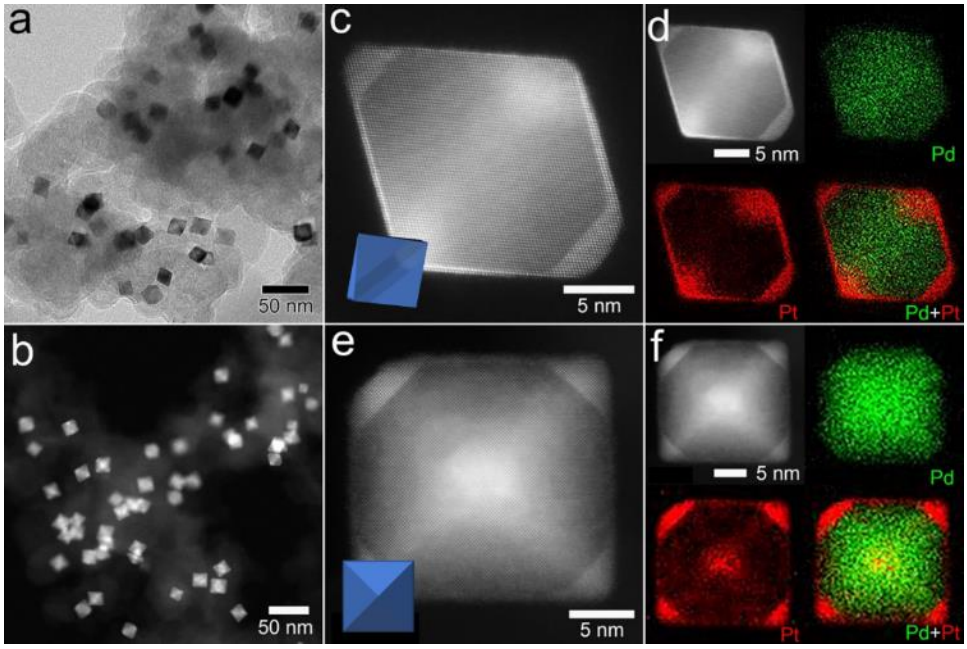

Figure 5.8. STEM images and EDS of pristine Pt@Pd octahedral nanoparticles
Low magnification (a) BF and (b) HAADF images of the pristine Pt@Pd octahedral nanoparticles showing the homogeneity of the starting material. High magnification HAADF images along the (c) (110) and (d) (100) direction. Octahedron model in bottom left. (d and f) EDS elemental maps of Pd and Pt of the nanoparticle in (c) and (e).

cycles, the loss of the faces of the octahedron and increased thickness of the edges to 8 layers indicated Pt had migrated from the face to the edges.

EDS mapping confirm the loss of Pd from the nanoparticle rather than intermixing to form an alloy with the Pt (Figure 5.9). Careful observation of the nanoparticles show a slight intensity drop on a projection of one of the (111) facets. A line profile of the EDS signal along the projection gives a hint at the sequential process for the dissolution of the Pd (Figure 5.10). Initially, the thickness of the Pt is uniform across the facet. After 10,000 cycles, a faint intensity loss was seen at high magnification which corresponded with a decrease in Pt signal. Such a defect formation may be due to Pt migration or leaching into solution, but confirmation of the mechanism is not possible from imaging the ADT samples. Bromide causes preferential deposition of Pt from facets onto

corners during formation of a shell.[171] Upon exposure of the interior, galvanic and halogen-induced etching of Pd is known to occur.[172] After 30,000 cycles, the movement of Pd to the Pt defect was evident in the EDS where there was equivalent Pd signal to Pt signal at the location of the defect. This indicates that the Pd was leaching out into solution. The sample after 50,000 cycles showed the complete loss of Pd and eventual thickening of the Pt octahedral cage. Low magnification EDS elemental maps show the presence of the leached Pd spread about on the carbon membrane of the TEM grid. To investigate the initial defect formation and movement of Pt, in situ electron microscopy inside a liquid cell was performed to replicate the benchtop electrochemical cycling.

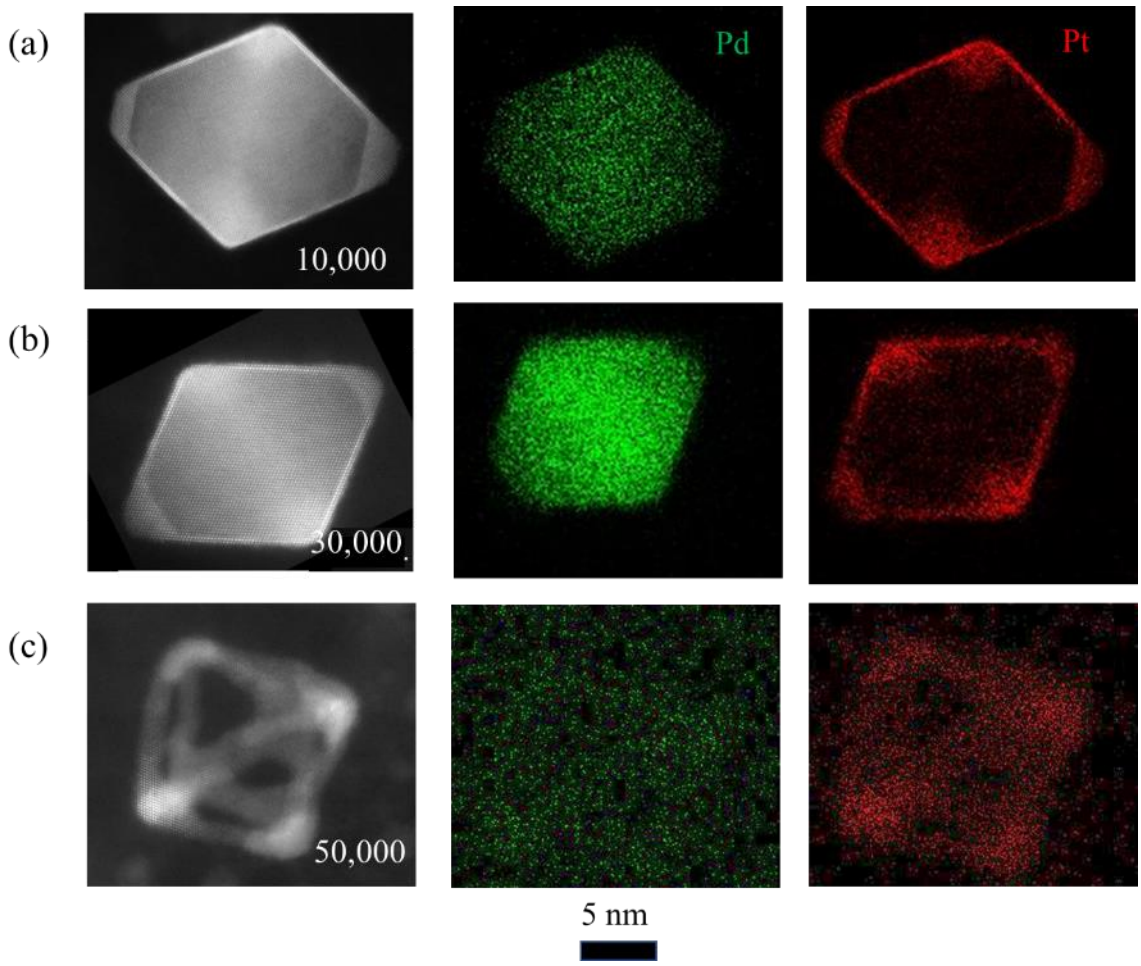

Figure 5.9. HAADF image and EDS of Pt@Pd after various ADT cycles
HAADF images and EDS elemental map for Pt@Pd octahedral nanoparticle after (a) 10k, (b) 30k, and (c) 50k cycles of accelerated durability testing.

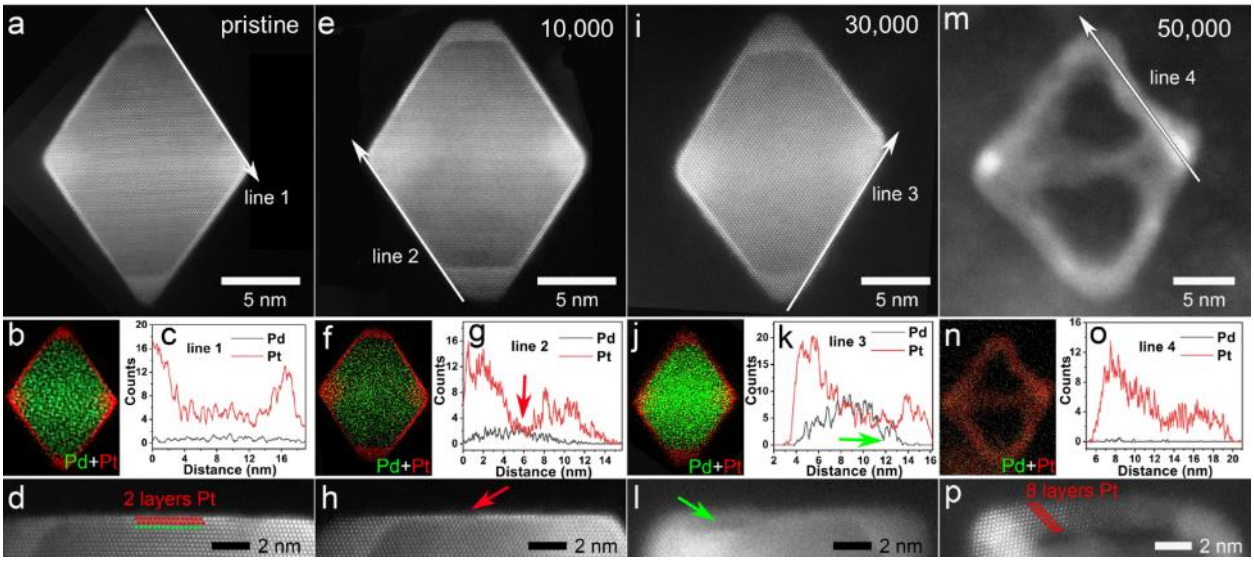

Figure 5.10. Comparison of Pt@Pd elemental distribution after various ADT cycles
HAADF images, EDS elemental maps, line scan, and high magnification HAADF images of the facet projection for Pt@Pd core-shell octahedrons (a-d) before and after (e-h) 10k, (i-l) 30k, and (m-p) 50k cycles ADT, respectively. Red arrow in (g, h) points to an intensity loss corresponding to a defect in the Pt shell. Green arrow in (k, l) points to region where Pd is leaching out from the interior.

5.4.3 In Situ Imaging of the Pt@Pd Octahedron

To match the ADT conditions, 0.1 M $HClO_4$ was used with both cycling between 0.6-1.0 V and 0.6 V constantly applied. In situ TEM imaging was acquired on a JEOL 2800 and recorded on a Gatan OneView camera at 10 frames per second. We observed that a constant potential induced a more stable viewing condition and more rapid change to the nanoparticle morphology so constant potential was selected as the investigation method. A time series of a region of nanoparticles was observed for 10 minutes with 0.6V applied (Figure 5.11). Further examination of the captured frames showed the process through which the dissolution initially proceeded. A surface roughening was observed by 100 s with a little concavity seen (Figure 5.12). The concavity became obvious by 200 s and did not appear to increase further. Plotting the side-to-side and corner-to-corner distances versus time showed that there was a rapid change up to 250 s before stabilizing.

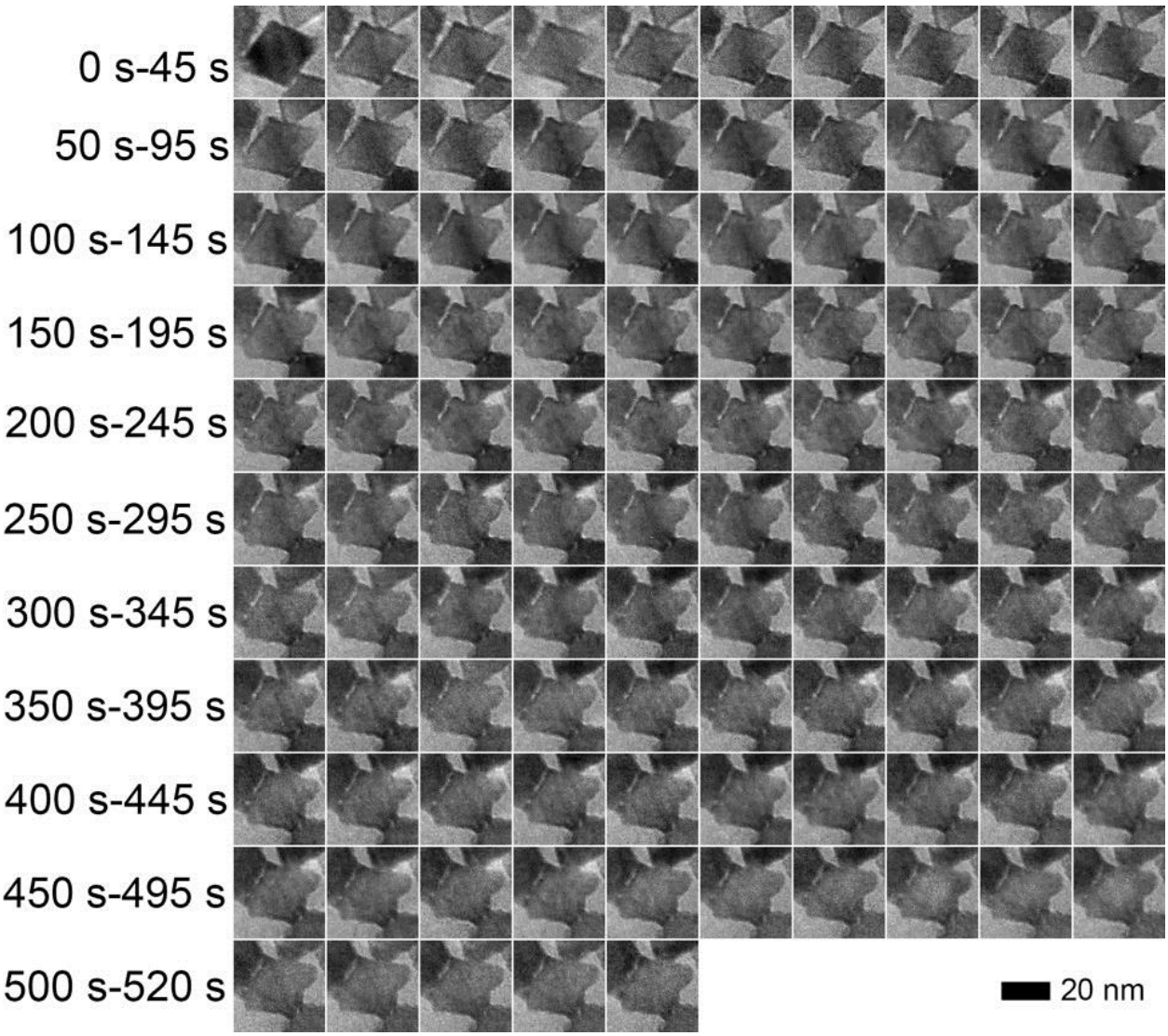

Figure 5.11. Time series of a Pt@Pd octahedron in situ under constant potential
A time series from 0-520 s of the same Pt@Pd octahedron under constant 0.6 V bias. Frames from every 5 s shown.

The TEM imaging seem to show that the initial defect forms rapidly, resulting in an imperfect Pt shell. The reduction potential of Pd is less than Pt (0.92 V and 1.19 V vs. standard hydrogen electrode, respectively) so Pd will dissolve first when exposed to the aqueous environment.[173] The Pd dissolution proceeds and then Pt migration to the edges and corners dominate once the majority of the Pd is gone from the core. Due to time constraints, the in situ electrochemical biasing

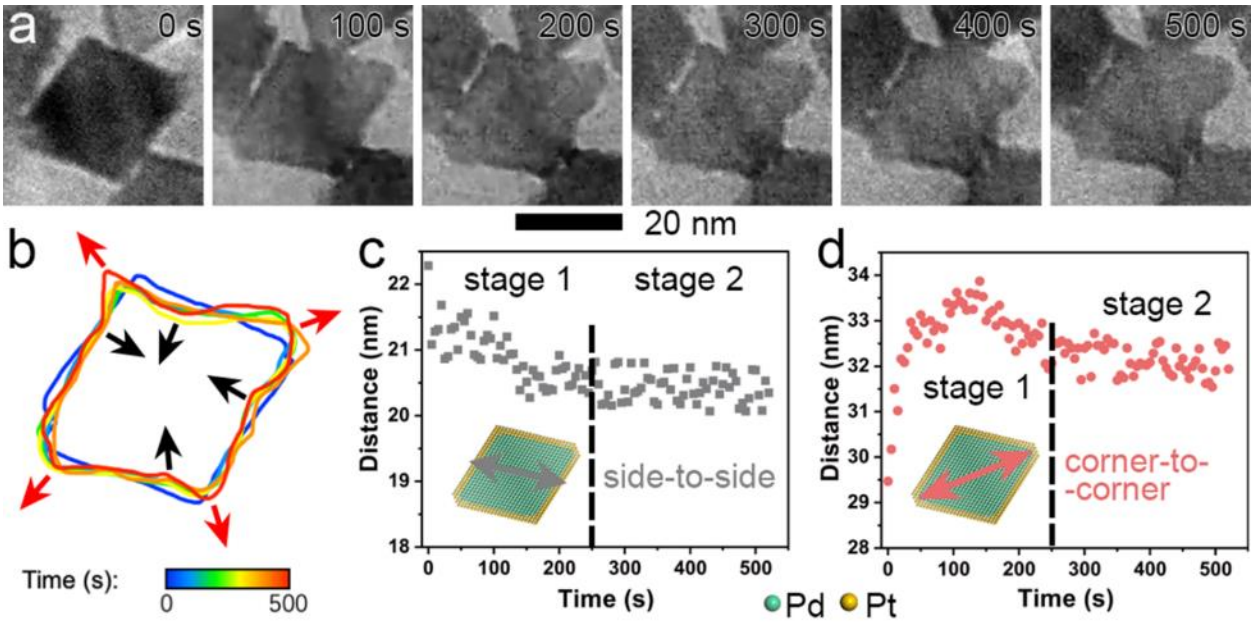

Figure 5.12. Analysis of in situ Pt@Pd octahedron structural changes
(a) Select frames from the in situ time series showing the shape and size. (b) Outlines of the nanoparticle from frames in (a). (c) Measured side-to-side distance over time. (d) measured corner-to-corner distance over time.

was not able to replicate the 50,000 ADT cycle which requires 4.6 days of continuous cycling. Thus, the final state where Pt nanocages were seen with the ADT samples were not observed in the in situ experiments.

After the in situ experiments were performed with the liquid cell, the E-chips were examined to determine the fate of the Pd that was observed to dissolve out of the core. Low magnification HAADF imaging showed the presence of a lighter intensity material outside of the nanoparticles (Figure 5.13a). Low magnification EDS indicate that there was a loss of Pd and Pt from the Pt@Pd octahedral nanoparticles into solution which was not seen with the ADT samples (Figure 5.13b, c). High magnification HAADF images show the clear presence of amorphous blobs adjacent to the nanoparticles (5.13d). EDS elemental mapping indicate the amorphous blobs are Pt which matches the expectation that the initial step for nanocage formation is the Pt defect formation on

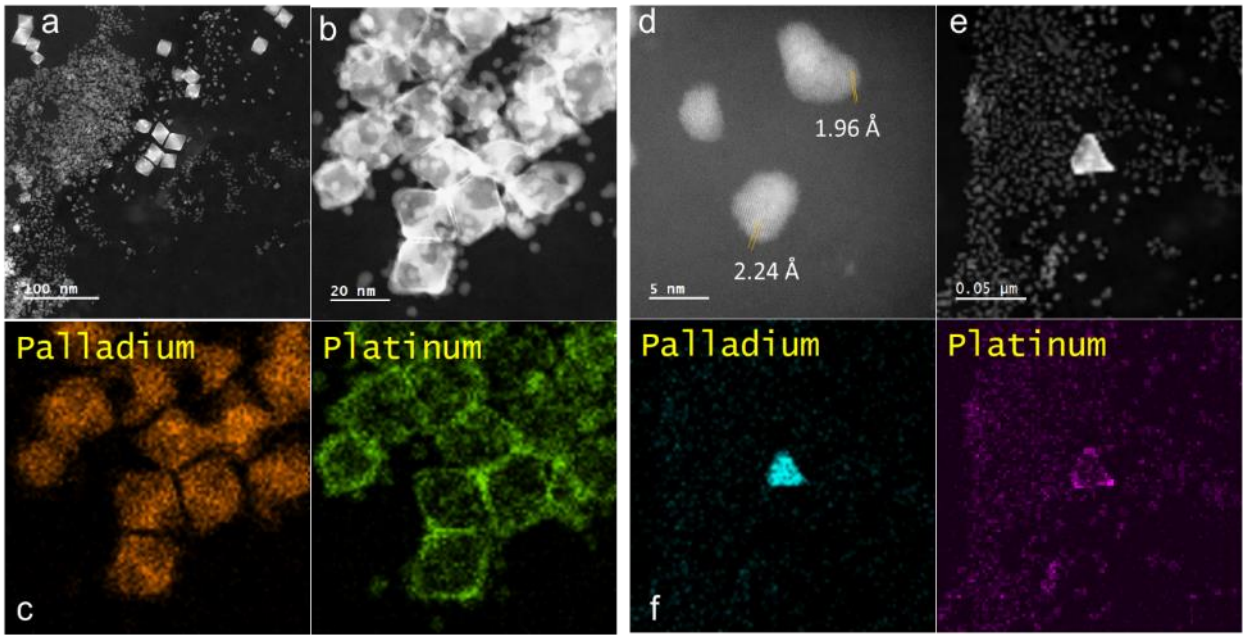

Figure 5.13. Analysis of Pt@Pd octahedron post-in situ
HAADF images of Pt@Pd octahedrons observed post-in situ at (a) low and (b) high magnification. (c) EDS elemental mapping of (b) showing the migration of Pt. (d) High magnification HAADF image of the lighter intensity nanostructures seen at low magnification. (e) Low magnification HAADF image of the non-octahedron particles. (f) EDS elemental mapping of (e) showing the mixture of Pd and Pt loss from the octahedrons.

the shell and migration of the Pt to expose the underlying Pd (Figure 5.13e). In another region, high magnification HAADF imaging of nanoparticles formed from the lighter Z contrast material show lattice spacings of 2.24 Å and 1.96 Å (Figure 5.13f). Due to the similar size of Pt and Pd, 2.24 Å may be attributed to the (111) lattice of either Pt or Pd nanoparticles. Similarly, 1.96 Å may be associated with the (200) lattice of either transition metal nanoparticles.[174–177] Together, the post-in situ analysis show the extent of defect formation and leaching which was seen in stages with the ADT samples.

5.5 Conclusion

Liquid cell inside the electron microscope is a powerful tool to observe processes in situ. This is of particular relevance as many benchtop reactions occur in a liquid environment so replication within the microscope allows researchers to probe processes in new ways to gain insight for applications such as nanoparticle synthesis and degradation. Even what may be undesirable byproducts of radiolysis may be turned into a desirable outcome as new applications are uncovered. One of the main limitations, the loss of spatial resolution, is an ongoing direction for research as graphene membranes are being explored as an alternative to silicon nitride. As more nanomaterials are probed through in situ liquid cell electron microscopy, the view into the nanoscale world broadens further.

In Chapter 5.2, Dr. Djawhar Ferrah provided the samples and acquired the XPS data.

In Chapter 5.3, Dr. Fenglei Shi and Dr. Hao Hu performed the nanobubble size tracking.

In Chapter 5.4, Dr. Fenglei Shi provided the samples. Dr. Fenglei Shi and Dr. Jianbo Wu performed the in situ structural change analysis on the time series.

Chapter 6

Summary and Outlook

In summary, I have presented studies of the structural, chemical, and electronic evolution of different nanomaterials by leveraging aberration corrected S/TEM imaging and spectroscopy in situ and ex situ at atomic resolution and at low magnification. First, the preparation method to ensure acquisition of good quality TEM data for powder samples was discussed. The most common method, dropcasting, was detailed along with ways to handle powders that do not disperse easily. After introducing the basics of TEM and STEM imaging and some of their corresponding advantages, disadvantages, and limitations, the use of imaging in situ was discussed. Through the use of MEMS based in situ holders which can isolate the environmental conditions from the microscope vacuum, similar microscope parameters may be used for both in situ and ex situ samples. Next, the basis of EDS and EELS within the microscope was discussed with example results shown. Typical use cases for these complementary spectroscopic techniques was provided. A brief discussion of vibrational EELS, a relatively recent technique, was provided. In comparison to spectroscopic techniques inside the microscope, the basis of some macroscopic spectroscopic techniques commonly applied to nanomaterials was provided. The advantages and limitations of probe molecule FTIR, Raman, X-ray absorption spectroscopy, and X-ray photoelectron spectroscopy were provided. The key limitation of macroscopic spectroscopy is the lack of spatial information to the acquired spectra, instead providing sample-averaged data. The primary limitation of electron microscopy is the limited field of view due to the high magnification to reach

atomic scale. Using both microscopy and macroscopic techniques to investigate nanomaterials allows researchers to mitigate the disadvantage of each.

The first nanomaterial investigated using in situ and ex situ microscopy, corroborated with macroscopic techniques, was a Zr based MOF. Post-synthesis modifications of MOFs are a common method to adjust the characteristics and capabilities of a MOF. Changes to the pore size, addition of active sites and functional groups, and linker exchange all involve a structural or chemical change. The initial structure was characterized with TEM, STEM, and electron diffraction. The structural changes during in situ heating was monitored with TEM and analyzed through the FFT of the direct images, showing a contraction of the inter-metal center distances. Vibrational EELS was then used to understand the changes to the chemical bonds. Matching results from ex situ samples corroborated the in situ data. Combining all the information, the step-wise transformation was elucidated. The in situ TEM showed how the MOF structure changed as the chemical bonds changed, an important characteristic of MOFs that directly impact their activity.

The second nanomaterial investigated was Pt(x)/CeO_2 nanoparticles as the catalyst underwent H_2 reduction with CeO_2 nanoparticles used as a comparison. Many works have been done on the surface reduction process of CeO_2, but questions still remain about various steps such as the localization of the Ce^{3+}. By using coreloss EELS, the surface reduction of Ce was measured before and after H_2 reduction without exposure to air which could re-oxidize the material. Due to the thickness of the silicon nitride membranes and the desire to retain a high degree of spatial resolution, signal-to-noise for the EELS data was improved post-acquisition through principal component analysis. After data processing, the Ce M_5/M_4 peak height ratio was mapped and showed the location of Ce^{3+} aggregation. By combining the HAADF images with the Ce^{3+} maps, it was seen that the Ce^{3+} aggregated at the CeO_2-CeO_2 boundaries, regardless of the identity of the

Pt species. In comparison, Pt-free CeO_2 showed a more even distribution of Ce^{3+} across the surface. The EELS maps indicated a clear relevance of CeO_2-CeO_2 boundaries which was investigated through sequential reduction-oxidation-reduction with FTIR and EELS. The sequential experiment showed that the first reduction resulted in an irreversible change yet HAADF imaging, XRD, and surface area measurements indicated no changes to the structure of individual nanoparticles. No sintering was observed to occur but analysis of the FFTs of the CeO_2 and Pt/CeO_2 showed clear differences. Before reduction, the FFTs showed a circularity, indicating a random orientation of the various Pt/CeO_2 and CeO_2 nanoparticles. After reduction, CeO_2 retained the random orientation while Pt/CeO_2 showed a reduction in the randomness, indicating an alignment between nanoparticles. This alignment, termed oriented attachment, is the preceding step toward sintering, with a low activation energy barrier. Thus, we can see that the in situ Pt/CeO_2 surface reduction by H_2 is accompanied by oriented attachment which allows a stabilization of large quantities of Pt-enabled hydrogen dissociation and the resulting oxygen vacancies.

Finally, observations in the liquid cell were varied, monitoring nanobubbles and nanoparticles both. The growth trajectory of nanobubbles were directly observed in situ and plotted, showing two stages of growth for both interfacial and bulk nanobubbles. It was seen that the nanobubbles followed non-equilibrium growth trajectories, first increasing rapidly before suddenly dropping. It was also observed that interfacial nanobubbles have a higher growth rate when comparing the projected area of the nanobubble. The conversion from bulk to interfacial nanobubble was also observed, showing a sudden change of the growth rate different from the two stages previously observed for non-conversion. For nanoparticles, rather than growth, dissolution was monitored for Pt@Pd octahedrons. Accelerated durability testing was applied to Pt@Pd nanoparticles which showed that the Pt shell migrated from facets to corners and edges. Eventually, the Pd interior

leached out, presumably into solution. Careful analysis of the ADT samples showed that a defect on the Pt shell was the location for initial Pt migration and subsequent Pd leaching. In situ TEM imaging was performed to observe the initial defect location and Pt migration. While the in situ results only observe the early stages due to time constraints, the direct images allowed for us to see how the structure was elongating in the corner-to-corner direction while compressing from the side-to-side direction. We can see the shell shape adjust before stabilizing. An analysis of the E-chip afterwards found the presence of small nodules of Pt, showing that one of the early steps toward nanocages is the migration of Pt away from the facet of the octahedron.

As shown, in situ TEM gives insights into processes at the nanoscale, providing spatial information that is not present with macroscopic spectroscopic techniques. This gives a view into reactions that previously were seen indirectly. However, the types of reactions that can be replicated are still limited. Advancements to MEMS technology will help with replication. For example, the incorporation of a fiber optic cable into the liquid cell holder would enable in situ observations of a photocatalytic nanomaterials. Other potentials are to convert liquid into a gaseous form for the gas/liquid cell, to allow for the monitoring of oxidizing reactions in a wet environment without much loss of spatial resolution.[178,179] Other microscopy techniques that can be applied in situ, not mentioned here, include STEM diffraction imaging to explore lattice strain and local electromagnetic fields.[180–183] However, as a microscopic technique, the TEM should be used alongside other spectroscopic techniques to get both an overview and details at the nanoscale. In situ electron microscopy has expanded the ways researchers can probe materials with higher and higher spatial and energy resolution; with future technological development on the holders in particular, in situ TEM imaging and spectroscopy will continue to be a powerful tool for investigating nanomaterial transformations.

References

(1) Volokitin, Y.; Sinzig, J.; De Jongh, L. J.; Schmidt, G.; Vargaftik, M. N.; Moiseev, I. I. Quantum-Size Effects in the Thermodynamic Properties of Metallic Nanoparticles. *Nature* **1996**, *384* (6610), 621–623.

(2) Sikam, P.; Thirayatorn, R.; Moontragoon, P.; Kaewmaraya, T.; Amornkitbamrung, V.; Ikonic, Z. The Quantum Confined Stark Effect in N-Doped ZnO/ZnO/N-Doped ZnO Nanostructures for Infrared and Terahertz Applications. *Nanotechnology* **2020**, *31* (44), 445207.

(3) Zhang, S.; Plessow, P. N.; Willis, J. J.; Dai, S.; Xu, M.; Graham, G. W.; Cargnello, M.; Abild-Pedersen, F.; Pan, X. Dynamical Observation and Detailed Description of Catalysts under Strong Metal-Support Interaction. *Nano Lett.* **2016**, *16* (7), 4528–4534.

(4) Han, B.; Guo, Y.; Huang, Y.; Xi, W.; Xu, J.; Luo, J.; Qi, H.; Ren, Y.; Liu, X.; Qiao, B.; et al. Strong Metal–Support Interactions between Pt Single Atoms and TiO2. *Angew. Chem. Int. Ed.* **2020**, *59* (29), 11824–11829.

(5) Ohka, T.; Akiyama, T.; Pradipto, A. M.; Nakamura, K.; Ito, T. Effect of Step Edges on Adsorption Behavior for GaN(0001) Surfaces during Metalorganic Vapor Phase Epitaxy: An Ab Initio Study. *Cryst. Growth Des.* **2020**, *20* (7), 4358–4365.

(6) Zhou, X.; Chen, L.; Sterbinsky, G. E.; Mukherjee, D.; Unocic, R. R.; Tait, S. L. Pt-Ligand Single-Atom Catalysts: Tuning Activity by Oxide Support Defect Density. *Catal. Sci. Technol.* **2020**, *10* (10), 3353–3365.

(7) Cheng, L.; Yin, H.; Cai, C.; Fan, J.; Xiang, Q. Single Ni Atoms Anchored on Porous Few-Layer g-C3N4 for Photocatalytic CO2 Reduction: The Role of Edge Confinement. *Small* **2020**, *16* (28), 2002411.

(8) Zhang, Z. Surface Effects in the Energy Loss near Edge Structure of Different Cobalt Oxides. *Ultramicroscopy* **2007**, *107* (8), 598–603.

(9) DeRita, L.; Resasco, J.; Dai, S.; Boubnov, A.; Thang, H. V.; Hoffman, A. S.; Ro, I.; Graham, G. W.; Bare, S. R.; Pacchioni, G.; et al. Structural Evolution of Atomically Dispersed Pt Catalysts Dictates Reactivity. *Nat. Mater.* **2019**, *18* (7), 746–751.

(10) Shi, F.; Gao, W.; Shan, H.; Li, F.; Xiong, Y.; Peng, J.; Xiang, Q.; Chen, W.; Tao, P.; Song, C.; et al. Strain-Induced Corrosion Kinetics at Nanoscale Are Revealed in Liquid: Enabling Control of Corrosion Dynamics of Electrocatalysis. *J. Clean. Prod.* **2020**, *6* (9), 2257–2271.

(11) Xi, W.; Wang, K.; Shen, Y.; Ge, M.; Deng, Z.; Zhao, Y.; Cao, Q.; Ding, Y.; Hu, G.; Luo, J. Dynamic Co-Catalysis of Au Single Atoms and Nanoporous Au for Methane Pyrolysis. *Nat. Commun.* **2020**, *11* (1), 1919.

(12) Fultz, B.; Howe, J. M. *Transmission Electron Microscopy and Diffractometry of Materials*; Springer Berlin Heidelberg: Berlin, Heidelberg, 2002.

(13) Williams, D. B.; Carter, C. B. *Transmission Electron Microscopy*; Springer US: Boston,

MA, 2009.

(14) Xin, H. L.; Muller, D. A. Aberration-Corrected ADF-STEM Depth Sectioning and Prospects for Reliable 3D Imaging in STEM. *J. Electron Microsc. (Tokyo).* **2009**, *58* (3), 157–165.

(15) Zeitler, E. *Scanning Transmission Electron Microscopy*; Pennycook, S. J., Nellist, P. D., Eds.; Springer New York: New York, NY, 2011.

(16) Lee, S.; Sun, X. G.; Lubimtsev, A. A.; Gao, X.; Ganesh, P.; Ward, T. Z.; Eres, G.; Chisholm, M. F.; Dai, S.; Lee, H. N. Persistent Electrochemical Performance in Epitaxial VO2(B). *Nano Lett.* **2017**, *17* (4), 2229–2233.

(17) Bañares, M. A. Preface. *Catal. Today* **2007**, *126*, 1–2.

(18) Lugg, N. R.; Kothleitner, G.; Shibata, N.; Ikuhara, Y. On the Quantitativeness of EDS STEM. *Ultramicroscopy* **2015**, *151*, 150–159.

(19) Stroud, R. M.; Lovejoy, T. C.; Falke, M.; Bassim, N. D.; Corbin, G. J.; Dellby, N.; Hrncirik, P.; Kaeppel, A.; Noack, M.; Hahn, W.; et al. Individual Heteroatom Identification with X-Ray Spectroscopy. *Appl. Phys. Lett.* **2016**, *108* (16), 163101.

(20) Lovejoy, T. C.; Ramasse, Q. M.; Falke, M.; Kaeppel, A.; Terborg, R.; Zan, R.; Dellby, N.; Krivanek, O. L. Single Atom Identification by Energy Dispersive X-Ray Spectroscopy. *Appl. Phys. Lett.* **2012**, *100* (15), 154101.

(21) Suenaga, K.; Okazaki, T.; Okunishi, E.; Matsumura, S. Detection of Photons Emitted from Single Erbium Atoms in Energy-Dispersive X-Ray Spectroscopy. *Nat. Photonics* **2012**, *6* (8), 545–548.

(22) Hart, J. L.; Lang, A. C.; Leff, A. C.; Longo, P.; Trevor, C.; Twesten, R. D.; Taheri, M. L. Direct Detection Electron Energy-Loss Spectroscopy: A Method to Push the Limits of Resolution and Sensitivity. *Sci. Rep.* **2017**, *7* (1), 8243.

(23) Yan, X.; Liu, C.; Gadre, C. A.; Dai, S.; Gu, L.; Yu, K.; Aoki, T.; Wu, R.; Pan, X. Unexpected Strong Thermally Induced Phonon Energy Shift for Mapping Local Temperature. *Nano Lett.* **2019**, *19* (10), 7494–7502.

(24) Mundy, J. A.; Mao, Q.; Brooks, C. M.; Schlom, D. G.; Muller, D. A. Atomic-Resolution Chemical Imaging of Oxygen Local Bonding Environments by Electron Energy Loss Spectroscopy. *Appl. Phys. Lett.* **2012**, *101* (4), 0–5.

(25) Wang, Y.; Huang, M. R. S.; Salzberger, U.; Hahn, K.; Sigle, W.; van Aken, P. A. Towards Atomically Resolved EELS Elemental and Fine Structure Mapping via Multi-Frame and Energy-Offset Correction Spectroscopy. *Ultramicroscopy* **2018**, *184*, 98–105.

(26) Egerton, R. F.; Watanabe, M. Characterization of Single-Atom Catalysts by EELS and EDX Spectroscopy. *Ultramicroscopy* **2018**, *193* (June), 111–117.

(27) Gao, Z.; Li, A.; Ma, D.; Zhou, W. Electron Energy Loss Spectroscopy for Single Atom Catalysis. *Top. Catal.* **2022**, *65* (17–18), 1609–1619.

(28) Krivanek, O. L.; Lovejoy, T. C.; Dellby, N.; Aoki, T.; Carpenter, R. W.; Rez, P.;

Soignard, E.; Zhu, J.; Batson, P. E.; Lagos, M. J.; et al. Vibrational Spectroscopy in the Electron Microscope. *Nature* **2014**, *514* (7521), 209–212.

(29) Haiber, D. M.; Crozier, P. A. Nanoscale Probing of Local Hydrogen Heterogeneity in Disordered Carbon Nitrides with Vibrational Electron Energy-Loss Spectroscopy. *ACS Nano* **2018**, *12* (6), 5463–5472.

(30) Hachtel, J. A.; Huang, J.; Popovs, I.; Jansone-Popova, S.; Keum, J. K.; Jakowski, J.; Lovejoy, T. C.; Dellby, N.; Krivanek, O. L.; Idrobo, J. C. Identification of Site-Specific Isotopic Labels by Vibrational Spectroscopy in the Electron Microscope. *Science* **2019**, *363* (6426), 525–528.

(31) Zeiger, P. M.; Rusz, J. Efficient and Versatile Model for Vibrational STEM-EELS. *Phys. Rev. Lett.* **2020**, *124* (2), 25501.

(32) Jokisaari, J. R.; Hachtel, J. A.; Hu, X.; Mukherjee, A.; Wang, C.; Konecna, A.; Lovejoy, T. C.; Dellby, N.; Aizpurua, J.; Krivanek, O. L.; et al. Vibrational Spectroscopy of Water with High Spatial Resolution. *Adv. Mater.* **2018**, *30* (36), 1–6.

(33) Venkatraman, K.; Rez, P.; March, K.; Crozier, P. A. The Influence of Surfaces and Interfaces on High Spatial Resolution Vibrational EELS from SiO2. *Microscopy* **2018**, *67* (February), i14–i23.

(34) Hage, F. S.; Nicholls, R. J.; Yates, J. R.; Mcculloch, D. G.; Lovejoy, T. C.; Dellby, N.; Krivanek, O. L.; Refson, K.; Ramasse, Q. M. Nanoscale Momentum-Resolved Vibrational Spectroscopy. *Sci. Adv.* **2018**, *1* (June), 1–7.

(35) Collins, S. M.; Kepaptsoglou, D. M.; Hou, J.; Ashling, C. W.; Radtke, G.; Bennett, T. D.; Midgley, P. A.; Ramasse, Q. M. Functional Group Mapping by Electron Beam Vibrational Spectroscopy from Nanoscale Volumes. *Nano Lett.* **2020**, *20*, 1272–1279.

(36) Jones, J.; Xiong, H.; DeLaRiva, A. T.; Peterson, E. J.; Pham, H.; Challa, S. R.; Qi, G.; Oh, S.; Wiebenga, M. H.; Hernández, X. I. P.; et al. Thermally Stable Single-Atom Platinum-on-Ceria Catalysts via Atom Trapping. *Science* **2016**, *353* (6295), 150–154.

(37) Mitchell, M. B. Fundamentals and Applications of Diffuse Reflectance Infrared Fourier Transform (DRIFT) Spectroscopy; 1993; pp 351–375.

(38) Zhang, X.; Cui, G.; Feng, H.; Chen, L.; Wang, H.; Wang, B.; Zhang, X.; Zheng, L.; Hong, S.; Wei, M. Platinum–Copper Single Atom Alloy Catalysts with High Performance towards Glycerol Hydrogenolysis. *Nat. Commun.* **2019**, *10* (1), 5812.

(39) Hadjivanov, K. I.; Vayssilov, G. N. Characterization of Oxide Surfaces and Zeolites by Carbon Monoxide as an IR Probe Molecule. *ChemInform* **2003**, *34* (17), 47008.

(40) Resasco, J.; Dai, S.; Graham, G.; Pan, X.; Christopher, P. Combining In-Situ Transmission Electron Microscopy and Infrared Spectroscopy for Understanding Dynamic and Atomic-Scale Features of Supported Metal Catalysts. *J. Phys. Chem. C* **2018**, *122* (44), 25143–25157.

(41) Matsubu, J. C.; Zhang, S.; DeRita, L.; Marinkovic, N. S.; Chen, J. G.; Graham, G. W.; Pan, X.; Christopher, P. Adsorbate-Mediated Strong Metal-Support Interactions in Oxide-

Supported Rh Catalysts. *Nat. Chem.* **2017**, *9* (2), 120–127.

(42) Georgieva, I.; Kostova, I.; Trendafilova, N.; Rastogi, V. K.; Bauer, G.; Kiefer, W. Raman, FT-IR and DFT Studies Ofortho-,Meta- Andpara-Pyridinomethylene Substituted Di(4-Hydroxy-Coumarin) and Their Ce(III), La(III) and Nd(III) Complexes. *J. Raman Spectrosc.* **2006**, *37* (7), 742–754.

(43) Li, X.; Yang, X.; Zhang, J.; Huang, Y.; Liu, B. In Situ/Operando Techniques for Characterization of Single-Atom Catalysts. *ACS Catal.* **2019**, *9* (3), 2521–2531.

(44) Ravel, B.; Newville, M. ATHENA, ARTEMIS, HEPHAESTUS: Data Analysis for X-Ray Absorption Spectroscopy Using IFEFFIT. *J. Synchrotron Radiat.* **2005**, *12* (4), 537–541.

(45) Stern E A; Sayers D E; Lytle F W. Extended X-Ray-Absorption Fine-Structure Technique. III. Determination of Physical Parameters. *Phys. Rev. B* **1975**, *11* (12), 4836–4846.

(46) Lee, P. A.; Citrin, P. H.; Eisenberger, P.; Kincaid, B. M. Extended X-Ray Absorption Fine Structure Its Strengths and Limitations as a Structural Tool. *Rev. Mod. Phys.* **1981**, *53* (4), 769–806.

(47) Tanuma, S.; Powell, C. J.; Penn, D. R. Calculation of Electron Inelastic Mean Free Paths (IMFPs) VII. Reliability of the TPP-2M IMFP Predictive Equation. *Surf. Interface Anal.* **2003**, *35* (3), 268–275.

(48) Suh, M. P.; Park, H. J.; Prasad, T. K.; Lim, D.-W. Hydrogen Storage in Metal-Organic Frameworks. *Chem. Rev.* **2012**, *112* (112), 782–835.

(49) Saha, S.; Chandra, S.; Garai, B.; Banerjee, R. Carbon Dioxide Capture by Metal Organic Frameworks. *Indian J. Chem. - Sect. A Inorganic, Phys. Theor. Anal. Chem.* **2012**, *51* (9–10), 1223–1230.

(50) Wu, H.; Gong, Q.; Olson, D. H.; Li, J. Commensurate Adsorption of Hydrocarbons and Alcohols in Microporous Metal Organic Frameworks. *Chem. Rev.* **2012**, *112* (2), 836–868.

(51) Yoon, M.; Srirambalaji, R.; Kim, K. Homochiral Metal-Organic Frameworks for Asymmetric Heterogeneous Catalysis. *Chem. Rev.* **2012**, *112* (2), 1196–1231.

(52) Wang, Q.; Astruc, D. State of the Art and Prospects in Metal-Organic Framework (MOF)-Based and MOF-Derived Nanocatalysis. *Chem. Rev.* **2019**, *120*, 1438–1511.

(53) Yoon, M.; Suh, K.; Natarajan, S.; Kim, K. Proton Conduction in Metal-Organic Frameworks and Related Modularly Built Porous Solids. *Angew. Chem. Int. Ed.* **2013**, *52* (10), 2688–2700.

(54) Xing, X. S.; Fu, Z. H.; Zhang, N. N.; Yu, X. Q.; Wang, M. S.; Guo, G. C. High Proton Conduction in an Excellent Water-Stable Gadolinium Metal-Organic Framework. *Chem. Commun.* **2019**, *55* (9), 1241–1244.

(55) Joarder, B.; Lin, J. Bin; Romero, Z.; Shimizu, G. K. H. Single Crystal Proton Conduction Study of a Metal Organic Framework of Modest Water Stability. *J. Am. Chem. Soc.* **2017**,

139 (21), 7176–7179.

(56) Chen, B.; Eddaoudi, M.; Reineke, T. M.; Kampf, J. W.; O'Keeffe, M.; Yaghi, O. M. Cu2(ATC)·6H2O: Design of Open Metal Sites in Porous Metal-Organic Crystals (ATC: 1,3,5,7-Adamantane Tetracarboxylate). *J. Am. Chem. Soc.* **2000**, *122* (46), 11559–11560.

(57) Seo, J. S.; Whang, D.; Lee, H.; Jun, S. I.; Oh, J.; Jeon, Y. J.; Kim, K. A Homochiral Metal-Organic Porous Material for Enantioselective Separation and Catalysis. *Nature* **2000**, *404* (6781), 982–986.

(58) Gao, J.; Li, Z.; Deng, Z.; Liu, M.; Wei, W.; Zheng, C.; Zhang, Y.; Chen, S.; Deng, P. Rapid Removal of Mercury from Water by Novel Mof/Pp Hybrid Membrane. *Nanomaterials* **2021**, *11* (10), 1–9.

(59) Yan, X.; Li, P.; Song, X.; Li, J.; Ren, B.; Gao, S.; Cao, R. Recent Progress in the Removal of Mercury Ions from Water Based MOFs Materials. *Coord. Chem. Rev.* **2021**, *443*, 214034.

(60) Li, Y.; Tan, M.; Liu, G.; Si, D.; Chen, N.; Zhou, D. Thiol-Functionalized Metal-Organic Frameworks Embedded with Chelator-Modified Magnetite for High-Efficiency and Recyclable Mercury Removal in Aqueous Solutions. *J. Mater. Chem. A* **2022**, *10* (12), 6724–6730.

(61) Banihashemi, F.; Bu, G.; Thaker, A.; Williams, D.; Lin, J. Y. S.; Nannenga, B. L. Beam-Sensitive Metal-Organic Framework Structure Determination by Microcrystal Electron Diffraction. *Ultramicroscopy* **2020**, *216* (April), 113048.

(62) Liu, L.; Zhang, D.; Zhu, Y.; Han, Y. Bulk and Local Structures of Metal–Organic Frameworks Unravelled by High-Resolution Electron Microscopy. *Commun. Chem.* **2020**, *3* (1), 1–14.

(63) Wiktor, C.; Meledina, M.; Turner, S.; Lebedev, O. I.; Fischer, R. A. Transmission Electron Microscopy on Metal-Organic Frameworks-a Review. *J. Mater. Chem. A* **2017**, *5* (29), 14969–14989.

(64) Chen, Q.; Dwyer, C.; Sheng, G.; Zhu, C.; Li, X.; Zheng, C.; Zhu, Y. Imaging Beam-Sensitive Materials by Electron Microscopy. *Adv. Mater.* **2020**, *32* (16), 1907619.

(65) Zhu, L.; Zhang, D.; Xue, M.; Li, H.; Qiu, S. Direct Observations of the MOF (UiO-66) Structure by Transmission Electron Microscopy. *CrystEngComm* **2013**, *15* (45), 9356–9359.

(66) Deng, M.; Bo, X.; Guo, L. Encapsulation of Platinum Nanoparticles into a Series of Zirconium-Based Metal-Organic Frameworks: Effect of the Carrier Structures on Electrocatalytic Performances of Composites. *J. Electroanal. Chem.* **2018**, *815* (January), 198–209.

(67) Wei, Y. P.; Liu, Y.; Guo, F.; Dao, X. Y.; Sun, W. Y. Different Functional Group Modified Zirconium Frameworks for the Photocatalytic Reduction of Carbon Dioxide. *Dalt. Trans.* **2019**, *48* (23), 8221–8226.

(68) Wang, C.; Guo, Z.; Shen, W.; Zhang, A.; Xu, Q.; Liu, H.; Wang, Y. Application of Sulfur-

Doped Carbon Coating on the Surface of Li3V2(PO4)3 Composites to Facilitate Li-Ion Storage as Cathode Materials. *J. Mater. Chem. A* **2015**, *3* (11), 6064–6072.

(69) Stankovich, S.; Dikin, D. A.; Piner, R. D.; Kohlhaas, K. A.; Kleinhammes, A.; Jia, Y.; Wu, Y.; Nguyen, S. B. T.; Ruoff, R. S. Synthesis of Graphene-Based Nanosheets via Chemical Reduction of Exfoliated Graphite Oxide. *Carbon N. Y.* **2007**, *45* (7), 1558–1565.

(70) Lindberg, B. J.; Hamrin, K.; Johansson, G.; Gelius, U.; Fahlman, A.; Nordling, C.; Siegbahn, K. Molecular Spectroscopy by Means of ESCA II. Sulfur Compounds. Correlation of Electron Binding Energy with Structure. *Phys. Scr.* **1970**, *1* (5–6), 286–298.

(71) Thompson, C. J.; Meyer, R. A.; Ball, J. S. Thermal Decomposition of Sulfur Compounds. II. 1-Pentanethiol. *J. Am. Chem. Soc.* **1952**, *74* (13), 3287–3289.

(72) Trovarelli, A. Catalytic Properties of Ceria and CeO2-Containing Materials. *Catal. Rev. - Sci. Eng.* **1996**, *38* (4), 439–520.

(73) Aireddy, D. R.; Ding, K. Heterolytic Dissociation of H2in Heterogeneous Catalysis. *ACS Catal.* **2022**, *12* (8), 4707–4723.

(74) Xing, F.; Nakaya, Y.; Yasumura, S.; Shimizu, K. ichi; Furukawa, S. Ternary Platinum–Cobalt–Indium Nanoalloy on Ceria as a Highly Efficient Catalyst for the Oxidative Dehydrogenation of Propane Using CO2. *Nat. Catal.* **2022**, *5* (1), 55–65.

(75) Zhang, Q.; Bu, J.; Wang, J.; Sun, C.; Zhao, D.; Sheng, G.; Xie, X.; Sun, M.; Yu, L. Highly Efficient Hydrogenation of Nitrobenzene to Aniline over Pt/CeO2Catalysts: The Shape Effect of the Support and Key Role of Additional Ce3+Sites. *ACS Catal.* **2020**, *10* (18), 10350–10363.

(76) Guo, Y.; Mei, S.; Yuan, K.; Wang, D. J.; Liu, H. C.; Yan, C. H.; Zhang, Y. W. Low-Temperature CO2 Methanation over CeO2-Supported Ru Single Atoms, Nanoclusters, and Nanoparticles Competitively Tuned by Strong Metal-Support Interactions and H-Spillover Effect. *ACS Catal.* **2018**, *8* (7), 6203–6215.

(77) Kalamaras, C. M.; Americanou, S.; Efstathiou, A. M. "Redox" vs "Associative Formate with -OH Group Regeneration" WGS Reaction Mechanism on Pt/CeO2: Effect of Platinum Particle Size. *J. Catal.* **2011**, *279* (2), 287–300.

(78) Vecchietti, J.; Bonivardi, A.; Xu, W.; Stacchiola, D.; Delgado, J. J.; Calatayud, M.; Collins, S. E. Understanding the Role of Oxygen Vacancies in the Water Gas Shift Reaction on Ceria-Supported Platinum Catalysts. *ACS Catal.* **2014**, *4* (6), 2088–2096.

(79) Gao, Y.; Li, R.; Chen, S.; Luo, L.; Cao, T.; Huang, W. Morphology-Dependent Interplay of Reduction Behaviors, Oxygen Vacancies and Hydroxyl Reactivity of CeO2 Nanocrystals. *Phys. Chem. Chem. Phys.* **2015**, *17* (47), 31862–31871.

(80) Barrabés, N.; Föttinger, K.; Llorca, J.; Dafinov, A.; Medina, F.; Sá, J.; Hardacre, C.; Rupprechter, G. Pretreatment Effect on Pt/CeO2 Catalyst in the Selective Hydrodechlorination of Trichloroethylene. *J. Phys. Chem. C* **2010**, *114* (41), 17675–17682.

(81) Zhang, F.; Gutiérrez, R. A.; Lustemberg, P. G.; Liu, Z.; Rui, N.; Wu, T.; Ramírez, P. J.;

Xu, W.; Idriss, H.; Ganduglia-Pirovano, M. V.; et al. Metal-Support Interactions and C1 Chemistry: Transforming Pt-CeO2into a Highly Active and Stable Catalyst for the Conversion of Carbon Dioxide and Methane. *ACS Catal.* **2021**, *11* (3), 1613–1623.

(82) Bugrova, T. A.; Kharlamova, T. S.; Svetlichnyi, V. A.; Savel'eva, A. S.; Salaev, M. A.; Mamontov, G. V. Insights into Formation of Pt Species in Pt/CeO2 Catalysts: Effect of Treatment Conditions and Metal-Support Interaction. *Catal. Today* **2021**, *375*, 36–47.

(83) Tong, T.; Douthwaite, M.; Chen, L.; Engel, R.; Conway, M. B.; Guo, W.; Wu, X. P.; Gong, X. Q.; Wang, Y.; Morgan, D. J.; et al. Uncovering Structure-Activity Relationships in Pt/CeO2 Catalysts for Hydrogen-Borrowing Amination. *ACS Catal.* **2023**, *13* (2), 1207–1220.

(84) Karim, W.; Spreafico, C.; Kleibert, A.; Gobrecht, J.; Vandevondele, J.; Ekinci, Y.; Van Bokhoven, J. A. Catalyst Support Effects on Hydrogen Spillover. *Nature* **2017**, *541* (7635), 68–71.

(85) Beck, A.; Kazazis, D.; Ekinci, Y.; Li, X.; Müller Gubler, E. A.; Kleibert, A.; Willinger, M. G.; Artiglia, L.; Van Bokhoven, J. A. The Extent of Platinum-Induced Hydrogen Spillover on Cerium Dioxide. *ACS Nano* **2022**.

(86) Lykhach, Y.; Staudt, T.; Vorokhta, M.; Skála, T.; Johánek, V.; Prince, K. C.; Matolín, V.; Libuda, J. Hydrogen Spillover Monitored by Resonant Photoemission Spectroscopy. *J. Catal.* **2012**, *285* (1), 6–9.

(87) Prins, R. Hydrogen Spillover. Facts and Fiction. *Chem. Rev.* **2012**, *112* (5), 2714–2738.

(88) Lin, W.; Herzing, A. A.; Kiely, C. J.; Wachs, I. E. Probing Metal-Support Interactions under Oxidizing and Reducing Conditions: In Situ Raman and Infrared Spectroscopic and Scanning Transmission Electron Microscopic-X-Ray Energy-Dispersive Spectroscopic Investigation of Supported Platinum Catalysts. *J. Phys. Chem. C* **2008**, *112* (15), 5942–5951.

(89) Puigdollers, A. R.; Schlexer, P.; Tosoni, S.; Pacchioni, G. Increasing Oxide Reducibility: The Role of Metal/Oxide Interfaces in the Formation of Oxygen Vacancies. *ACS Catal.* **2017**, *7* (10), 6493–6513.

(90) Chen, A.; Yu, X.; Zhou, Y.; Miao, S.; Li, Y.; Kuld, S.; Sehested, J.; Liu, J.; Aoki, T.; Hong, S.; et al. Structure of the Catalytically Active Copper–Ceria Interfacial Perimeter. *Nat. Catal.* **2019**, *2* (4), 334–341.

(91) Lawrence, E. L.; Crozier, P. A. Oxygen Transfer at Metal-Reducible Oxide Nanocatalyst Interfaces: Contrasting Carbon Growth from Ethane and Ethylene. *ACS Appl. Nano Mater.* **2018**, *1* (3), 1360–1369.

(92) Kropp, T.; Lu, Z.; Li, Z.; Chin, Y. H. C.; Mavrikakis, M. Anionic Single-Atom Catalysts for CO Oxidation: Support-Independent Activity at Low Temperatures. *ACS Catal.* **2019**, *9* (2), 1595–1604.

(93) Bliem, R.; van der Hoeven, J.; Zavodny, A.; Gamba, O.; Pavelec, J.; de Jongh, P. E.; Schmid, M.; Diebold, U.; Parkinson, G. S. An Atomic-Scale View of CO and H 2 Oxidation on a Pt/Fe 3 O 4 Model Catalyst. *Angew. Chemie Int. Ed.* **2015**, *54* (47), 13999–

14002.

(94) Lin, Y.; Zhou, M.; Tai, X.; Li, H.; Han, X.; Yu, J. Analytical Transmission Electron Microscopy for Emerging Advanced Materials. *Matter* **2021**, *4* (7), 2309–2339.

(95) Collins, S. M.; Fernandez-Garcia, S.; Calvino, J. J.; Midgley, P. A. Sub-Nanometer Surface Chemistry and Orbital Hybridization in Lanthanum-Doped Ceria Nano-Catalysts Revealed by 3D Electron Microscopy. *Sci. Rep.* **2017**, *7* (1), 1–9.

(96) Wang, R.; Crozier, P. A.; Sharma, R.; Adams, J. B. Measuring the Redox Activity of Individual Catalytic Nanoparticles in Cerium-Based Oxides. *Nano Lett.* **2008**, *8* (3), 962–967.

(97) Zhang, J.; Huang, F.; Lin, Z. Progress of Nanocrystalline Growth Kinetics Based on Oriented Attachment. *Nanoscale* **2010**, *2* (1), 18–34.

(98) Nkou Bouala, G. I.; Clavier, N.; Martin, S.; Léchelle, J.; Favrichon, J.; Brau, H. P.; Dacheux, N.; Podor, R. From in Situ HT-ESEM Observations to Simulation: How Does Polycrystallinity Affects the Sintering of CeO2 Microspheres? *J. Phys. Chem. C* **2016**, *120* (1), 386–395.

(99) Nkou Bouala, G. I.; Clavier, N.; Léchelle, J.; Mesbah, A.; Dacheux, N.; Podor, R. In Situ HT-ESEM Study of Crystallites Growth within CeO2 Microspheres. *Ceram. Int.* **2015**, *41* (10), 14703–14711.

(100) Scardi, P.; Leoni, M.; Müller, M.; Di Maggio, R. In Situ Size-Strain Analysis of Nanocrystalline Ceria Growth. *Mater. Sci. Eng. A* **2010**, *528* (1), 77–82.

(101) Watanabe, M.; Seki, T. Initial Sintering Kinetics of Non-Stoichiometric CeO2−x. *Mater. Sci. Eng. B Solid-State Mater. Adv. Technol.* **2021**, *272* (July), 1–6.

(102) Ross, F. M. Opportunities and Challenges in Liquid Cell Electron Microscopy. *Science* **2015**, *350* (6267), aaa9886.

(103) Pu, S.; Gong, C.; Robertson, A. W. Liquid Cell Transmission Electron Microscopy and Its Applications. *R. Soc. Open Sci.* **2020**, *7* (1).

(104) Park, J.; Koo, K.; Noh, N.; Chang, J. H.; Cheong, J. Y.; Dae, K. S.; Park, J. S.; Ji, S.; Kim, I. D.; Yuk, J. M. Graphene Liquid Cell Electron Microscopy: Progress, Applications, and Perspectives. *ACS Nano* **2021**, *15* (1), 288–308.

(105) Wang, C.; Qiao, Q.; Shokuhfar, T.; Klie, R. F. High-Resolution Electron Microscopy and Spectroscopy of Ferritin in Biocompatible Graphene Liquid Cells and Graphene Sandwiches. *Adv. Mater.* **2014**, *26* (21), 3410–3414.

(106) Regan, W.; Alem, N.; Alemán, B.; Geng, B.; Girit, Ç.; Maserati, L.; Wang, F.; Crommie, M.; Zettl, A. A Direct Transfer of Layer-Area Graphene. *Appl. Phys. Lett.* **2010**, *96* (11).

(107) Sasaki, Y.; Kitaura, R.; Yuk, J. M.; Zettl, A.; Shinohara, H. Efficient Preparation of Graphene Liquid Cell Utilizing Direct Transfer with Large-Area Well-Stitched Graphene. *Chem. Phys. Lett.* **2016**, *650*, 107–112.

(108) Deursen, P. M. G.; Koning, R. I.; Tudor, V.; Moradi, M.; Patterson, J. P.; Kros, A.;

Sommerdijk, N. A. J. M.; Koster, A. J.; Schneider, G. F. Graphene Liquid Cells Assembled through Loop-Assisted Transfer Method and Located with Correlated Light-Electron Microscopy. *Adv. Funct. Mater.* **2020**, *30* (11), 1904468.

(109) Belloni, J. V.; Mostafavi, M.; Douki, T. *Radiation Chemistry: From Basics to Applications in Material and Life Sciences*; EDP Sciences, 2020.

(110) BOAG, J. W.; HART, E. J. Absorption Spectra in Irradiated Water and Some Solutions: Absorption Spectra of 'Hydrated' Electron. *Nature* **1963**, *197* (4862), 45–47.

(111) Lee, J.; Nicholls, D.; Browning, N. D.; Mehdi, B. L. Controlling Radiolysis Chemistry on the Nanoscale in Liquid Cell Scanning Transmission Electron Microscopy. *Phys. Chem. Chem. Phys.* **2021**, *23* (33), 17766–17773.

(112) Svoboda, V.; Michiels, R.; LaForge, A. C.; Med, J.; Stienkemeier, F.; Slavíček, P.; Wörner, H. J. Real-Time Observation of Water Radiolysis and Hydrated Electron Formation Induced by Extreme-Ultraviolet Pulses. *Sci. Adv.* **2020**, *6* (3), 1–9.

(113) Siwek, M.; Edgecock, T. Application of Electron Beam Water Radiolysis for Sewage Sludge Treatment—a Review. *Environ. Sci. Pollut. Res.* **2020**, *27* (34), 42424–42448.

(114) Yu, X.; Cheng, G.; Zheng, S. Y. Synthesis of Self-Assembled Multifunctional Nanocomposite Catalysts with Highly Stabilized Reactivity and Magnetic Recyclability. *Sci. Rep.* **2016**, *6* (December 2015), 1–11.

(115) Tan, C.; Zhang, H. Wet-Chemical Synthesis and Applications of Non-Layer Structured Two-Dimensional Nanomaterials. *Nat. Commun.* **2015**, *6*.

(116) Wang, D.; Bierwagen, G. P. Sol-Gel Coatings on Metals for Corrosion Protection. *Prog. Org. Coatings* **2009**, *64* (4), 327–338.

(117) Vayssieres, L. Growth of Arrayed Nanorods and Nanowires of ZnO from Aqueous Solutions. *Adv. Mater.* **2003**, *15* (5), 464–466.

(118) Park, J.; Joo, J.; Soon, G. K.; Jang, Y.; Hyeon, T. Synthesis of Monodisperse Spherical Nanocrystals. *Angew. Chem. Int. Ed.* **2007**, *46* (25), 4630–4660.

(119) Orsini, A.; Falconi, C. Real-Time Monitoring of the Solution Growth of ZnO Nanorods Arrays by Quartz Microbalances and in-Situ Temperature Sensors. *Sci. Rep.* **2014**, *4*, 1–7.

(120) Soon, G. K.; Hyeon, T. Colloidal Chemical Synthesis and Formation Kinetics of Uniformly Sized Nanocrystals of Metals, Oxides, and Chalcogenides. *Acc. Chem. Res.* **2008**, *41* (12), 1696–1709.

(121) Guardia, P.; Labarta, A.; Batlle, X. Tuning the Size, the Shape, and the Magnetic Properties of Iron Oxide Nanoparticles. *J. Phys. Chem. C* **2011**, *115* (2), 390–396.

(122) Lisiecki, I. Size, Shape, and Structural Control of Metallic Nanocrystals. *J. Phys. Chem. B* **2005**, *109* (25), 12231–12244.

(123) Boles, M. A.; Engel, M.; Talapin, D. V. Self-Assembly of Colloidal Nanocrystals: From Intricate Structures to Functional Materials. *Chem. Rev.* **2016**, *116* (18), 11220–11289.

(124) Woehl, T. J.; Evans, J. E.; Arslan, I.; Ristenpart, W. D.; Browning, N. D. Direct in Situ Determination of the Mechanisms Controlling Nanoparticle Nucleation and Growth. *ACS Nano* **2012**, *6* (10), 8599–8610.

(125) Ferrah, D.; Haines, A. R.; Galhenage, R. P.; Bruce, J. P.; Babore, A. D.; Hunt, A.; Waluyo, I.; Hemminger, J. C. Wet Chemical Growth and Thermocatalytic Activity of Cu-Based Nanoparticles Supported on TiO2 Nanoparticles/HOPG: In Situ Ambient Pressure XPS Study of the CO2 Hydrogenation Reaction. *ACS Catal.* **2019**, *9* (8), 6783–6802.

(126) Taing, J.; Cheng, M. H.; Hemminger, J. C. Photodeposition of Ag or Pt onto TiO2 Nanoparticles Decorated on Step Edges of HOPG. *ACS Nano* **2011**, *5* (8), 6325–6333.

(127) Kubota, H. T. S. M. M. Y. T. T. Y. M. T. Specific Volume and Viscosity of Methanol-Water Mixtures under High Pressure. *Rev. Phys. Chem. Japan* **1980**, *49* (2), 59–69.

(128) Wenderich, K.; Mul, G. Methods, Mechanism, and Applications of Photodeposition in Photocatalysis: A Review. *Chem. Rev.* **2016**, *116* (23), 14587–14619.

(129) De Yoreo, J. J.; Gilbert, P. U. P. A.; Sommerdijk, N. A. J. M.; Penn, R. L.; Whitelam, S.; Joester, D.; Zhang, H.; Rimer, J. D.; Navrotsky, A.; Banfield, J. F.; et al. Crystallization by Particle Attachment in Synthetic, Biogenic, and Geologic Environments. *Science* **2015**, *349* (6247).

(130) Liao, H. G.; Cui, L.; Whitelam, S.; Zheng, H. Real-Time Imaging of Pt3Fe Nanorod Growth in Solution. *Science* **2012**, *336* (6084), 1011–1014.

(131) Peng, X.; Manna, L.; Yang, W.; Wickham, J. Shape Control of CdSe Nanocrystals Shape Control of CdSe Nanocrystals. *Lett. to Nat.* **2016**, *404* (March 2000), 59–61.

(132) You, H.; Fang, J. Particle-Mediated Nucleation and Growth of Solution-Synthesized Metal Nanocrystals: A New Story beyond the LaMer Curve. *Nano Today* **2016**, *11* (2), 145–167.

(133) Woehl, T. J.; Prozorov, T. The Mechanisms for Nanoparticle Surface Diffusion and Chain Self-Assembly Determined from Real-Time Nanoscale Kinetics in Liquid. *J. Phys. Chem. C* **2015**, *119* (36), 21261–21269.

(134) Arieli, R.; Marmur, A. Decompression Sickness Bubbles: Are Gas Micronuclei Formed on a Flat Hydrophobic Surface? *Respir. Physiol. Neurobiol.* **2011**, *177* (1), 19–23.

(135) Zhang, L.; Zhang, Y.; Zhang, X.; Li, Z.; Shen, G.; Ye, M.; Fan, C.; Fang, H.; Hu, J. Electrochemically Controlled Formation and Growth of Hydrogen Nanobubbles. *Langmuir* **2006**, *22* (19), 8109–8113.

(136) Polman, A. Solar Steam Nanobubbles. *ACS Nano* **2013**, *7* (1), 15–18.

(137) Angulo, A.; van der Linde, P.; Gardeniers, H.; Modestino, M.; Fernández Rivas, D. Influence of Bubbles on the Energy Conversion Efficiency of Electrochemical Reactors. *Joule* **2020**, *4* (3), 555–579.

(138) Meegoda, J. N.; Aluthgun Hewage, S.; Batagoda, J. H. Stability of Nanobubbles. *Environ. Eng. Sci.* **2018**, *35* (11), 1216–1227.

(139) Ohgaki, K.; Khanh, N. Q.; Joden, Y.; Tsuji, A.; Nakagawa, T. Physicochemical Approach to Nanobubble Solutions. *Chem. Eng. Sci.* **2010**, *65* (3), 1296–1300.

(140) Weijs, J. H.; Lohse, D. Why Surface Nanobubbles Live for Hours. *Phys. Rev. Lett.* **2013**, *110* (5), 1–5.

(141) Park, J. B.; Shin, D.; Kang, S.; Cho, S. P.; Hong, B. H. Distortion in Two-Dimensional Shapes of Merging Nanobubbles: Evidence for Anisotropic Gas Flow Mechanism. *Langmuir* **2016**, *32* (43), 11303–11308.

(142) Xiong, R.; Xu, R. X.; Huang, C.; De Smedt, S.; Braeckmans, K. Stimuli-Responsive Nanobubbles for Biomedical Applications. *Chem. Soc. Rev.* **2021**, *50* (9), 5746–5776.

(143) Yin, Y.; Jiang, X.; Sun, L.; Li, H.; Su, C.; Zhang, Y.; Xu, G.; Li, X.; Zhao, C.; Chen, Y.; et al. Continuous Inertial Cavitation Evokes Massive ROS for Reinforcing Sonodynamic Therapy and Immunogenic Cell Death against Breast Carcinoma. *Nano Today* **2021**, *36*, 101009.

(144) Zhang, M.; Seddon, J. R. T. Nanobubble-Nanoparticle Interactions in Bulk Solutions. *Langmuir* **2016**, *32* (43), 11280–11286.

(145) Wang, Y.; Bhushan, B.; Zhao, X. Nanoindents Produced by Nanobubbles on Ultrathin Polystyrene Films in Water. *Nanotechnology* **2009**, *20* (4).

(146) Seddon, J. R. T.; Lohse, D.; Ducker, W. A.; Craig, V. S. J. A Deliberation on Nanobubbles at Surfaces and in Bulk. *ChemPhysChem* **2012**, *13* (8), 2179–2187.

(147) Fan, Y. W.; Wang, R. Z. Submicrometer-Sized Vaterite Tubes Formed Through Nanobubble-Templated Crystal Growth. *Adv. Mater.* **2005**, *17* (19), 2384–2388.

(148) Atkinson, A. J.; Apul, O. G.; Schneider, O.; Garcia-Segura, S.; Westerhoff, P. Nanobubble Technologies Offer Opportunities to Improve Water Treatment. *Acc. Chem. Res.* **2019**, *52* (5), 1196–1205.

(149) Chipakwe, V.; Jolsterå, R.; Chelgani, S. C. Nanobubble-Assisted Flotation of Apatite Tailings: Insights on Beneficiation Options. *ACS Omega* **2021**, *6* (21), 13888–13894.

(150) Lukianova-Hleb, E. Y.; Ren, X.; Zasadzinski, J. A.; Wu, X.; Lapotko, D. O. Plasmonic Nanobubbles Enhance Efficacy and Selectivity of Chemotherapy Against Drug-Resistant Cancer Cells. *Adv. Mater.* **2012**, *24* (28), 3831–3837.

(151) Hernandez, C.; Gulati, S.; Fioravanti, G.; Stewart, P. L.; Exner, A. A. Cryo-EM Visualization of Lipid and Polymer-Stabilized Perfluorocarbon Gas Nanobubbles - A Step Towards Nanobubble Mediated Drug Delivery. *Sci. Rep.* **2017**, *7* (1), 1–8.

(152) Huang, T. W.; Liu, S. Y.; Chuang, Y. J.; Hsieh, H. Y.; Tsai, C. Y.; Wu, W. J.; Tsai, C. T.; Mirsaidov, U.; Matsudaira, P.; Chang, C. S.; et al. Dynamics of Hydrogen Nanobubbles in KLH Protein Solution Studied with in Situ Wet-TEM. *Soft Matter* **2013**, *9* (37), 8856–8861.

(153) Yang, J.; Alam, S. B.; Yu, L.; Chan, E.; Zheng, H. Dynamic Behavior of Nanoscale Liquids in Graphene Liquid Cells Revealed by in Situ Transmission Electron Microscopy.

Micron **2019**, *116* (September 2018), 22–29.

(154) Nag, S.; Tomo, Y.; Takahashi, K.; Kohno, M. Mechanistic Insights into Nanobubble Merging Studied Using in Situ Liquid-Phase Electron Microscopy. *Langmuir* **2021**, *37* (2), 874–881.

(155) Grogan, J. M.; Schneider, N. M.; Ross, F. M.; Bau, H. H. Bubble and Pattern Formation in Liquid Induced by an Electron Beam. *Nano Lett.* **2014**, *14* (1), 359–364.

(156) Alam, S. B.; Yang, J.; Bustillo, K. C.; Ophus, C.; Ercius, P.; Zheng, H.; Chan, E. M. Hybrid Nanocapsules for: In Situ TEM Imaging of Gas Evolution Reactions in Confined Liquids. *Nanoscale* **2020**, *12* (36), 18606–18615.

(157) Shin, D.; Park, J. B.; Kim, Y. J.; Kim, S. J.; Kang, J. H.; Lee, B.; Cho, S. P.; Hong, B. H.; Novoselov, K. S. Growth Dynamics and Gas Transport Mechanism of Nanobubbles in Graphene Liquid Cells. *Nat. Commun.* **2015**, *6*, 1–6.

(158) De Jonge, N.; Peckys, D. B.; Kremers, G. J.; Piston, D. W. Electron Microscopy of Whole Cells in Liquid with Nanometer Resolution. *Proc. Natl. Acad. Sci. U. S. A.* **2009**, *106* (7), 2159–2164.

(159) Tomo, Y.; Takahashi, K.; Nishiyama, T.; Ikuta, T.; Takata, Y. Nanobubble Nucleation Studied Using Fresnel Fringes in Liquid Cell Electron Microscopy. *Int. J. Heat Mass Transf.* **2017**, *108*, 1460–1465.

(160) Zhang, L.; Roling, L. T.; Wang, X.; Vara, M.; Chi, M.; Liu, J.; Choi, S.; Park, J.; Herron, J. A.; Xie, Z.; et al. Platinum-Based Nanocages with Subnanometer-Thick Walls and Well-Defined, Controllable Facets. *Science* **2015**, *349* (6246), 412–416.

(161) Xiong, Y.; Shan, H.; Zhou, Z.; Yan, Y.; Chen, W.; Yang, Y.; Liu, Y.; Tian, H.; Wu, J.; Zhang, H.; et al. Tuning Surface Structure and Strain in Pd–Pt Core–Shell Nanocrystals for Enhanced Electrocatalytic Oxygen Reduction. *Small* **2017**, *13* (7), 1–8.

(162) Yan, Y.; Shan, H.; Li, G.; Xiao, F.; Jiang, Y.; Yan, Y.; Jin, C.; Zhang, H.; Wu, J.; Yang, D. Epitaxial Growth of Multimetallic Pd@PtM (M = Ni, Rh, Ru) Core-Shell Nanoplates Realized by in Situ-Produced CO from Interfacial Catalytic Reactions. *Nano Lett.* **2016**, *16* (12), 7999–8004.

(163) Bu, L.; Zhang, N.; Guo, S.; Zhang, X.; Li, J.; Yao, J.; Wu, T.; Lu, G.; Ma, J. Y.; Su, D.; et al. Biaxially Strained PtPb/Pt Core/Shell Nanoplate Boosts Oxygen Reduction Catalysis. *Science* **2016**, *354* (6318), 1410–1414.

(164) Xia, Y.; Gilroy, K. D.; Peng, H.-C.; Xia, X. Seed-Mediated Growth of Colloidal Metal Nanocrystals. *Angew. Chemie Int. Ed.* **2017**, *56* (1), 60–95.

(165) Peng, Z.; Yang, H. Synthesis and Oxygen Reduction Electrocatalytic Property of Pt-on-Pd Bimetallic Heteronanostructures. *J. Am. Chem. Soc.* **2009**, *131* (22), 7542–7543.

(166) Park, J.; Zhang, L.; Choi, S. Il; Roling, L. T.; Lu, N.; Herron, J. A.; Xie, S.; Wang, J.; Kim, M. J.; Mavrikakis, M.; et al. Atomic Layer-by-Layer Deposition of Platinum on Palladium Octahedra for Enhanced Catalysts toward the Oxygen Reduction Reaction. *ACS Nano* **2015**, *9* (3), 2635–2647.

(167) Wang, X.; Choi, S. Il; Roling, L. T.; Luo, M.; Ma, C.; Zhang, L.; Chi, M.; Liu, J.; Xie, Z.; Herron, J. A.; et al. Palladium-Platinum Core-Shell Icosahedra with Substantially Enhanced Activity and Durability towards Oxygen Reduction. *Nat. Commun.* **2015**, *6* (May), 1–8.

(168) Wang, X.; Vara, M.; Luo, M.; Huang, H.; Ruditskiy, A.; Park, J.; Bao, S.; Liu, J.; Howe, J.; Chi, M.; et al. Pd@Pt Core-Shell Concave Decahedra: A Class of Catalysts for the Oxygen Reduction Reaction with Enhanced Activity and Durability. *J. Am. Chem. Soc.* **2015**, *137* (47), 15036–15042.

(169) Sasaki, K.; Naohara, H.; Cai, Y.; Choi, Y. M.; Liu, P.; Vukmirovic, M. B.; Wang, J. X.; Adzic, R. R. Core-Protected Platinum Monolayer Shell High-Stability Electrocatalysts for Fuel-Cell Cathodes. *Angew. Chemie Int. Ed.* **2010**, *49* (46), 8602–8607.

(170) Zhou, C. H.; Ma, H. T.; Wang, L. Comparative Study of Oxidation Kinetics for Pure Nickel Oxidized under Tensile and Compressive Stress. *Corros. Sci.* **2010**, *52* (1), 210–215.

(171) Gao, W.; Elnabawy, A. O.; Hood, Z. D.; Shi, Y.; Wang, X.; Roling, L. T.; Pan, X.; Mavrikakis, M.; Xia, Y.; Chi, M. Atomistic Insights into the Nucleation and Growth of Platinum on Palladium Nanocrystals. *Nat. Commun.* **2021**, *12* (1), 1–10.

(172) Shan, H.; Gao, W.; Xiong, Y.; Shi, F.; Yan, Y.; Ma, Y.; Shang, W.; Tao, P.; Song, C.; Deng, T.; et al. Nanoscale Kinetics of Asymmetrical Corrosion in Core-Shell Nanoparticles. *Nat. Commun.* **2018**, *9* (1), 1–9.

(173) Bard, A.; Faulkner, L. *Electrochemical Methods Fundamentals and Applications*; John Wiley & Sons, 2000; Vol. 2.

(174) Zhang, D.; Jin, C.; Tian, H.; Xiong, Y.; Zhang, H.; Qiao, P.; Fan, J.; Zhang, Z.; Li, Z. Y.; Li, J. An: In Situ TEM Study of the Surface Oxidation of Palladium Nanocrystals Assisted by Electron Irradiation. *Nanoscale* **2017**, *9* (19), 6327–6333.

(175) Shimomura, S.; Yoshitake, M.; Tanaka, Y. Structure and Facet Characterization of Platinum Nanoparticles Loaded on Carbon Black Particles Using HRTEM Kun ' Ichi Miyazawa *, Shuichi Shimomura **, Masaru Yoshitake *, Yumi Tanaka *. **2018**, *8* (11), 13–21.

(176) Long, N. V.; Ohtaki, M.; Ngo, V. N.; Cao, M. T.; Nogami, M. Structure and Morphology of Platinum Nanoparticles with Critical New Issues of Low- and High-Index Facets. *Adv. Nat. Sci. Nanosci. Nanotechnol.* **2012**, *3* (2).

(177) Navaladian, S.; Viswanathan, B.; Varadarajan, T. K.; Viswanath, R. P. A Rapid Synthesis of Oriented Palladium Nanoparticles by UV Irradiation. *Nanoscale Res. Lett.* **2009**, *4* (2), 181–186.

(178) Burke, M. G.; Bertali, G.; Prestat, E.; Scenini, F.; Haigh, S. J. The Application of in Situ Analytical Transmission Electron Microscopy to the Study of Preferential Intergranular Oxidation in Alloy 600. *Ultramicroscopy* **2017**, *176* (November 2016), 46–51.

(179) Key, J. W.; Zhu, S.; Rouleau, C. M.; Unocic, R. R.; Xie, Y.; Kacher, J. Investigating Local Oxidation Processes in Fe Thin Films in a Water Vapor Environment by in Situ

Liquid Cell TEM. *Ultramicroscopy* **2020**, *209* (March 2019), 112842.

(180) Zeng, Z.; Zhang, X.; Bustillo, K.; Niu, K.; Gammer, C.; Xu, J.; Zheng, H. In Situ Study of Lithiation and Delithiation of MoS2 Nanosheets Using Electrochemical Liquid Cell Transmission Electron Microscopy. *Nano Lett.* **2015**, *15* (8), 5214–5220.

(181) Ahmed, S.; Bianchini, M.; Pokle, A.; Munde, M. S.; Hartmann, P.; Brezesinski, T.; Beyer, A.; Janek, J.; Volz, K. Visualization of Light Elements Using 4D STEM: The Layered-to-Rock Salt Phase Transition in LiNiO2 Cathode Material. *Adv. Energy Mater.* **2020**, *10* (25), 2001026.

(182) Mukherjee, D.; Gamler, J. T. L.; Skrabalak, S. E.; Unocic, R. R. Lattice Strain Measurement of Core@Shell Electrocatalysts with 4D Scanning Transmission Electron Microscopy Nanobeam Electron Diffraction. *ACS Catal.* **2020**, *10* (10), 5529–5541.

(183) Shibata, N.; Findlay, S. D.; Matsumoto, T.; Kohno, Y.; Seki, T.; Sánchez-Santolino, G.; Ikuhara, Y. Direct Visualization of Local Electromagnetic Field Structures by Scanning Transmission Electron Microscopy. *Acc. Chem. Res.* **2017**, *50* (7), 1502–1512.

Appendix A

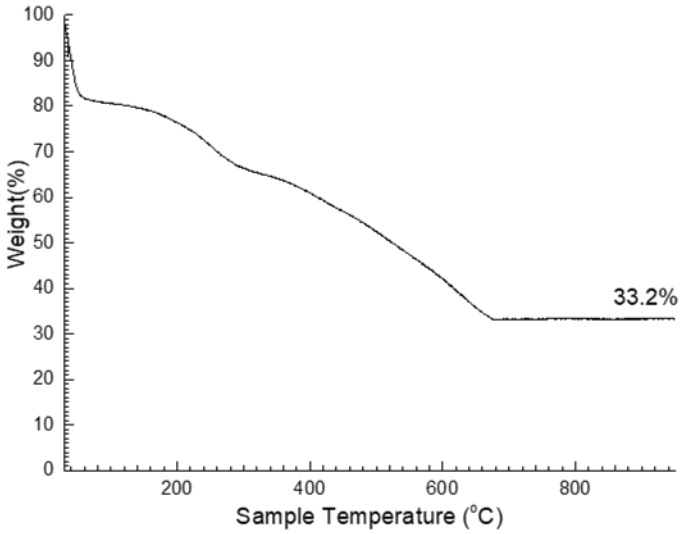

Figure A1. Thermogravimetric analysis of the MOF.
A final weight of 33.2% for the ZrO_2 gives a final Zr weight of 24.6%.